Sub-wavelength field confinement with negative permittivity nanostructures

Lin Nan

München 2023

Sub-wavelength field confinement with negative permittivity nanostructures

Lin Nan

Dissertation
to obtain the doctoral degree of natural sciences (Dr. rer. nat.)
at the Faculty of Physics
of the Ludwig–Maximilians–Universität
München

submitted by
Lin Nan

München, 23/Mar/2023

First Referee: Prof. Dr. Emiliano Cortés
Second Referee: Prof. Dr. Giulia Tagliabue
Day of oral examination: 08/May/2023

Contents

List of Figures

Zusammenfassung

Die Steuerung von Lichtwellen durch Materialien ist ein Entscheidend für die Entwicklung und Optimierung optischer Komponenten. Durch die Manipulation der Permittivität und Permeabilität von Materialien können wir das Verhalten von Lichtwellen steuern. Dies eröffnet neue Möglichkeiten für die Entwicklung neuer optischer Technologien, die von beugungsarmer Bildgebung bis zur photochemischen Katalyse reichen. Eine vielversprechende Möglichkeit zur Begrenzung des Beugungsfeldes sind Materialien mit negativer dielektrischer Permittivität. Nanoskopische Strukturen aus diesen Materialien können Licht auf kleinste Volumina begrenzen, die weit unter dem Beugungslimit liegen. Diese Eingenschaft hat die Entwicklung einer neuen Klasse von optischen Geräten wie Linsen, Filtern und Sensoren ermöglicht.

Zwie Möglichkeiten zur Begrenzung von Licht bis unter das Beugungslimit sind Oberflächenplasmonen und Oberflächenphononen, die durch Nanoantennen oder Metaoberflächen erzeugt werden können. Diese Strukturen bestehen aus metallischen oder polaren dielektrischen Nanostrukturen, wie z. B. Ag, Au oder SiC. Durch sorgfältiges Design von Geometrie und Ausrichtung dieser Nanostrukturen können die elektromagnetischen Eigenschaften von Lichtwellen ausgenutzt werden, um die Beugungsgrenze zu unterschreiten.

Nanoantennen, die auf Oberflächenplasmonenpolaritonen basieren, sind ein ausgezeichneter Kandidat dafür. Dabei wird eine starke Wechselwirkung zwischen Licht und Materie erreicht, was für verschiedene Anwendungen wie Raman-Spektroskopie, Fotovoltaik und optische Sensoren von entscheidender Bedeutung ist. In ähnlicher Weise funktionieren Oberflächenphonon-Polariton-basierte Nanoantennen und Metaoberflächen, die die Wechselwirkung zwischen Licht und Gitterschwingungen verstärken und so neue Möglichkeiten zur Beeinflussung chemischer Reaktionen und für Sensoranwendungen schaffen.

Das Hauptaugenmerk dieser Arbeit liegt auf der Untersuchung der Interaktion von Licht mit Ag-, Au- und SiC-Nanostrukturen, sowohl im Nah- als auch im Fernfeld. Durch den Einsatz von Dunkelfeldspektroskopie, oberflächenverstärkter Raman-Spektroskopie, Fourier-Transformations-Infrarotspektroskopie und optischer Rasternahfeldmikroskopie war es möglich, verstärkte Licht-Materie-Wechselwirkungen zu beobachten. Durch die Verstärkung dieser Wechselwirkungen in den Nanostrukturen konnte eine Modulation der photochemischen Reaktionsdynamik beobachtet werden. Darüber hinaus konnte eine starke Schwingungskopplung mit der Umgebung erreicht werden, was neue Möglichkeiten für optische Sensor- und Spektroskopieanwendungen eröffnet.

Summary

The precise control of light waves through materials is a pivotal facet in the design and optimization of optical components. Through the judicious manipulation of a material's permittivity and permeability, we can effectively govern the propagation and interaction of light waves. This has ushered in a new era of innovation in optical technology, spanning a gamut of applications from sub-diffraction imaging to photochemical catalysis. Of particular interest are materials and structures exhibiting negative dielectric permittivity, which engender extraordinary field confinement below the diffraction limit, enabling unprecedented manipulation of light behavior beyond the boundaries of traditional materials. This unique capability has unlocked a new class of optical devices, ranging from lenses and filters to sensors, that operate at the nanoscale level and represent a paradigm shift in the development of cutting-edge optical technologies.

One potential avenue for achieving sub-diffraction field confinement lies in leveraging the unique properties of surface plasmons and surface phonons through the implementation of nanoantennae and metasurfaces. These finely crafted structures consist of metallic or polar dielectric nanostructures, including but not limited to Ag, Au, and SiC, which have been specifically engineered to interact with light in a highly controlled manner. By carefully manipulating the geometry and orientation of these nanostructures, we can harness the complex electromagnetic properties of light waves, ultimately enabling the realization of sub-diffraction field confinement.

Nanoantennae based on surface plasmon polaritons, consisting of metallic nanostructures, offer a remarkable capacity to confine the electromagnetic energy of incident light within a sub-diffraction-sized region. This confinement yields a substantial increase in the light-matter interaction within the confined space, a critical factor in various applications, including Raman spectroscopy, photovoltaics, and optical sensors. Similarly, surface phonon polariton-based nanoantennae and metasurfaces exploit the interaction between light and lattice vibrations, enabling sub-diffraction confinement. By tailoring these structures, it is possible to amplify the interaction between light and matter, creating novel opportunities to manipulate chemical reactions and sensing applications.

The primary focus of this thesis is to investigate the optical responses of surface polarition-based Ag, Au, and SiC sub-diffraction nanostructures, both in the near-field and far-field regimes. Through the use of techniques such as dark-field spectroscopy, surface enhanced Raman spectroscopy, Fourier transform infrared spectroscopy, and scattering-type scanning near-field optical microscopy it was possible to observe the enhanced light-matter

interactions arising from these sub-diffraction nanostructures. One of the significant advantages of these sub-diffraction nanostructures is their ability to enhance light-matter interactions, leading to the modulation of photochemical reaction dynamics. Further more through these enhanced interactions, it was possible to achieve vibrational strong coupling with the environment, enabling new possibilities for optical sensing and spectroscopy applications.

Chapter 1

Introduction

1.1 Diffraction limit and field confinement

The rapid advent in modern optical technology allows us to directly visualize vast variety of phenomena in nature. However, despite the steady improvement in designing and manufacturing optical components in the past three centuries, the conventional optical techniques are hampered by this ultimate barrier called diffraction limit. Since Ernst Abbe have proposed the relation of the minimum resolvable size to the wavelength λ, refractive index of the lens n, and the half-angle of the focus-cone θ [1],

$$d = 0.5\frac{\lambda}{n\sin\theta}. \tag{1.1}$$

As it is depicted in Figure 1.1, when the light from single point-source passes a optical media with a circular aperture through the focus-cone, it generates a diffraction-limited focus spot at the focal plane as regularly spaced rings, aka Airy disk. The intensity of the diffraction patterns follows the point spread function(PSF) of the system [2]. The denominator in equation 1.1, $n\theta$, is also referred as numerical aperture (NA) that characterizes the angle limit of the accepted light-cones in optical systems, and is often determined by the intrinsic properties of the lenses; the larger the NA is, the smaller the resolution d is.

Figure 1.2 shows examples the Airy disks in diffraction limited and resolvable cases. The The lower panel of the figure shows PSFs of the respective Airy disks. The λ in this case is 500 nm and NA is 0.5. From the Abbe limit, the minimum resolvable distance of two sources, d, should be $\sim$ 500 nm, and Figure 1.2 b and c modeled the case when d is smaller and greater Abbe limit respectively.

The smallest achievable point-to-point distance that can be obtained from a conventional optical system is governed by a fundamental set of physical laws that cannot be easily overcome. Since the maximum half-angel value of the focus-cone is limited to 90,

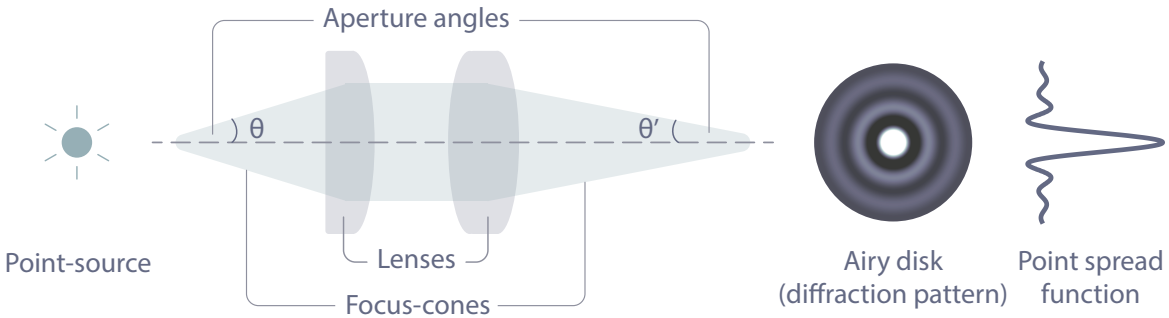

Figure 1.1: When the light from a point-source enters a conventional optical system with circular aperture, the transmitted photons are diffracted at the optical components and eventually appear as Airy disks at the focal plane due to the wave nature of light. The intensity of the diffraction pattern at the Airy disk can be described with point spread function.

refractive indices of the imaging medium can be tuned to further improve the resolution. Although there has been tremendous efforts made to focus the light in smallest possible d through rational designs and optimizations of the optical components, the ability to focus the light is still restricted by the refractive index range of the common optical materials; and in practice, the aperture angle larger than 80 degrees can be only found in the high-end objectives that costs thousands of Euros.

Recently, several exciting novel approaches have emerged to overcome the diffraction limit of conventional optical systems. It now appears that there is no fundamental spatial limit in focusing light, and it has become possible to confine light up to a nanometer range. One of the most promising techniques is the use of negative permittivity materials in optical systems. These materials have unique optical properties that allow for the manipulation of light at the nanoscale, enabling researchers to go beyond the limitations of traditional optical methods. This has opened up new avenues for the study of biological and physical phenomena at unprecedented spatial resolutions and holds great potential for applications in fields such as nanophotonics, sensing, and imaging.

1.2 Field confinement in negative permittivity materials

The behavior of light waves in different materials can be predicted by two significant parameters: permittivity, ϵ_r, and permeability, μ_r. These parameters are key to describing the refractive index of an optical material, which is the ratio of the speed of light in a

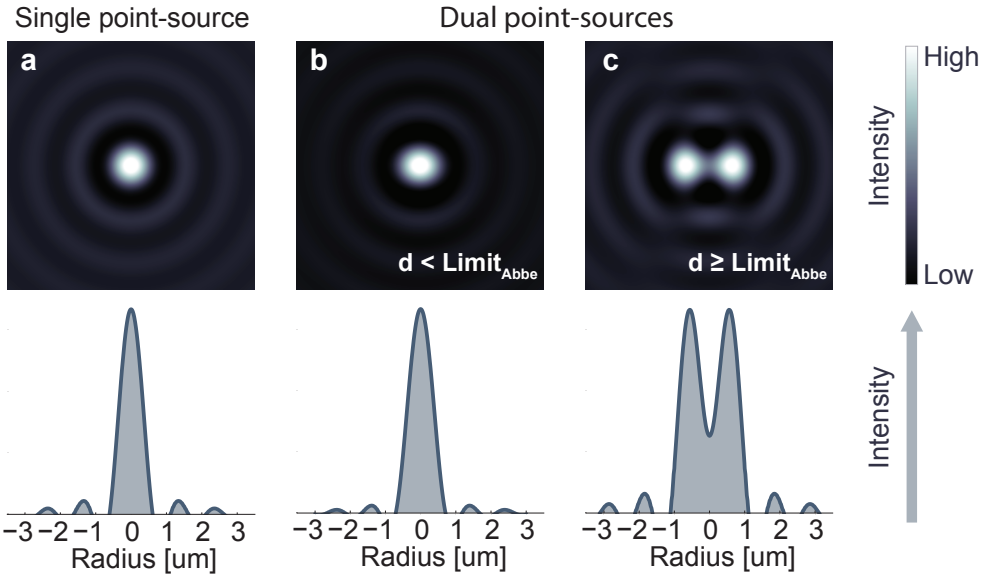

Figure 1.2: Modeled Airy disks and point spread function for diffraction for the case $\lambda = 500$ nm, and NA $= 0.5$. Upper panel shows Airy disks from one point-source and unresolvable and resolvable cases for two point-sources. The lower panel shows relative light intensity based on point spread function of each case. When the distance, d, between two sources is smaller than Abbe limit (b), the observed image is unresolvable; and is equal or larger than Abbe limit (c), the observed image is resolvable.

vacuum to the speed of light in the material.

The refractive index plays a crucial role in the propagation of light waves through different media. Snell's law, which describes the relationship between the angle of incidence and the resulting angle of refraction of light waves at an interface between two media, depends on the refractive indices of the two media. The refractive index of an achiral medium is given by the equation

$$n = \pm\sqrt{\epsilon_r \mu_r}, \tag{1.2}$$

which is dependent on the permittivity and permeability of the material. This equation demonstrates that the refractive index can be manipulated by changing the values of the permittivity and permeability of the material. This ability to control the behavior of light waves within and at the interface of certain materials allows for the intentional determination of the refractive index, which is critical for designing and optimizing optical components for specific applications. Such manipulation of the optical property can potentially applied for overcoming the diffraction-limit that is mentioned in the previous section.

The concept of negative refractive index materials was first proposed in 1968 by Russian physicist Victor Veselago [3]. Veselago theorized that materials with both negative permittivity and negative permeability could lead to a negative refractive index, where the phase and group velocities of light waves are reversed. This unique property allows for a range of novel optical phenomena, including sub-diffraction field confinement and super-resolution imaging.

Materials with negative dielectric permittivity are able to guide surface plasmon–polariton (SPP) modes in metals below the plasma frequency and surface phonon polaritons (SPhP) modes in polar dielectrics. These modes are collective oscillations of electron plasma or surface phonon that couple with electromagnetic waves. The ability to guide these modes enables nanophotonics beyond the diffraction limit, which studies the propagation, localization, and guidance of strongly localized SPP and SPhP modes using nanostructures.

Figure 1.3 shows carrier mobility, carrier concentration, and interband losses of the commong materials that supports surface polaritions [4]. The carrier concentration and mobility of plasmonic materials are important factors that can influence the field confinement in these materials. The carrier concentration refers to the density of free electrons or holes in the material, while the mobility refers to how easily these charge carriers can move through the material.

In general, higher carrier concentrations can lead to stronger plasmonic responses and more efficient field confinement in plasmonic materials. This is because plasmons, which are collective oscillations of the free electrons in the material, rely on the presence of these electrons to exist. Therefore, a higher concentration of free electrons can support stronger plasmonic resonances, leading to more localized fields and stronger light-matter interactions. Similarly, higher carrier mobilities can also improve the field confinement in plasmonic materials. This is because the mobility determines how quickly the free electrons can move in response to an applied electric field. If the mobility is high, the electrons can respond more quickly to the field, leading to a stronger and more localized plasmonic response. Considering all the factors and the losses, this thesis is focused on exploiting Ag, Au, and SiC for visible and IR studies.

The development of surface plasmon and surface phonon based waveguides and antennae has been driven by the potential to combine the compactness of electronic circuits with the bandwidth of photonic networks. These structures enable mode confinement that is not limited by the material parameters of the guiding structure, which is critical for achieving sub-diffraction field confinement.

In summary, the ability to control the behavior of light waves through materials by manipulating the permittivity and permeability parameters is crucial for designing and optimizing optical components for specific applications. Materials with negative dielec-

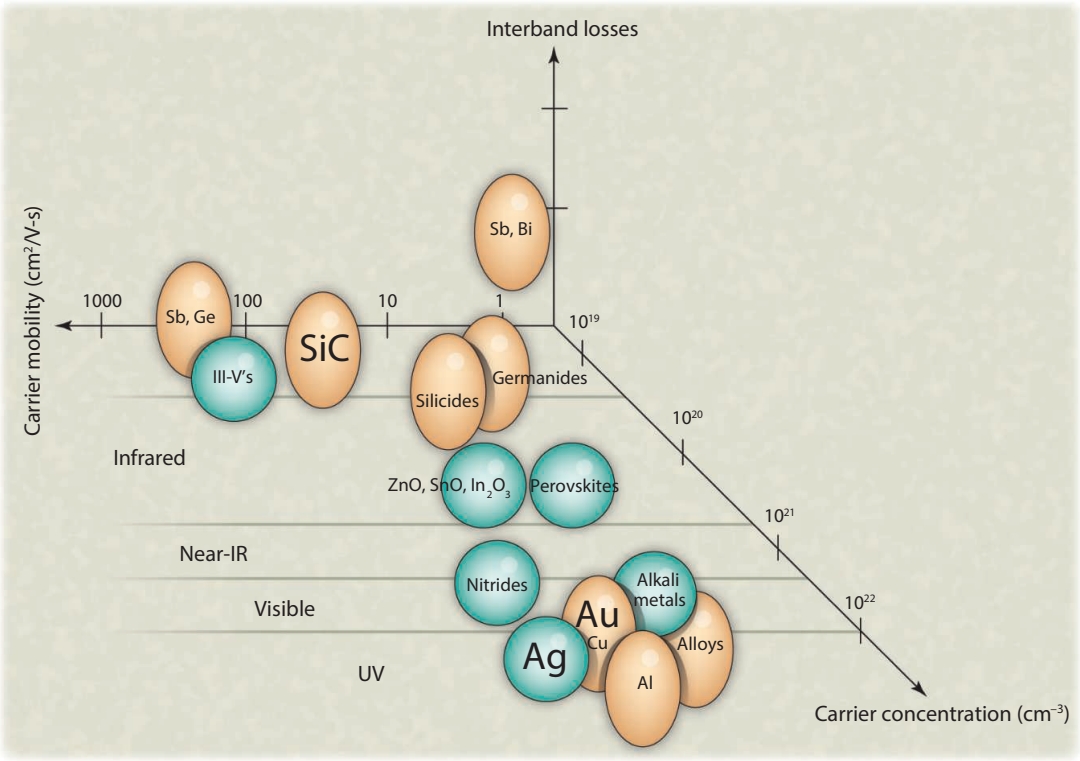

Figure 1.3: Properties of surface polariton materials. Materials with low interband losses are represented by spherical bubbles, while those with larger interband losses in the corresponding part of the electromagnetic spectrum are represented by elliptical bubbles. Maginified materials, ie., Ag, Au, and SiC are the materials of interest within the scope of this thesis [4].

tric permittivity offer a promising solution to achieving sub-diffraction field confinement, which is critical for advancing optical imaging and other applications. The development of surface plasmon and surface phonon based nanoantennae and metasurfaces allow us sub-diffraction field confinement; subsequently enhancing the light-matter interaction within. This thesis is focused on exploring various aspects of sub-diffraction nanostructures with negative permittivity materials and their possible applications in modulating chemical reaction pathways and sensing applications.

Chapter 2

Field confinement with surface plasmon and phonon polaritons

2.1 Surface polaritons

Polaritons are hybrid quasiparticles that result from the strong interaction between photons and electric or magnetic dipole-carrying excitations in a material. This interaction leads to a phenomenon called level repulsion or anti-crossing, where two uncoupled dispersion curves form two different branches. The bandgap between the upper and lower branches changes in accordance with the coupling strength.

Two types of polaritons, namely surface plasmon polariton (SPP) and surface phonon polariton (SPhP), will be discussed in the following sections. SPPs arise from the interaction between photons and the collective oscillation of electrons in a metal's surface, while SPhPs result from the interaction between photons and the collective vibration of atoms in a crystal's surface.

Both types of polaritons have unique properties that make them useful for various applications, such as sensing, imaging, and energy harvesting. For example, SPPs can confine light to sub-wavelength dimensions, leading to high-resolution imaging and sensing. SPhPs, on the other hand, can interact strongly with molecules on a surface, making them useful for chemical sensing and spectroscopy.

Surface polaritons are quasi-particles that arise from the strong interaction between photons and electric or magnetic dipole-carrying excitations. They have unique properties that make them useful for various applications, and two types of polaritons, SPPs and SPhPs, will be discussed in the following sections.

2.2 Surface polaritions in metals and polar dielectrics

With the development of nanofabrication techniques, subwavelength electromagnetic (EM) confinement can be achieved by nanoantenna, leading to the prosperous research field of surface polaritions. As it was briefly mentioned in the Introduction, the negative real part of the dielectric function ($\mathrm{Re}(\varepsilon) < 0$) is crucial for achieving subwavelength EM confinement. In the context of diffraction-limited field confinement, two types of materials are commonly discussed: metals and polar dielectrics. The EM response of metals is characterized by a negative real part of the dielectric function $\mathrm{Re}(\varepsilon) < 0$, indicating that electrons in the conduction band can freely move and polarize in the opposite direction of the incoming field, resulting in low EM penetration. Similarly, polar dielectrics, characterized by a $\mathrm{Re}(\varepsilon) < 0$ region related to the absorption of an infrared-active transverse optical phonon (TO), can also be used for the fabrication of EM antennae [5].

2.2.1 Surface plasmons in metal

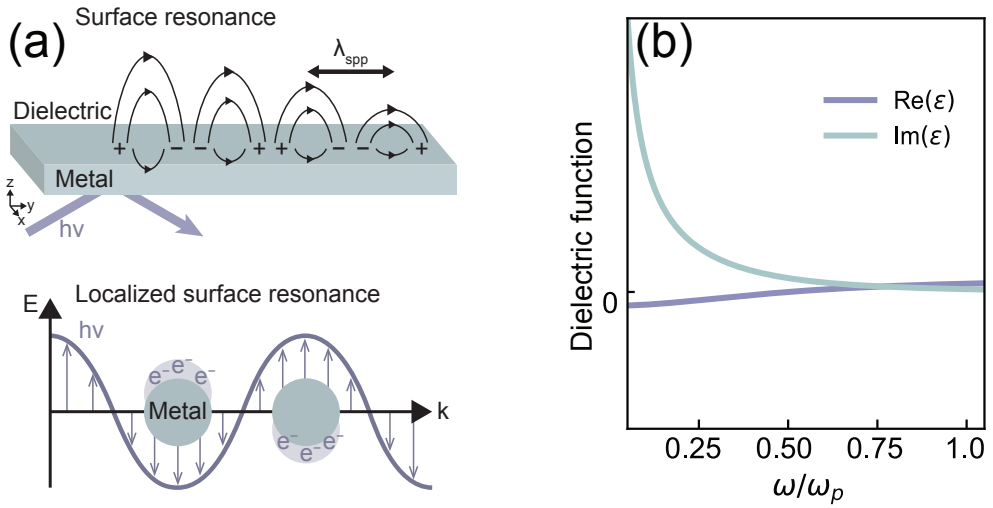

Figure 2.1: Surface plasmon polaritons in noble metals. (a) The schematic of surface plasmon polaritons. The hybridization between incident photons and electron collective oscillations results in propagating electromagnetic waves confined at the interface of metal and dielectric (top) and the representative z-axis electric field distribution (—Ez(z)/Ez(0)—) of surface plasmon polaritons (bottom).(b) The dielectric function from the Drude model eq. 2.3 a) describing the em response of free-electrons ($\gamma = \omega_p/2$, $\varepsilon_\infty = \omega_p/5$) [6].

$$\varepsilon(\omega) = \varepsilon_\infty - \frac{\omega_p^2}{\omega^2 - i\gamma\omega} \tag{2.1}$$

Metals have a negative permittivity at optical frequencies, which arises from the free electrons in the metal that can respond to the incident electromagnetic field. This results in strong absorption of light and the confinement of the field to a thin layer on the surface of the metal, known as SPP mode. When considering materials that are isotropic, the dielectric function can be described by a scalar quantity, which is only a function of frequency $\varepsilon(\omega)$, if nonlocal effects are ignored. The behaviour of an electron plasma can be represented using the Drude model [7].

where γ is the inverse of the mean time between electron collisions, which determines the losses in the material, and ε_∞ offsets the baseline level of ε to account for interband transitions at higher frequencies $\omega > \omega_p$. The plasma frequency ω_p depends on the electron density n and effective mass m^*, as expressed by 2.2:

$$\omega_p = \sqrt{\frac{ne^2}{\varepsilon_0 m^*}}. \tag{2.2}$$

Here, e is the electron charge, ε_0 is the vacuum permittivity, and the effective mass of an electron depends on the conduction band curvature of the material. The plasma frequency indicates the frequency below which electrons can follow the external driving field, while above it, electrons lag behind the driving field. At frequencies above ω_p, the material does not behave like a metal optically. For $\omega \to 0$, metals behave like perfect conductors, where the real part of $\varepsilon(\omega)$ is formally infinitely negative.

The electron density n in Equation 2.2 is the primary factor determining the plasma frequency of a material. Typically, metals have ω_p in the visible or UV range, with electron densities of $n \sim 10^{22} - 10^{23} : \mathrm{cm}^{-3}$, while doped semiconductors have ω_p in the far to near infrared range, depending on the doping level, with electron densities of $n \sim 10^{23} - 10^{29} : \mathrm{cm}^{-3}$. An interesting case is graphene, where the electron density can be tuned by applying an external voltage bias. [8]

2.2.2 Surface phonon polaritions in polar dielectrics

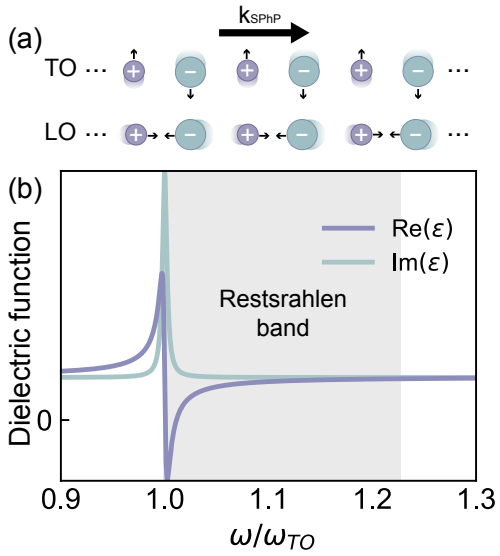

Figure 2.2: Surface phonon polaritons in polar dielectrics. (a) The schematic of TO and LO modes in polar crystals. The circles represent ionic atoms. The small arrows indicate the directions of the displacement of the ions. The arrow on the top indicates the direction of the wave propagation.(b) The dielectric function from the Lorentz model eq. 2.4 describing the EM response in the presence of a transverse optical phonon ($\omega_{LO} = 3\omega_{TO}/2$, $\gamma = \omega_{TO}/200$, $\varepsilon_\infty = \omega_{TO}/500$) [6].

$$\varepsilon(\omega) = \varepsilon_\infty - \frac{\omega_p^2}{\omega^2 - i\gamma\omega} \tag{2.3}$$

Polar dielectrics possess a dipole moment due to their asymmetric crystal structure, which can interact with an electric field and give rise to optical phenomena. In particular, the interaction between the electric field and the lattice vibrations, or phonons, can cause resonant processes that modify the dielectric function. The response of polar dielectrics can be mathematically described by a Lorentz-type function, given by Equation (2.4):

$$\varepsilon(\omega) = \varepsilon_\infty \left(1 + \frac{\omega_{LO}^2 - \omega_{TO}^2}{\omega_{TO}^2 - \omega^2 - i\gamma\omega}\right). \tag{2.4}$$

Similar to the Drude model shown in Equation 2.3, the dielectric function also contains two parameters, ε_∞ and γ, which represent the high-frequency dielectric constant and the damping coefficient, respectively. In this equation, $\varepsilon(\omega)$ denotes the frequency-dependent dielectric function of the material, which is characterized by the presence of two optical phonon frequencies, namely the transverse (TO) and longitudinal (LO) phonon frequencies,

denoted by ω_{TO} and ω_{LO}, respectively.

The Reststrahlen (RS) band is defined as the region in which the real part of the dielectric function is negative, i.e., $\mathrm{Re}(\varepsilon) < 0$. This region is bounded below by the TO phonon frequency and above by the LO phonon frequency (Figure 2.2(b)). The phonon structure of polar dielectrics plays a critical role in determining their optical response, and thus the properties of the Reststrahlen band. Therefore, understanding the lattice vibrations in crystals is essential for understanding the optical properties of polar dielectrics.

In a three-dimensional crystal, there are p atoms in the primitive cell, and there exist $3p$ phonon modes, out of which three are acoustic and $3(p-1)$ are optical. The dispersion of acoustic phonons, denoted by $\omega(k)$, is approximately linear near the $k = 0$ point. Due to the large difference in magnitude between the photon momentum and the lattice momentum, the direct interaction between light and acoustic phonons is possible only at $k = 0$. Therefore, acoustic phonons cannot absorb light directly, in contrast to optical phonons, which have non-zero energy even at $k = 0$.

Each phononic branch has one longitudinal and two transverse modes. However, some of these modes can be degenerate due to crystal symmetries. Since light is a transverse wave, only transverse-optical (TO) phonons can directly absorb photons. Therefore, the imaginary part of the dielectric function, denoted by $\mathrm{Im}(\varepsilon)$ in Figure 2.2 (b), is large near the TO phonon, but not near the longitudinal-optical (LO) phonon. However, not all TO phonons can absorb IR light, as it requires a change in the dipole moment. In non-polar lattices, TO phonons cannot absorb IR light as a displacement of ions does not cause any change in the dipole moment.

Ignoring losses, there exists a general relationship, called the Lyddane-Sachs-Teller (LST) relationship [9], between the frequency of LO and TO phonons at $k = 0$:

$$\frac{\omega_{LO}^2}{\omega_{TO}^2} = \frac{\varepsilon(\omega = 0)}{\varepsilon_\infty} \tag{2.5}$$

Here, $\varepsilon(\omega = 0)$ denotes the dielectric function at zero frequency, and ε_∞ denotes the high-frequency limit of the dielectric function. The LST relationship is a useful tool in the study of the phonon properties of crystals.

Phonons are quantized lattice vibrations in a solid, and they can be divided into two main categories: acoustic and optical phonons. It should be noted that one should not confuse the surface phonons a.k.a optical phonons and accoustic phonons. Acoustic phonons are characterized by having a linear dispersion around the zero-momentum point and play a significant role in determining the speed of sound in the material. On the other hand, optical phonons are characterized by having a flat dispersion around the zero-momentum point and nonzero energy.

In a three-dimensional lattice with p atoms in the primitive cell, there are 3p phonon modes, out of which three are acoustic and 3(p-1) are optical, as shown in Figure 20a. Optical phonons can directly couple to photons as the light line intersects their dispersion, but acoustic phonons do not. The energy of phonons can vary from few to some hundreds of meV, meaning they are found in the mid to far-IR region of the electromagnetic spectrum.

In a diatomic 1D chain allowed to vibrate in a 2D space, four phonon modes exist, as shown in Figure 2.3(b). These different modes are sketched schematically as longitudinal (LA and LO) and transverse (TA and TO) modes. In a 3D lattice, for each phononic branch, there is one longitudinal and two transverse modes. Depending on the structure of the crystal, many of the 3p phononic branches can be degenerated in energy along lattice directions characterized by high symmetry.

Interaction between photons and phonons can happen through inelastic scattering, with acoustic phonons involving "Brillouin scattering" and optical phonons involving "Raman scattering". Overall, the key difference between acoustic and optical phonons is in their dispersion characteristics and their interaction with photons shown in 2.3.

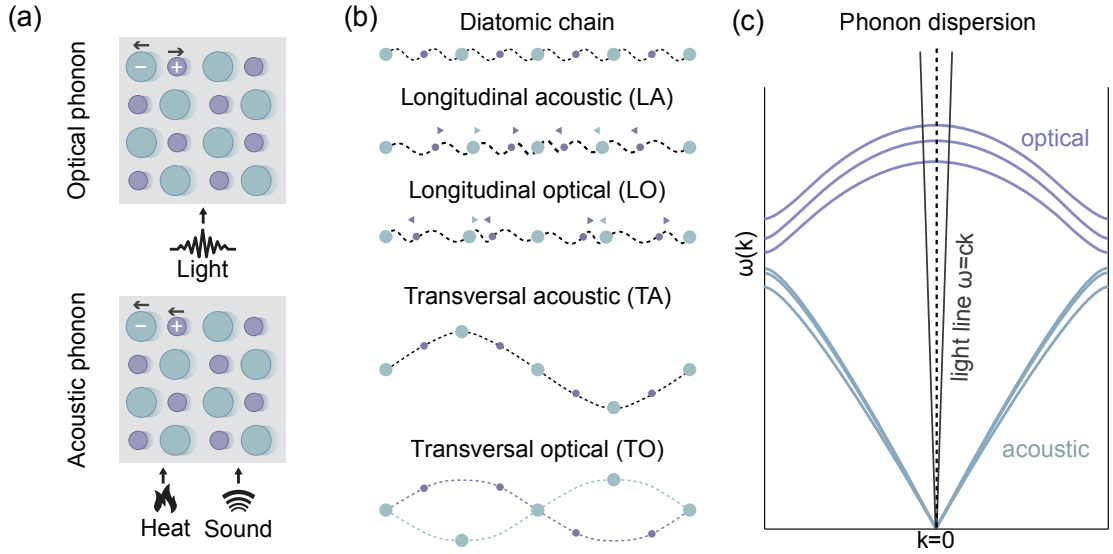

Figure 2.3: (a) Schematic illustration of optical and acoustic phonons and their exciting mechanisms. (b) Sketch of the four phonon modes existing for a diatomic 1D chain free to move in a 2D space.(c) Sketch of the dispersion relations for phonons in a 3D lattice, consisting of three acoustic branches and three optical branches. [10].

2.2.3 Surface plasmon vs. phonon polariton

In Chapter 1, we highlighted the need for materials with $\mathrm{Re}(\varepsilon) < 0$ to achieve subwavelength confinement, and introduced SPP and SPhPs. While the dispersion curves for both types of SW are similar, many differences exist between the two, which we summarize in the following.

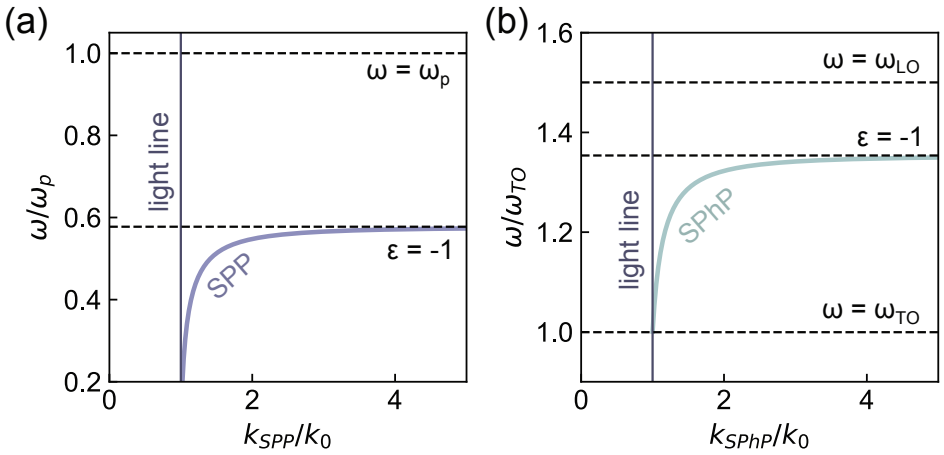

Figure 2.4: Dispersion for SPPs (a) and SPhPs (b) in vacuum [11].

The first obvious difference is that, as can be seen from Figure 2.4, SSP exist at every wavelength below ω_p, while SPhP exist only in the Reststrahlen band. Moreover, if one is interested in deep subwavelength confinement, the wavelength of operation has to be close to $\mathrm{Re}(\varepsilon) = 0$, as shown in Figure 2.5. This in not only true for surface modes, but also for localized resonances. For example, a simple rod antenna of length L has the lowest order resonance at $\lambda_{res} = L/2$ for $\mathrm{Re}(\varepsilon) \ll 0$. Only when the permittivity approaches zero this simple relationship breaks down and subwavelength resonators become possible [12]. From the energy balance point of view, the $\mathrm{Re}(\varepsilon) \ll 0$ condition corresponds to a low amount of energy stored as electron kinetic energy, only negligibly affecting the balance between electric and magnetic energy. The result is that the minimum size of a resonator is only slightly smaller than what determined by the diffraction limit. In turn, this means that losses are low at long wavelengths in metallic antennae, as only a small amount of energy is lost by electron collisions. While SPhPs naturally exist only in the mid-infrared (MIR) range, noble metal plasmonic structures produce the highest confinement at visible frequencies [13]. The different wavelength ranges can be bridged by doped semiconductors, which can have ω_p in the MIR [14], facilitating a direct comparison between SPP and SPhP.

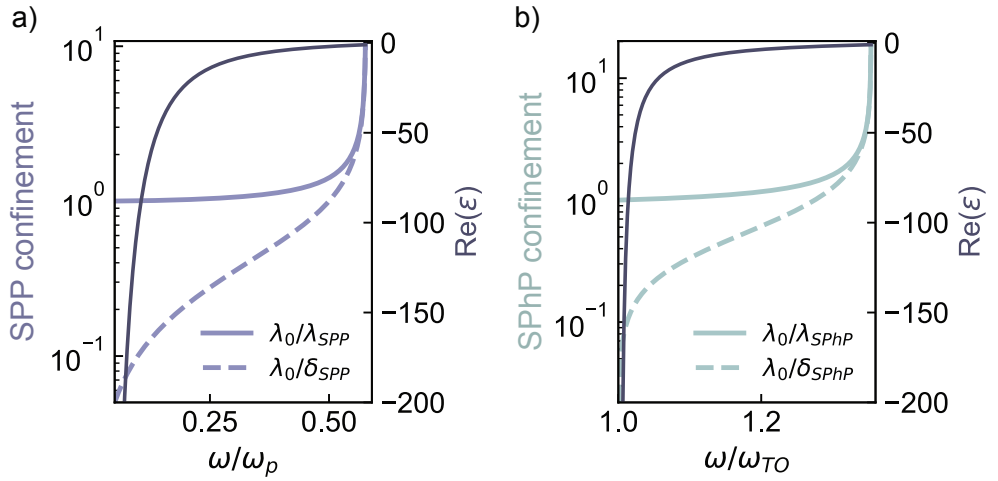

Figure 2.5: SW confinement for SPPs (a) and SPhPs (b) in both the direction of propagation λ_0/λ_{SW} and the direction perpendicular to the interface λ_0/δ_{SW}. Strong confinement is achieved where $\mathrm{Re}(\varepsilon)$ is close to zero [15].

The main property that has led to extensive study of SPhP is the lower losses in polar dielectrics. As we have seen from the energy balance approach in section 2.3.2, independently of the resonator shape the losses are determined by the scattering rate of the oscillating charges in the material. For noble metals, the intrinsic scattering rate is on the order of $10^{14}\,\mathrm{s}^{-1}$, while for doped semiconductors it can be an order of magnitude less due to the lower electron density [16]. However, the higher skin depth of doped semiconductors leads to comparable or even grater losses than in noble metals [16]. In this regard, SPhP offer great advantage since the loss mechanism is not related to electron-electron scattering but to phonon-phonon scattering, which is a much slower process. While SPP have lifetimes on the order of tens of femtoseconds, SPhP can reach three order of magnitude longer lifetimes of tens of picoseconds.

2.3 Diffraction-limited field confinement

2.3.1 Surface waves at the interfaces

In the previous section, we talked about the optical response of metals and polar dielectrics. Both these materials exhibit regions of frequency where their dielectric function's real part, $\mathrm{Re}(\varepsilon)$, is negative. Now, we will discuss how achieving $\mathrm{Re}(\varepsilon) < 0$ is crucial for subdiffractional field confinement when exciting surface waves at the boundary of two semi-infinite slabs. This confinement is necessary to overcome the diffraction limit, which can be explained using the Heisenberg uncertainty principle.

$$\Delta x \Delta p_x \geq \frac{\hbar}{2} \tag{2.6}$$

This principle states that there is a fundamental limit to the precision with which we can simultaneously measure the position and momentum of a particle.

In a 2-dimensional scenario, where a photon beam is propagating in vacuum along the y direction and is focused in the x direction by an objective, the momentum of a photon is related to its wavevector as $\Delta p_x = \Delta k_x \hbar / 2\pi$. The range of wavevector in the x direction is limited by the numerical aperture (NA) of the objective, where the minimum value of wavevector is 0, and the maximum value is k_0NA, with k_0 being the wavevector in vacuum, which is equal to $2\pi/\lambda$, where λ is the wavelength of the photon. In the case of an infinitely extended objective, the numerical aperture is equal to 1, resulting in the maximum wavevector in the x direction being k_0, or $2\pi/\lambda$. Therefore, the spread of momentum in the x direction can be related to the numerical aperture of the objective. By substituting in eq. 2.6 we can show the diffraction limited expression of 1.1:

$$\Delta x \geq \frac{\lambda}{2}. \tag{2.7}$$

In order to overcome this limit, a larger spread in the photon momentum is required with $k_x^{MAX} > k_0$. However, since $k_0^2 = k_x^2 + k_y^2$ and k_x and k_y are real numbers for free-space propagating light, the diffraction limit remains applicable. On the other hand, if k_y is imaginary, the field's spatial spread in the x direction can be confined below the diffraction limit since $k_x > k_0$. An imaginary k-vector corresponds to an exponentially damped field, as $\mathbf{E} = \exp(i\mathbf{k} \cdot \mathbf{r})$. The existence of these evanescent-waves is generally linked to the presence of a material boundary. The area near the surface where these exponentially decaying fields exist is referred to as the near-field since these field components do not propagate and cannot be detected in the far-field, far away from the interface.

Consider the case of a simple material interface where two semi-infinite slabs occupy a two-dimensional space. To produce an evanescent wave, we can use two dielectric media that exhibit total internal reflection (TIR) when light is directed from the medium with the higher refractive index ($n_2 > n_1$) above the critical angle $\theta_c = \arcsin(n_1/n_2)$, as shown in Figure 2.6. Due to continuity, the field in medium n_1 cannot be zero immediately after the interface, leading to the presence of an evanescent wave. The spatial modulation of the field in medium 1 is the same as that in medium 2, which is determined by the free-space wavelength and does not allow the diffraction limit to be broken in the x direction. Although the evanescent field in the z direction is used in TIR fluorescence microscopy to reduce background signals from fluorophores far from the interface, no field enhancement is associated with TIR phenomena. This is because the field intensity from the surface

scales as $I(z) = I_0 \exp(-z/d)$, where d is the critical decay distance and I_0 is the intensity below the surface from the incoming free-space light in medium n_2 [17].

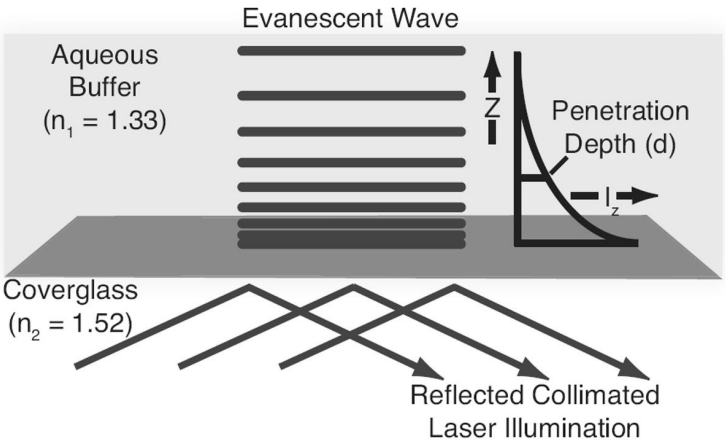

Figure 2.6: Sketch of the TIR phenomena associated with the creation of evanescent waves in the medium with lower refractive index [17].

At the boundary between two materials shown in Figure 2.6, evanescent waves can also be generated by exciting surface waves (SW) that propagate along the interface. These waves feature exponentially decaying fields in the direction perpendicular to the interface. The existence of surface states at the interface between two materials can be derived analytically from Maxwell's equations, by applying continuity relations for the E and H field [18]. The condition for SW is satisfied by demanding that the field components are exponentially decaying in the z direction, which is perpendicular to the interface, such that $E_{i,j}(z)$ and $H_{i,j}(z)$ are proportional to $\exp(-k_i z)$, where the index j runs over the field components and i runs over the two materials. The real part of the wavevectors has to be positive, i.e., $\mathrm{Re}(k_i) > 0$, to achieve exponentially decaying fields. Based on this condition and the continuity of the fields, only transverse magnetic (TM) SW can exist at the boundary, and no transverse electric (TE) SW can exist. This is possible only if the real part of the dielectric function of the two materials is of opposite signs [18]:

$$\frac{k_1}{k_2} = -\frac{\varepsilon_1}{\varepsilon_2} \tag{2.8}$$

Surface waves within a single boundary can only occur between a dielectric material with a real permittivity greater than zero and a material with a real permittivity less than zero. For the purpose of this discussion, we will refer to the dielectric material as medium 1 and the material with the negative real permittivity as medium 2. The two wave vectors (k-vectors) in the z direction are related by the following equations [18]:

$$k_i^2 = \beta^2 - k_0^2 \varepsilon_i \tag{2.9}$$

where β is the wavevector of the SW in the propagation direction and is given by

$$\beta = k_0 \sqrt{\frac{\varepsilon_1 \varepsilon_2}{\varepsilon_1 + \varepsilon_2}} \tag{2.10}$$

The relationship described in equation 2.9 applies to all materials with a negative real part of the dielectric function ($\mathrm{Re}(\varepsilon) < 0$), regardless of their microscopic properties. Such waves are called surface waves (SWs) and can exist in both metals and polar dielectrics in the reststrahlen (RS) band. In metals, they are known as surface plasmon polaritons (SPPs), while in polar dielectrics, they are called surface phonon polaritons (SPhPs), provided that the frequency is below the transverse optical (TO) frequency. The dispersion of SPPs and SPhPs is shown in Figure 2.4, calculated with the dielectric functions in Figure 2.1 and 2.2, where the imaginary part of the dielectric function has been neglected, and a vacuum dielectric slab has been assumed for simplicity. In both cases, the electric field at the material boundary decays exponentially in the z direction, with a high degree of confinement in the "metallic" material, and propagates in the x direction along the material interface. The dispersion curves for SPPs and SPhPs are similar, with a divergence of the wavevector occurring when $\mathrm{Re}(\varepsilon(\omega)) = -1$, or in general when $\mathrm{Re}(\varepsilon(\omega)) = -\varepsilon_{env}$, where ε_{env} is the dielectric function of the dielectric slab. When $\mathrm{Re}(\varepsilon) \ll 0$, the dispersion curves approach the light line $\omega = ck_0$, where SWs behave similarly to free-space photons with poor confinement in both the x and z directions. One key difference between SPPs and SPhPs is that there is no lower energy limit for the existence of SPPs, while SPhPs only exist above the TO frequency. SPPs and SPhPs both have dispersion curves that lie to the right of the light line, meaning that conservation of energy and momentum cannot be satisfied, and free-space photons cannot excite SWs. However, the additional momentum needed for excitation can be provided by gratings or near-field sources [18].

The confinement of surface waves can be analyzed in both propagation and perpendicular directions by taking the inverse of the wavevector. In Figure 2.5, we have shown the ratio between the surface wave (SW) wavelength and free-space wavelength λ_0/λ_{SPhP}, the decay length of the field in the dielectric side $\delta = 2\pi/k_1$, and the value of $\mathrm{Re}(\varepsilon)$. The figure shows that subwavelength confinement is achieved for frequencies where the dielectric function is close to zero in both cases. However, the high confinement region is found in different wavelength ranges for SPPs in metals and SPhPs, with SPPs in the visible range and SPhPs in the mid to far infrared range. The imaginary part of the dielectric function was not considered in this analysis. In real materials, the maximum in-plane k-vector is limited by the nonzero value of $\mathrm{Im}(\varepsilon)$, which sets a lower limit on the achievable

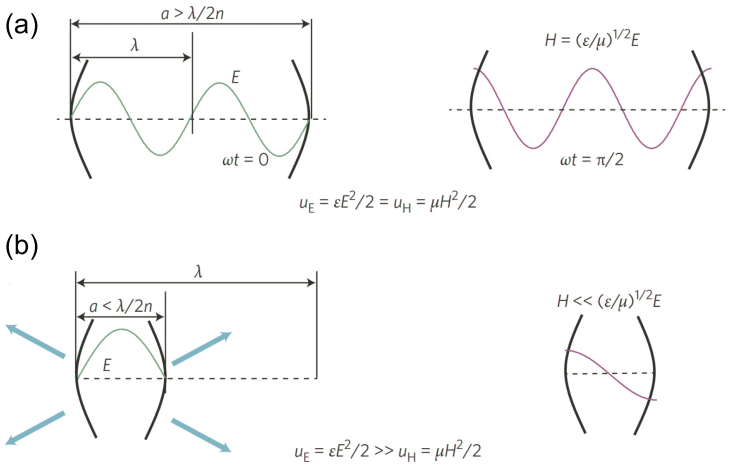

Figure 2.7: (a) In a resonator that is larger than half wavelength, the oscillation of electric and magnetic fields are self-sustaining. (b) In sub-wavelength structures with cavity size a, the magnetic energy is too small as compared to the electric field leading to the leakage of energy [20].

confinement. When losses are taken into account, the k_{SW} dispersion does not diverge at $\mathrm{Re}(\varepsilon) = -1$, but bends back towards the light line. In general, the k-vector is a complex quantity, and a propagation length for the SW can be defined as $L = 1/2\mathrm{Im}(k_{SW})$. Higher confinement comes at the cost of a lower propagation length due to higher field penetration in the material, resulting in stronger losses.

It is clear from this discussion that SPPs and SPhPs have similar behavior from an electromagnetic perspective. However, there are fundamental quantitative and qualitative differences between these two types of SW, as will be described in the following sections.

Although we concluded that a material with $\mathrm{Re}(\varepsilon) < 0$ is required to support SWs in the simple case of two semi-infinite slabs, it is important to note that in more complex geometries, SWs can also exist in purely dielectric architectures. One example of this is Bloch surface waves, which are supported by a heterostructure consisting of alternating dielectric layers. In this configuration, SWs can be excited, but their maximum wavevector β is limited by the highest refractive index of the dielectric stack, which satisfies $1 < n_{SW} < n_{MAX}$ [19].

2.3.2 Oscillations in resonators

In the previous section, we explained that a material with a negative permittivity $\mathrm{Re}(\varepsilon) < 0$ is required for sustaining surface waves (SW) at the boundary between two semi-infinite slabs. This is essential for subdiffractional field confinement. In addition to the detailed geometry of the system, the importance of negative permittivity can be

understood from an energy conservation perspective for resonators. We consider an optical cavity with a length that is a multiple of the wavelength, where standing waves can be formed. The electric field **E** and magnetic field **H** of the system have a spatial dependence in the confinement direction z that can be described as $\sin(2\pi z/\lambda)$. The system is illustrated in Figure 2.7 (a).

The total electromagnetic (EM) energy in the system is periodically exchanged between the electric field energy $u_E \sim \varepsilon|\mathbf{E}|^2/2$ and the magnetic field energy $u_H \sim |\mathbf{H}|^2\mu/2$, where μ is the magnetic permeability of the material. We assume that the fields have a harmonic time dependence. As per Maxwell's equations, the electric field **E** and magnetic field **H** are orthogonal.This leads the third modified Maxwell's equation:

$$\nabla \times \mathbf{E} = -\mu \frac{\partial \mathbf{H}}{\partial t}, \tag{2.11}$$

which is solved if $|\mathbf{H}| = \sqrt{\varepsilon/\mu}|\mathbf{E}|$. When we substitute a certain relationship into the equations for the electric and magnetic energies, we observe that they both have an equivalent value of $u_E = u_H$. This outcome confirms our expectation that energy is periodically exchanged between the electric and magnetic fields without any loss, and as a result, self-sustaining oscillations can occur [20]. It is noteworthy that by following the same process using the fourth Maxwell equation, we can obtain the same result:

$$\nabla \times \mathbf{H} = \varepsilon \frac{\partial \mathbf{E}}{\partial t} \tag{2.12}$$

If the size of the resonator, denoted by a, is smaller than the wavelength of the wave, the spatial dependence of the wave will be given by $\sin(\pi z/a)$, which is illustrated in Figure 2.7(b). This spatial dependence can be related to the magnitude of the electric and magnetic fields through Equation 2.12:

$$|\mathbf{H}| = \frac{2a}{\lambda}\sqrt{\frac{\varepsilon}{\mu}}|\mathbf{E}|. \tag{2.13}$$

It is possible to express the magnetic energy in terms of the electric energy as:

$$u_H = \left(\frac{2a}{\lambda}\right)^2 u_E. \tag{2.14}$$

When the size of a resonator is much smaller than the wavelength of light, i.e., $a \ll \lambda$, there is an energy imbalance as the magnetic energy stored in the resonator (u_H) is much smaller than the electric energy (u_E). This means that self-sustaining oscillations are not possible, and energy stored in the resonator will be lost due to leakage radiation to the environment. This energy imbalance is a manifestation of the diffraction limit, which sets

a minimum dimension of $a = \lambda/2$ below which squeezing the light in a resonator is not possible.

In materials with $\mathrm{Re}(\varepsilon) < 0$, such as metals or polar dielectrics, the energy balance can be restored by considering the kinetic energy (u_K) associated with the movement of free charges, such as electrons in metals or ionic bonds in polar dielectrics. The kinetic term naturally adds in phase with the magnetic term, as currents are out of phase with the electric field. However, this means that sub-wavelength resonators are inevitably lossy, as energy is stored almost half of the time as kinetic energy, which is lost at a rate comparable to the scattering rate (γ) of the oscillating charges.

On the other hand, if one applies the same reasoning to eq. 2.11 instead of eq. 2.12, an apparent contradiction arises, as $u_E \ll u_H$ in this case. This means that to restore energy balance, one needs a source of additional potential energy oscillating in phase with **E**. However, it is less straightforward how this can be achieved, other than by increasing the value of ε until the diffraction limit condition applies again.

2.4 Antennae in optical frequencies

Antennae are structures that enhance the interaction between light and matter in a local area, allowing for efficient energy and information transfer between a transmitter or receiver and the free radiation field. In the radio-frequency and microwave range of the electromagnetic spectrum, antenna theory has been developed to design efficient devices for converting free-propagating radiation to localized energy, and vice versa. Recent advances in nano-optics and plasmonics have enabled the creation of nanoscale antennae that operate at optical frequencies, with the goal of developing devices analogous to those in the larger wavelength ranges. However, scaling established concepts of antenna theory to optical frequencies presents difficulties, as incident radiation at these frequencies penetrates into the metal and creates coherent oscillations of the free-electron gas, resulting in a plasmon resonance. Consequently, the dielectric function of the metal must be taken into account to obtain meaningful results at optical frequencies, unlike the assumption of perfect conductivity in microwave antenna theory. For instance, in rod nanoantennae, an effective wavelength picture has been developed, where the optical antenna responds not to the external wavelength, but to a shorter effective wavelength λ_{eff}, dependent on the material properties via a linear relationship $\lambda_{eff} = n_1 + n_2[\lambda/\lambda_p]$, where λ_p is the plasma wavelength and n_1 and n_2 are coefficients that rely on the properties of the antenna and the surrounding medium. However, analytical solutions for complex geometries are generally unavailable, and electromagnetic simulation methods such as finite difference time domain (FDTD) or finite element (FEM) are used to calculate the properties of nanoantennae.

2.5 Numerical calculations

2.5.1 Maxwell equations in arbitrary 3D geometries

In the previous section, it was mentioned that the for finding solutions for complex geometries, it is necessary to implement numerical calculations. Two commonly used numerical methods for simulating electromagnetic fields are the finite difference time domain (FDTD) method and the finite element method (FEM). In both methods, the three-dimensional space is divided into a mesh of finite units, and solve Maxwell's equations in each unit:

$$\begin{aligned} \frac{\partial \mathbf{B}}{\partial t} &= -\nabla \times \mathbf{E} - \mathbf{B} \\ \frac{\partial \mathbf{D}}{\partial t} &= \nabla \times \mathbf{H} - \mathbf{J} \end{aligned} \tag{2.15}$$

where $\boldsymbol{D}$ is the electric displacement vector, $\boldsymbol{B}$ is the magnetic induction intensity, $\boldsymbol{E}$ is the electric field intensity, and $\boldsymbol{H}$ is the magnetic field intensity. The relationship among the physical values can be expressed as:

$$\begin{aligned} \boldsymbol{D} &= \epsilon \boldsymbol{E} \\ \boldsymbol{B} &= \mu \boldsymbol{H} \\ \boldsymbol{J} &= \sigma \boldsymbol{E} \end{aligned} \tag{2.16}$$

where ρ represents charge density, $\boldsymbol{J}$ is current density, ϵ is the permittivity, μ is the permeability, and σ is the conductivity.

The continuity of the fields is ensured at the boundaries of each unit. However, FDTD and FEM models differ in the algorithms they use to solve Maxwell's equations, which affects the type of mesh that can be employed to discretize the space. In summary, FDTD and FEM are two methods for numerically solving Maxwell's equations in a discretized space, but differ in the algorithm used and the type of mesh employed.

2.5.2 Finite difference time domain method

The finite difference time domain (FDTD) method was first proposed by Kane Shee-Gong Yee in 1966 [21]. The core idea is to discretize the three-dimensional space being studied into Yee cells. The arrangement of the electric and magnetic field components in the x, y, and z directions within each Yee cell is shown in Figure 2.8 the x (y, z) component of the electric field is located at the midpoint of the edge parallel to the x (y, z) axis, while the x (y, z) component of the magnetic field is located at the center of each face

perpendicular to the x (y, z) axis.

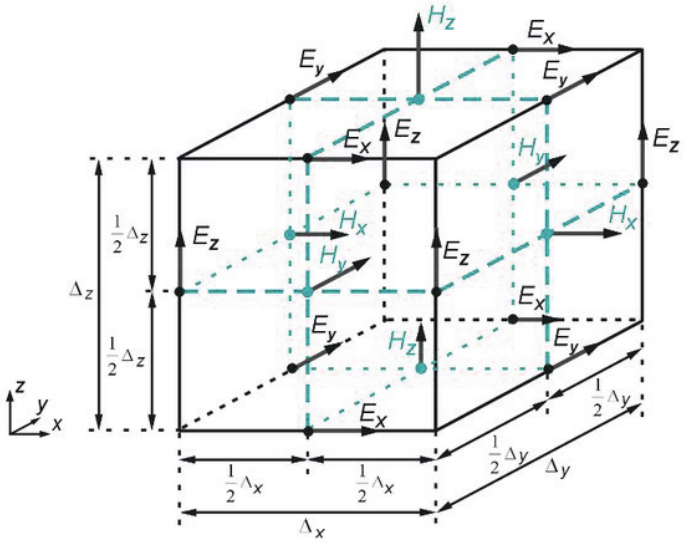

Figure 2.8: Illustration of the electric and magnetic fields in a Yee cell for the implementation of the FDTD method. [21].

Therefore, each x (y, z) component of the electric field (magnetic field) is surrounded by four y (z, x) and z (x, y) components of the magnetic field (electric field). At the same time, the electric and magnetic fields are sampled alternately at half time steps on the time axis, transforming Maxwell's curl equations into a system of difference equations. The derivation of the difference equation set is given below:

$$\begin{cases} \dfrac{\partial H_x}{\partial t} = \dfrac{1}{\mu_0}\left(\dfrac{\partial E_y}{\partial z} - \dfrac{\partial E_z}{\partial y}\right) \\ \dfrac{\partial H_y}{\partial t} = \dfrac{1}{\mu_0}\left(\dfrac{\partial E_z}{\partial x} - \dfrac{\partial E_x}{\partial z}\right) \\ \dfrac{\partial H_z}{\partial t} = \dfrac{1}{\mu_0}\left(\dfrac{\partial E_x}{\partial y} - \dfrac{\partial E_y}{\partial x}\right) \end{cases} \tag{2.17}$$

and

$$\begin{cases} \dfrac{\partial H_x}{\partial t} = \dfrac{1}{\epsilon_0\epsilon_r}\left(-\sigma E_x + \dfrac{\partial H_z}{\partial y} - \dfrac{\partial H_y}{\partial z}\right) \\ \dfrac{\partial H_y}{\partial t} = \dfrac{1}{\epsilon_0\epsilon_r}\left(-\sigma E_y + \dfrac{\partial H_x}{\partial z} - \dfrac{\partial H_z}{\partial x}\right) \\ \dfrac{\partial H_z}{\partial t} = \dfrac{1}{\epsilon_0\epsilon_r}\left(-\sigma E_z + \dfrac{\partial H_y}{\partial x} - \dfrac{\partial H_x}{\partial y}\right) \\ . \end{cases} \tag{2.18}$$

The above equations 2.16 rely on the constitutive relations, and consider non-magnetic materials where the relative permeability $\mu_r = 1$. Now, the components in the electric and magnetic fields are discretized in both space and time. Taking the electric field E(x, y, z, t) as an example, its discretization in space and time can be expressed as:

$$E(x, y, z, t) = E(i\Delta x, j\Delta y, k\Delta z, n\Delta t) = E^n(i, j, k) \tag{2.19}$$

where i, j, and k are the discrete steps of the electric field along the x, y, and z axes in space. Δx, Δy, and Δz are the discrete step sizes, i.e., the grid edge lengths of the Yee cell in each direction. Δt and n are the discrete step size and number of steps along the time axis of the electric field.

With such derivation, FDTD discretizes the continuous Maxwell's equations in time and space into explicit difference equations, avoiding complex operations such as matrix inversion. Additionally, the electric and magnetic field components at different positions in FDTD are obtained through simple iterations, meaning that only initial values and boundary conditions need to be given to solve the equations step by step. Moreover, FDTD solves the equations directly in the time domain, and with the use of Fourier transform, the frequency response of the device over a broadband can be obtained with only one simulation.

2.5.3 Finite element method

The finite element method (FEM) is a technique for solving partial differential equations subject to specific boundary conditions. This method has been widely used in various fields of physics and engineering, such as structural analysis, heat transfer, fluid dynamics, mass transport, and electromagnetism [22]. A general boundary-value problem can be defined by a differential equation in a domain Ω:

$$\mathcal{L}\phi = f \tag{2.20}$$

where $\mathcal{L}$ is a differential operator and f the excitation or forcing function. ϕ is an unknown solution to a differential equation subject to boundary conditions on the boundary Γ of a domain Ω. In the solution of three-dimensional Maxwell equations, the differential operator $\mathcal{L}$ takes the form of the coupled wave equations for the fields $\mathbf{E}$ and $\mathbf{H}$, assuming harmonic time dependence and computing time derivatives as $\partial E/\partial t = i\omega E$. The boundary problem specified by the equation can be solved in different ways, including the Ritz and Galerkin methods [22]. The Ritz method utilizes the variational principle, but it is not discussed here. Instead, we present the Galerkin method, which is a member of the

weighted residual methods family. Considering an approximate solution $\tilde{\phi}$, the residual r can be defined as

$$r = \mathcal{L}\tilde{\phi} - f \neq 0 \tag{2.21}$$

By minimizing the residual r over the entire domain Ω, the best approximation $\tilde{\phi}$ can be determined. This condition can be written as:

$$R_i = \int_\Omega \omega_i r \, d\Omega = 0 \tag{2.22}$$

where R_i is named the weighted residual integral i and ω_i are chosen weighting functions defined over the whole domain Ω. In Galerkin's method the weighting function ω_i are chosen to be the same as those used to construct the approximate solution:

$$\tilde{\phi} = \sum_{j=1}^{N} c_j \omega_j \tag{2.23}$$

where c_j are constant coefficients to be determined. Eq. 2.22 can be rewritten by using eq. 2.21 as:

$$R_i = \int_\Omega \left(\omega_i \mathcal{L}\{\omega\}^T\{c\} - \omega_i f\right) \, d\Omega = 0 \tag{2.24}$$

This can be rewritten as a matrix equation:

$$[S]\{c\} = \{b\} \tag{2.25}$$

where the matrix elements are

$$S_{ij} = \frac{1}{2}\int_\Omega \left(\omega_i \mathcal{L}\omega_j + \omega_j \mathcal{L}\omega_i\right) \, d\Omega \tag{2.26}$$

and

$$b_i = \frac{1}{2}\int_\Omega \omega_i f \, d\Omega \tag{2.27}$$

To apply Galerkin's method, we consider a one-dimensional system comprising two infinite parallel plates located at $x = 0$ and $x = 1$, respectively. The plates are held at potentials of 0 V and 1 V, respectively. The region between the plates is filled with a medium having a constant permittivity of ε. Additionally, the region has a space-varying electric charge, $\rho(x) = -(x+1)\varepsilon; \mathrm{C/m^3}$, where x is the distance from the $x = 0$ plate. The solution can be found for this system within the interval $0 \leq x \leq 1$, by solving the Poisson

equation. The solution found through Poisson equation can be expressed as:

$$\frac{d^2\phi}{dx^2} = x + 1. \tag{2.28}$$

By applying boundary conditions $\phi|_{x=0} = 0$ and $\phi|_{x=1} = 1$ to Eq. 2.28, it admits the analytical solution $\phi(x) = x^3/6 + x^2/2 + x/3$. Eq. 2.28, and it can be written in the form of the boundary condition problem 2.20 with $\mathcal{L} = d^2/dx^2$ and $f = x + 1$. The weighted residual equation for Galerkin's method following eq. 2.21 is:

$$\int_0^1 \omega_i \left(\frac{d^2\tilde{\phi}}{dx^2} - x - 1 \right) dx = 0 \tag{2.29}$$

In the boundary problem, there are only two conditions that need to be satisfied at $x = 0$ and $x = 1$. Therefore, in equation 2.29, we select $i = 1$ and $i = 2$ to account for these conditions. To continue with the solution, we must choose the functions ω_i, which are also utilized in constructing $\tilde{\phi}$. A simple choice is to take a polynomial expansion for the approximate solution:

$$\tilde{\phi}(x) = c_1 + c_2 x + c_3 x^2 + c_4 x^3 \tag{2.30}$$

Applying the boundary conditions $\tilde{\phi}|_{x=0} = 0$ and $\tilde{\phi}|_{x=1} = 1$ to 2.30:

$$\tilde{\phi}(x) = x + c_3(x^2 - x) + c_4(x^3 - x) \tag{2.31}$$

Then we take the ω_i functions associated to the coefficients c_3 and c_4 to be determined:

$$\begin{aligned} \omega_1 &= x^2 - x \\ \omega_2 &= x^3 - x \end{aligned} \tag{2.32}$$

Now the approximate solution $\tilde{\phi}(x)$ and the two functions ω_1 and ω_2 can be substituted in 2.29. From the evaluation of the definite integral, two algebraic equations are obtained:

$$\begin{aligned} \frac{c_3}{3} + \frac{c_4}{2} - \frac{1}{4} &= 0 \\ \frac{c_3}{2} + \frac{4c_4}{5} - \frac{23}{60} &= 0 \end{aligned} \tag{2.33}$$

from which the coefficients $c_3 = 1/2$ and $c_4 = 1/6$ can be determined. In this case the exact analytical solution is recovered. It can be shown that this happens as long as the

trial functions constitute a complete basis for the problem [22].

Galerkin's method is an effective approach to solve boundary problems, but its success depends on finding a suitable set of trial functions that can approximate the true solution. In one-dimensional problems, simple polynomial trial functions are often sufficient. However, for three-dimensional problems, where the real solution can be highly complex, it becomes challenging to find an appropriate set of trial functions. To overcome this difficulty, the finite element method (FEM) is used to divide the whole domain into smaller subdomains. By doing so, Galerkin's method can be applied to each subdomain with simple trial functions. The solutions found in each subdomain are then interpolated using a chosen interpolation function, which is usually linear or a low-order polynomial. The overall process of FEM with Galerkin's method can be summarized in four steps: firstly, the whole domain is subdivided into smaller subdomains. Secondly, an appropriate interpolation function is selected to relate the solutions found in each subdomain. Thirdly, a system of algebraic equations is obtained by applying Galerkin's method. Finally, a solution for the system of equations is determined.

2.5.4 FDTD vs. FEM methods

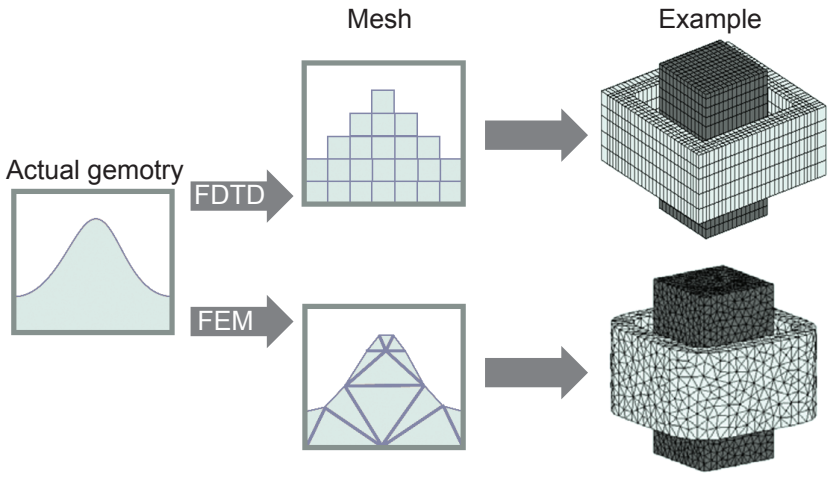

Figure 2.9: Example of meshing (top view) in a FDTD (a) and a FEM (b) simulation [23].

In the previous sections, we have introduced the fundamental elements of two numerical methods, FDTD and FEM, used to solve Maxwell's equations in three dimensions. Both methods have distinct differences, advantages, and shortcomings depending on the problem at hand. One of the main differences lies in the way they discretize the three-dimensional space. While FDTD only allows for non-uniform orthogonal gridding, FEM has no inherent limitation in subdividing the domain, which makes it better suited for meshing curved

structures. FEM subdivides the domain into triangular shapes in two dimensions and tetrahedrons in three dimensions, enabling it to approximate complex shapes more efficiently than FDTD. Consequently, FEM simulations usually require a lower number of mesh cells, reducing the simulation time. An example of the different meshing strategies in FEM and FDTD simulations is shown in Figure 2.9 for a three-dimensional disk. In this case, FDTD required four times more mesh cells than FEM ($\sim 115,000$ and $\sim 25,000$ mesh cells, respectively) to simulate the same volume, and the circular geometry was better represented in the FEM model thanks to its non-Cartesian mesh.

Another significant difference between the two methods is that FDTD is a time-domain method, while FEM is a frequency-domain method. In FDTD simulations, a defined source excites the system, and the time evolution is simulated step by step. This means that the transient response of a system can be investigated, and broadband simulations are naturally included in a single run. The frequency response in FDTD models is obtained by Fourier transforming the time signal. In contrast, FEM assumes the time dependence to be harmonic, making it incapable of investigating the transient response of a system. Therefore, simulations in FEM are inherently single-wavelength, and the broadband response is obtained by combining many different single-wavelength simulations. FDTD struggles to simulate very high-quality factor systems because to obtain accurate results, one needs to extend the simulation in time until the fields are entirely dissipated. Furthermore, FDTD requires fitting the material response with an analytical model to simulate dispersive materials, whereas this is unnecessary in FEM.

In this work, both FEM and FDTD simulations are employed to investigate various nanophotonic structures. Lumerical software for FDTD simulations and CST Studio for FEM simulations are the main platforms.

Chapter 3

Exploiting plasmonic field enhancement

3.1 Characterization of plasmonic nanostructures

3.1.1 Cross-sections

As it was described in the previous section plasmon polaritons are collective oscillations of free electrons on the metal surface. The interaction of these surface plasmons with light can lead to a wide range of unique optical phenomena, such as localized field enhancement, light confinement, and spectral filtering, among others. In this section, two indirect characterizaton methods plasmonic structures that are employed for the studies in Sections 3.3 and 3.4 will be introduced.

One important way of characterizing the optical response of plasmonic nanostructures is through their cross-sections. The cross-sections are influenced by the carrier concentration. The carrier concentration affects the plasma frequency and the damping of the plasmonic resonance. When the carrier concentration increases, the plasma frequency shifts to a higher value, resulting in a blue-shift of the plasmonic resonance. This is because the increased concentration of free charge carriers results in stronger collective oscillations of the electrons within the nanoantenna. For instance, as shown in Figure 1.3 from Chapter 1, the carrier of Ag is higher than Au have therefore leading to a blue-shifted resonance rage for Ag as compared to Au. Additionally, the damping of the plasmonic resonance increases with carrier concentration, resulting in a broadening of the resonance line-width.

The characterization of cross-sections in plasmonic nanostructures can provide important insights into their optical properties. For example, the shape and size of the cross-section can affect the spectral response of the nanostructure, such as the position and in-

tensity of resonant peaks in the absorption, scattering or reflection spectra. Additionally, the orientation and polarization of the incident light can also influence the cross-section and thus the optical response of the nanostructure [**?**].

The most common way of determining the cross-section is defined as:

$$\sigma(\omega) = \frac{P_{rad}(\omega)}{I_{exc}(\omega)}, \tag{3.1}$$

where $P_{rad}(\omega)$ is the power from the far-field irradiation, and $I_{ext}(\omega)$ is the excitation intensity at frequency ω. This measure is expressed in units of area and is typically normalized by the object's transverse area [24].

Both of these effects can influence the cross-sections in plasmonic nanoantennae. For example, a blue-shift of the plasmonic resonance can result in enhanced absorption or scattering of incident light at shorter wavelengths. The broadening of the resonance linewidth can also result in increased absorption or scattering cross-sections over a broader range of wavelengths.

When analyzing the scattering problem, it can be challenging to use analytical methods. Numerical simulations are often necessary, particularly for accurately determining the power, which is determined by the Poynting vector, $\mathbf{S} = \mathrm{Re}\{\mathbf{E}\times\mathbf{B}\}$. This vector measures the flow of the electric and magnetic fields out of the antenna that reaches the far-field. To ensure accurate measurements, power monitors must be positioned at a significant distance from the nanostructure. Furthermore, it is crucial to consider only radiative terms that scale as 1/r, where r is the distance from the scattering object to the observation point in the far-field [24].

The response of a scattering system to an external excitation can be obtained by taking the Fourier-transform of the product of the scattering cross-section and the incident irradiance:

$$P_{rad}(t) = \frac{1}{\sqrt{2\pi}} \int_R \sigma_{scat}(\omega) I_{exc}(\omega) e^{+i\omega t}\, d\omega. \tag{3.2}$$

It is often assumed that the scattering cross-section follows a Lorentzian shape, although this is an *ad hoc* assumption and stems from the resemblance of resonance functions to Lorentzians:

$$\sigma_{rad}(t) \propto \frac{\zeta/2}{(\omega-\omega_0)^2 + (\zeta/2)'}. \tag{3.3}$$

In this equation, ζ is the full-width half-maximum (due to losses) and ω_0 is the position of the peak of the Lorentzian. Furthermore, by assuming a constant excitation intensity throughout the peak's width, $I_{scat}(\omega) = I_0$), we can integrate the equation

$$P_{rad}(t) \propto e^{-\zeta\pi|t|} \tag{3.4}$$

to obtain the radiated power as a function of time.

This means the inverse of the full-width half-maximum, denoted as $1/(\zeta\pi)$, is a characteristic time that relates to the rate at which the emitted intensity dissipates. In the scientific literature, the terms "super-radiant" and "sub-radiant" are used to describe broad and narrow modes, respectively. This terminology is borrowed from atomic physics, where a group of dipoles can collectively interact to produce a burst of short-duration increase in the emitted intensity [25–27], or conversely, a total or partial cancellation of it over an extended period [28]. It should be noted that although a Lorentzian was used in the derivation of the expression for scattered power, the general result does not depend on the specific functional dependence of the scattering cross-section on frequency. The only requirement is that it is a function that decreases rapidly enough.

Another quantity that is relevant in the study of scattering phenomena is the differential scattering cross-section for a particular excitation polarization direction, denoted by the unit vector $\hat{n}$, as a function of the spherical angles θ and ϕ:

$$\sigma_{scat,\hat{n}}(\omega;\theta,\phi) = \frac{P_{rad,\hat{n}}(\omega;\theta,\phi)}{I_{ext}(\omega)}. \tag{3.5}$$

This quantity represents the probability per unit solid angle that a scattering event will occur in a specific direction, given a particular polarization direction of the incident wave [**?**]. The differential scattering cross-section can be calculated by analyzing the scattering amplitude and considering the polarization and direction of the incident and scattered waves:

$$\sigma_{scat,\hat{n}}(\omega) = \int_0^{\pi}\int_0^{2\pi} \sigma_{scat,\hat{n}}(\omega;\theta,\phi) sin\theta d\theta d\phi. \tag{3.6}$$

Its dependence on the polar and azimuthal angles allows for a detailed understanding of the scattering behavior and can provide valuable insights into the structure and properties of the scattering object.

The relevant values can be measured experimentally through dark-field spectroscopy [18]. The experimental details will be described in end of this chapter. In the upcoming chapters,the scattering cross-section of the application-specific nano-antennae will be shown accordingly.

3.1.2 Dark-field spectroscopy

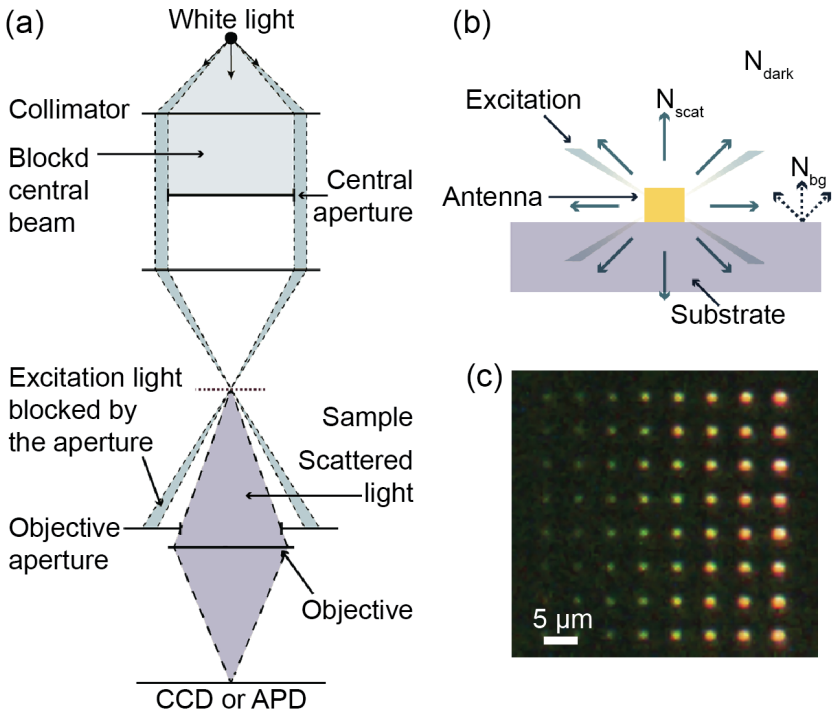

Figure 3.1: (a) Schematic of a dark-field microscopy, (b) schematic showing the various source of the signals, and (c) an example dark-field image of gold nano-bowties with various scattering cross-sections [29].

The measured scattering cross-section by the system with numerical aperture NA that is depicted in Figure 1.1 can be re-written from equation 3.6 as follows:

$$\sigma_{scat,\hat{n}}(\omega) = \int_0^{\theta_0} \int_0^{2\pi} \sigma_{scat,\hat{n}}(\omega;\theta,\phi) sin\theta d\theta d\phi, \tag{3.7}$$

where $sin\theta_0 = NA$.

This means that the light is only collected from the top from the angle $\theta_0 \leq \pi/2$.

Nano-antennae in real samples are typically situated on top of substrates, which can result in a reflection contribution that interferes with accurate analysis of the antennae. To overcome this issue, illuminating from the side can be a viable solution. However,

such an approach can also modify the spectrum because light may excite modes in the vertical direction of the antennae, leading to the emergence of new peaks in the spectrum, as depicted in Figure 3.1. As a result, researchers have been exploring the development of dark-field microscopy from a near-normal incidence, which has been an important area of investigation [30]. In this study, all spectra obtained from experiments were acquired at an angle to account for these factors.

The process of inferring the scattering cross-section involves a series of steps. First, an extended white source is used to illuminate the sample containing the nano-antennae. The source passes through a converging lens that is positioned near an aperture, which only allows a ring of light to pass through. A condenser is placed after the focal plane of the lens to form an image of the source onto the sample. This illumination method combines Köhler illumination and a centrally-blocked aperture to blur out any spatial irregularities in the brightness distribution.

When the nano-antenna interacts with the light, it scatters photons that can be detected in the far field, and coupled into a fiber. This process is crucial for determining the scattering cross-section. The Köhler illumination method and the centrally-blocked aperture ensure that the scattering is accurately detected and recorded. This method has been previously described in literature as Köhler illumination [31]

In the context of analyzing scattering measurements, it is necessary to account for various sources of background signals that can obscure the signal of interest. One such source is the darkcounts of the cooled coupled-charge device (CCD), which contribute to the scattered counts $N_(scat)(\omega)$. To obtain the true contribution of the nano-antenna, the darkcounts($N_{dark}(\omega)$) corrected background signal arising from scattering imperfections in the substrate $N_{bg}(\omega)$ must be removed. Additionally, to accurately characterize the frequency-dependent transmission of the system, it is essential to obtain the spectrum of a perfectly white scatterer, which not only includes the quantum efficiency at specific frequencies but also the frequency dependency of the illuminating lamp. This spectrum is commonly referred to as $N_{ref}(\omega)$. Therefore, a thorough analysis of the scattering measurements requires the removal of multiple sources of background signals and the acquisition of essential reference spectra. This can be expressed in the following equation:

$$\sigma_{scat,\hat{n}}(\omega) \propto \frac{N_{scat,\hat{n}}(\omega,\theta_0) - N_{bg,\hat{n}}(\omega,\theta_0)}{N_{ref,\hat{n}}(\omega,\theta_0) - N_{dark,\hat{n}}(\omega,\theta_0)}. \tag{3.8}$$

3.1.3 Surface enhanced Raman spectroscopy

The information from the dark-field spectra can provide the far-field optical properties. However, it is not possible to obtain any further information regarding diffrection-limited

properties such as local-field enhancement or hot-electron generations. One of the methods to explore the diffraction-limited properties within a simple optical microscopy set-up is through the surface-enhanced Raman spectroscopy (SERS).

SERS is a technique that enhances the Raman signal of molecules adsorbed on or near metallic surfaces. The principle behind SERS is based on the interaction between the electromagnetic field and the metal surface, which results in an enhancement of the Raman signal and this can provide insights of the near-field in the plasmonic nanostructure.

The enhancement factor (EF) of SERS is defined as the ratio of the Raman intensity of a molecule on a metal surface to the Raman intensity of the same molecule in the absence of the metal surface. The EF can be expressed as:

$$EF = \frac{I_{SERS}}{I_{Raman}} \tag{3.9}$$

where I_{SERS} is the intensity of the SERS signal and I_{Raman} is the intensity of the Raman signal in the absence of the metal surface [32–34].

The enhancement in the SERS signal is attributed to two main mechanisms: chemical enhancement and electromagnetic enhancement. The chemical enhancement arises from the chemical interactions between the molecule and the metal surface, while the electromagnetic enhancement is due to the interaction between the incident electromagnetic field and the metal surface.

The electromagnetic enhancement arises from the excitation of surface plasmon resonances in the metal surface. When a metal surface is illuminated with light, the free electrons in the metal can be excited to oscillate collectively, creating a surface plasmon resonance. The surface plasmon resonance results in a strong electromagnetic field at the metal surface, which can enhance the Raman signal of molecules in close proximity to the metal surface.

The enhancement in the electromagnetic field can be described by the local electromagnetic field enhancement factor (EMEF), which is the ratio of the electromagnetic field intensity at the surface of the metal to the incident electromagnetic field intensity. The EMEF can be expressed as:

$$EMEF = \frac{|E_{SERS}|^2}{|E_0|^2} \tag{3.10}$$

where $|E_{SERS}|$ is the magnitude of the electromagnetic field at the surface of the metal and $|E_0|$ is the magnitude of the incident electromagnetic field [32, 33].

The EMEF is strongly dependent on the geometry of the metal surface, the excitation wavelength, and the polarization of the incident electromagnetic field. In general, the EMEF is highest when the excitation wavelength is resonant with the surface plasmon res-

onance of the metal and when the incident electromagnetic field is polarized perpendicular to the metal surface.

3.2 Hot-electrons in plasmonic materials

Published in: "Hybrid Plasmonic Nanomaterials for Hydrogen Generation and Carbon Dioxide Reduction" ACS Energy Letters (2022) [35]
Simone Ezendam, Matias Herran, Lin Nan, Christoph Gruber, Yicui and Kang, Franz Groebmeyer, Rui Lin, Julian Gargiulo, Ana Sousa-Castillo, and Emiliano Cortés.

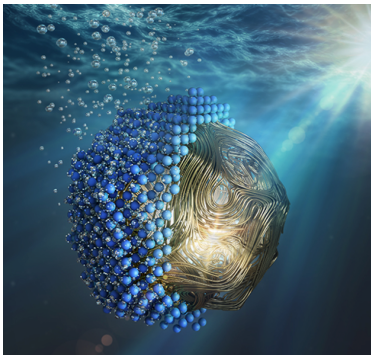

When plasmon resonances are excited in a plasmonic material, incident radiation is strongly scattered, leading to an increase in the scattering cross-section of the material. This scattering process can also lead to the production of hot-electrons, which are high-energy electrons that are excited by the plasmon resonance and are ejected from the material a.k.a hot-electrons. The energy of the hot-electrons is related to the energy of the incident radiation and the energy of the plasmon resonance. Materials that exhibit strong plasmon resonances can absorb a significant amount of energy from the incident radiation, leading to the production of hot-electrons with energies in the visible or even ultraviolet range. The upcoming section is aimed to explore the generation and harvest of the hot-elections.

Plasmonics modes, which are photon states coupled to the oscillations of electrons in metallic structures, are highly desirable for applications requiring small mode sizes and high electromagnetic field enhancements, such as bio and chemical sensors, solar cells, and photodetectors. The efficiency of trapping and concentrating light by surface plasmons has led to a wide range of applications, as demonstrated by numerous reviews in recent years [36–38]. Localized surface plasmons, a type of standing wave variation of surface plasmon polaritons, can be achieved in carefully designed nanostructures using advanced fabrication techniques like electron beam lithography (EBL). The ability to design such nanostructures with a high degree of flexibility has contributed to the rapid and extensive growth of this field [39–43].

Recently, there has been renewed interest in investigating the generation and behavior of "hot-electrons" within plasmonic nanostructures. hot-electrons refer to electrons that have been photoexcited and possess energy higher than what can be provided by a thermal excitation at ambient temperature. When photons are absorbed, and the Localized

Surface Plasmon Resonance (LSPR) in the nanostructure is excited, the electromagnetic decay can proceed through either the re-emission of photons (scattering process) [44] or non-radiatively, by transferring energy to the electronic cloud. Different theories have been developed to describe this process, and researchers are exploring new possibilities for reaction-driven plasmonic applications (Figure 3.2). hot-electrons have the potential to stimulate a variety of thermal, electrical, mechanical, and chemical processes [35, 45]. The photoemission process is a well-known and extensively studied process that involves hot-electrons because it provides valuable information about the energy level distribution inside a material and its surface properties. However, only a small number of the photoexcited hot-electrons can be extracted from the material, as these extraction processes compete with faster carrier relaxation ones. The fast relaxation processes that convert carrier energy into heat are the limiting factor in the use of hot-electrons for chemical or physical processes at the metal surface. The energy of a hot electron can be defined as positive or negative depending on its energy with respect to the vacuum level. In the case of negative hot electron energy, the electron is bound to the nanostructure as the acquired energy is not high enough for extraction. However, such electrons with higher energy than those arising from simple thermal excitation are of particular interest in chemical and charge transfer applications, as they can fill unoccupied levels of acceptor molecules adjacent to the metal surface or induce a photochemical transformation.

Plasmons offer several advantages in generating hot-electrons, such as the ability to customize the carrier energy distribution and localize carrier generation spatially. The generation process can be controlled with a high degree of precision, influencing the resulting photo-excited process. Studies are exploring the microscopic mechanisms of plasmon decay [46], either using classical models or incorporating quantum effects, as plasmons are fundamentally quantum mechanical [47, 48, 48]. However, to capture effects beyond the free electron limit, ab-initio calculations considering the entire electronic band structure are necessary. As energy transfer processes occur on different time scales and device sizes vary, it is challenging to develop a unifying theory.

3.2.1 Hot-electron generation

The decay of a plasmon generates electron-hole pairs with zero net crystal momentum, and this process occurs only above a certain interband transition energy through a direct absorption process. At lower interband energy, absorption and emission of phonons allow the plasmon decay to conserve momentum and excite different electronic states via an indirect absorption process. Plasmon excitation can cause localization of electronic states in a nanoscale system, which imposes an uncertainty on the momentum eigenstates according

to the Heisenberg principle. This localization in space allows for a finite probability of direct plasmon decay, resulting in the generation of an electron-hole pair with finite momentum and energy lower than the interband threshold, a process known as geometry-assisted intraband transition [46]. The momentum difference for this transition is provided by the nanostructure. To fully understand the processes involved in hot carrier generation, it is essential to consider material properties, energy bands, and geometry effects, as they all play a crucial role in the phenomenon [49].

Various theoretical approaches are commonly employed to describe the different factors contributing to the generation of hot carriers, and a comprehensive model requires an understanding of the associated parameters. The quantum mechanical treatment of the geometry effect is often utilized, wherein the free electron model is widely used. This model involves solving the Schrödinger equation for electronic states in the geometry, and then applying Fermi's golden rule to calculate the transition rate between these states [50]. The material effects are linked to the band structure, with direct transitions being particularly influenced by Fermi's selection rule. The energy effects define which type of process dominates in the excitation of hot carriers based on the structure considered. For instance, direct transitions are dominant above the interband threshold, even for small particles (around 10 nm), while phonon-assisted and geometry-assisted intraband transitions compete below this threshold. Thus, a combination of ab-initio and free electron calculations is required to comprehend the various contributions involved in the plasmon decay process.

3.2.2 Hot-electron transport and harvest

The probability of generating hot carriers is finite and occurs with a specific distribution of initial momenta at any location within the plasmonic material. As shown in Figure 3.2,these carriers move through the material and undergo scattering events with electrons, phonons, and crystalline defects, leading to thermalization and a condensed energy distribution around the Fermi level. However, for practical applications of hot carriers, higher energy levels are necessary to effectively drive reactions in molecules or overcome Schottky barriers towards semiconductors. The main challenge in plasmonic hot carrier applications is collecting the carriers before they undergo scattering processes that reduce their energy [51].

The transport of carriers in a material is commonly analyzed in either ballistic or diffusive regimes. Ballistic transport occurs when the carrier moves without being scattered within the characteristic dimension of the nanostructure. Diffusive transport, on the other hand, involves small perturbations from the Fermi-Dirac distribution to describe variations in the carrier's energy as a function of space. Plasmonic structures typically operate in

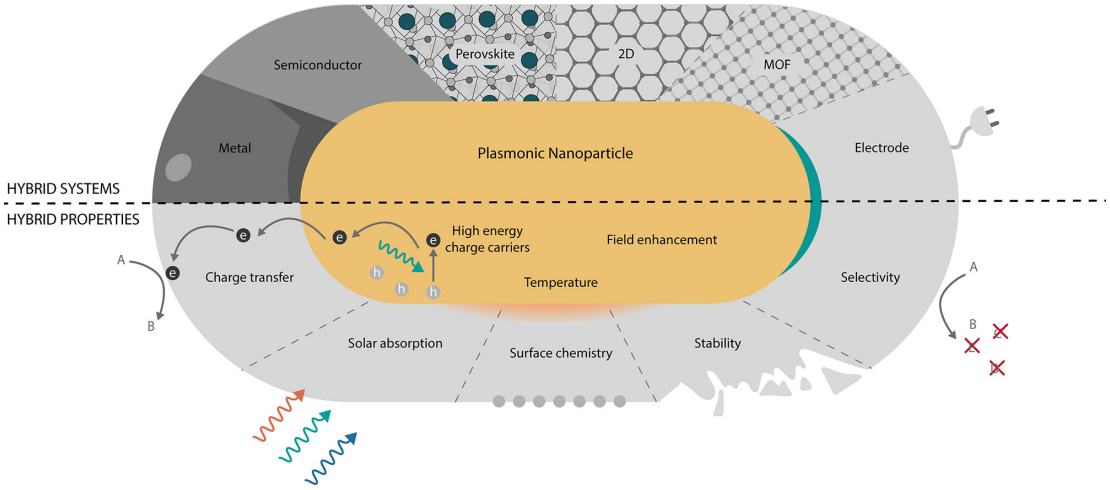

Figure 3.2: Hot-electron generation and harvest. The plasmonic component can not only generate but also harvest light and transfer the energy through charge carriers, heat, and electromagnetic fields. Non-plasmonic materials can add or enhance catalytic properties. The hybrid system can show enhanced stability, selectivity, or activity through various mechanisms, e.g., effective charge transfer, surface chemistry, or enhanced absorption.

an intermediate regime between these two regimes and are analyzed using the Boltzmann equation, which takes into account spatial dependencies. This approach allows for a more accurate description of carrier transport in plasmonic structures. [46].

One of the direct methods to measure hot-electron is through ultrafast pump-probe measurements, which reveal the evolution of excited carriers' energy distribution over time. These studies show an initial rapid rise in the pump-probe signal due to electron-electron scattering, followed by a slower decay due to electron-phonon scattering. This behavior is described by the "two-temperature model", which assigns different temperatures to the electrons and the lattice. By using this model, it is possible to estimate electron and phonon coupling strengths and relaxation times [52]. However, this information only applies to the already thermalized electron distribution, not revealing how to utilize hot carriers. To fully understand the transport of plasmonic hot carriers and their distribution, the Boltzmann equation must be solved in spatial terms. Ab-initio calculations show that the energy is uniformly distributed between zero and the Fermi level after excitation [53]. Thus, all electrons excited through collisions should be considered hot carriers. As more energetic carriers can drive reactions more easily, it is important to understand how hot carriers diffuse and lose energy within the plasmonic structure. By understanding the transport mechanism, it is possible to design the distance at which energetic carrier extraction should occur.

The discussion about energetic charge carriers typically revolves around their collec-

tion and utilization for photochemical transformations, particularly for chemistry-related purposes. Plasmons can produce a substantial amount of energetic charge carriers due to their high field, which can trigger a photochemical reaction either by locally heating the system or by injecting energetic charges into the adsorbed reactants. This information is relevant to applications involving the utilization of energetic charge carriers [52].

Chemical reactions in nanoparticles can be initiated through two primary mechanisms: phonon-driven and charge carrier-driven [52]. In phonon-driven reactions, the nanoparticles' phonon modes are excited by energetic carriers, leading to a coupling with the adsorbate's vibrational modes. This coupling results in a transfer of energy from the nanoparticle to the adsorbate, enabling the transformation of the adsorbate from a reactant to a product state while maintaining the system in the ground state. The ground state free energy and the nanoparticle's temperature control this type of reaction. On the other hand, charge carrier-driven reactions use excited charge carriers to temporarily populate electronic states that may not be populated otherwise. These transient ions induce forces on the adsorbate molecule, leading to nuclear motion that facilitates a chemical transformation. This mechanism is known as desorption induced by electronic transitions (DIET), and it requires the coupling between the excited carrier state and the adsorbate's degrees of freedom. Charge carrier-driven reactions can selectively increase the adsorbate temperature with respect to the nanoparticle's phonon temperature and other adsorbate vibrational [54]. However, the need for high-intensity light on bulk metal surfaces makes charge-driven chemical reactions on metals challenging for practical applications. On the other hand, plasmon excitation and high yield of carrier generation in nanoparticles make it possible to induce charge-carrier reactions. Bimetallic nanoparticles, consisting of a plasmonic material core (such as Ag and Au) and a more chemically reactive metal shell (like Pt and Pd), can also initiate charge-carrier reactions. For instance, studies have shown that charge-carrier conversion is essential in activating the oxidation reaction on the surface of a cluster of small Ag nanocubes [55,56]. Additionally, charge-driven reactions have been reported in the reduction of nitroaromatic compounds absorbed on 6 nm Au nanoparticles illuminated by UV-vis light [57].

Excited carriers can transfer through either direct or indirect mechanisms, with the latter occurring when the energetic charge carriers are formed on the nanoparticle's surface before being transferred to the adsorbate [58]. Energetic carriers undergo rapid relaxation processes, quickly thermalizing to energies near the Fermi level within hundreds of femtoseconds. The resulting thermalized carriers have longer lifetimes, which increases the likelihood of their transfer to the orbitals surrounding the Fermi level of the material. The direct charge transfer mechanism, also known as chemical interface damping, is associated with the coupling of plasmons to the available level of the adsorbate, resulting

in scattering of charge carriers through the adsorbate state [52, 58]. Despite considerable research efforts, there remain unresolved questions regarding the attachment of charges to adsorbates on the surface of excited nanoparticles. Further research is required to develop comprehensive models that accurately describe these complex charge-carrier driven transformations [59–62].

3.3 Controlling plasmonic chemistry pathways through specific ion effects

Published in: "Controlling Plasmonic Chemistry Pathways through Specific Ion Effects" Advanced Optical Materials (2022) [63]
Andrei Stefancu, Lin Nan, Li Zhu, Vasile Chiș, Ilko Bald, Min Liu, Nicolae Leopold, Stefan A. Maier, and Emiliano Cortés.

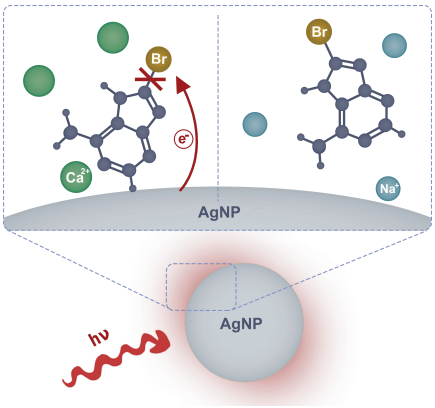

The previous section covered the capability of enhancing fields and generating hot-electrons in plasmonic nanoantennae. The upcoming sections demonstrate how these abilities are utilized in enhanced spectroscopy and activating photocatalytic activity.

Plasmon-driven dehalogenation of brominated purines has been recently explored as a model system to understand fundamental aspects of plasmonassisted chemical reactions. Here, it is shown that divalent Ca2+ ions strongly bridge the adsorption of bromoadenine (Br-Ade) to Ag surfaces. Such ionmediated binding increases the molecule's adsorption energy leading to an overlap of the metal energy states and the molecular states, enabling the chemical interface damping (CID) of the plasmon modes of the Ag nanostructures (i.e., direct electron transfer from the metal to Br-Ade). Consequently, the conversion of Br-Ade to adenine almost doubles following the addition of Ca^{2+}. These experimental results, supported by theoretical calculations of the local density of states of the Ag/Br-Ade complex, indicate a change of the charge transfer pathway driving the dehalogenation reaction, from Landau damping (in the lack of Ca^{2+} ions) to CID (after the addition of Ca^{2+}). The results show that the surface dynamics of chemical species (including water molecules) play an essential role in charge transfer at plasmonic interfaces and cannot be ignored. It is envisioned that these results will help in designing more efficient nanoreactors, harnessing the full potential of plasmon-assisted chemistry.

Until recently, the plasmonic chemistry community focused mainly on Landau damping as the primary electron/energy transfer from plasmonic nanostructures to adsorbed molecules [49, 50, 64, 65]. In the context of surface plasmon resonance, Landau damping represents the scattering of hot-electrons (electrons with energy greater than the thermal energy) at the surface of nanostructures [66, 67] (thus, it scales with 1/R for spherical nanostructures, where R is the radius [68]). Nonetheless, despite the enormous efforts

and advances to increase the efficiency of chemical reactions through Landau damping, the efficiency of such reactions remains low. The low efficiency is mainly due to the unavoidable losses in the metals (provided by bulk scattering, electron-electron scattering, and thermalization of hot elecrons), which often surpass the energy gain provided by the plasmon resonance modes [69–71].

Therefore, the plasmonic community started slowly to shift focus from Landau damping to chemical interface damping (CID) as the primary pathway for electron/energy transfer from plasmonic nanostructures to adsorbates [72–74]. Contrary to Landau damping, which is a multistep effect (first, the electrons are excited above the Fermi level, then they are scattered at the surface of the nanostructures, where they can be transferred to adsorbed molecular orbitals), CID represents the direct electron transfer from the Fermi level to the adsorbate energy state, conditioned by an overlap between the metal states and the adsorbate states (i.e., hybridization) [75, 76]. It was shown recently that CID can lead at least to the same charge transfer effciency as Landau damping and even become the dominant charge transfer mechanism in some systems.

Nonetheless, a prerequisite for both Landau- and CID-assisted charge transfer to molecules is for the molecules to be adsorbed closely to the surface of the plasmonic nanostructures or adsorbed directly on it, in the case of CID. In the surface-enhanced Raman scattering (SERS) effect for example (which requires the same condition, since the electromagnetic fields decay with r^{-10} from the metal surface), the low adsorption affinity of many target molecules is a well-known hurdle toward their sensitive detection. Examples of this include glucose (whose direct label-free SERS spectrum was not yet achieved) [77], water molecules [78, 79] (with very modest enhancement factors despite the fact that most SERS studies are done in aqueous solvents), or organic acids [80], among other examples. The surface effects which deal with the dynamics of chemical species at the surface of nanostructures usually receive very little attention compared to Landau damping or CID. However, as in the above examples regarding SERS detection, such surface effects and surface dynamics often dictate the interaction between molecules and nanostructures and cannot simply be ignored or assumed negligible.

Our recent SERS studies [81–83] provide evidence that specific ion effects control the selective adsorption of molecules onto colloidal silver nanoparticles (AgNPs). As a rule of thumb, the addition of positively (Ca^{2+}, Mg^{2+}), or negatively (Cl^-), Br^-) charged ions [84,85] leads to the selective adsorption of negatively and positively charged molecules, respectively on the surface of AgNPs. Most often, the Derjaguin-Landau-Verwey- Overbeek (DVLO) theory is used to model the interactions of ions with colloidal nanoparticles (NPs) and surfaces in general. However, the predictions of the DVLO model are often refuted by experiments which show that certain ions interact specifically with colloidal nanoparticles

and surfaces, leading thus to specific ion effects [86–88].

In this study, we aim to explore such specific ion effects in the plasmon-assisted dehalogenation reaction of 8-bromoadenine (Br-Ade) to adenine (Ade) on Ag surfaces. As far as we know, the way in which specific ion effects impact plasmon- assisted reaction rates has never been studied before. The dehalogenation of Br-Ade to Ade has been studied extensively by the Bald group [89–93] and, importantly, a thermal-driven reaction has been excluded through power-dependent measurements as well as in studies using nanosecond laser pulses, suggesting that the main electron transfer pathway from AgNPs to Br-Ade is a plasmon-assisted one. This is also confirmed by afirecent study using in-situ electrochemical SERS [94].

Here we show that divalent Ca^{2+} and Mg^{2+} ions increase the dehalogenation rate of Br-Ade by specically bridging its adsorption on silver nanowires (AgNW) and thus increasing the adsorption affinity of Br-Ade to the Ag surface. Contrary, monovalent Na^{+} does not affect the reaction rate. These experimental results show conclusively how specific ion effects and the dynamics of chemical moieties at the NPs surface impact plasmon-assisted chemical reactions at the nanoscale. Moreover, based on these results, we can indirectly suggest which plasmon-assisted charge transfer mechanism dominates, since Landau damping and CID should be affected differently by the surface chemistry and surface effects.

3.3.1 Specific-ion effects on silver

We start first by characterizing the nanosubstrate used throughout this study. Silver nanowires (AgNW) were synthesized from concentrated citrate capped AgNPs colloidal solution (obtained through the Lee-Meisel method [95]) through convective self-assembly [96] (CSA). To obtain the AgNWs separated by a well-defined distance, we used the stop-and-go method [97] (more details in the Experimental Section). Figure 3.3 shows schematically the synthesis process, together with a representative optical image of the obtained substrate. Figure 3.3 (c-e), show that the SERS intensity of Ade adsorbed on the AgNW is uniform across the surface of the AgNW, thus offering a reproducible substrate for testing the Br-Ade dehalogenation. Next, we monitored the SERS intensity of Br-Ade with and without Ca^{2+} (in the form of $Ca(NO_3)_2$ salt) by using the AgNW substrate. We show in Figure 3.5 (a,b) that the adsorption affinity of Br-Ade for the Ag surface increases significantly in the presence of Ca^{2+}, leading consequently to an increase of the SERS intensity of Br-Ade. For monitoring the time-dependent SERS intensity of Br-Ade, the AgNW substrate immersed in a Br-Ade solution with and without Ca^{2+}, respectively, was placed under the Raman microscope and SERS spectra were acquired, periodically, from the same spot on the AgNW. Since the acquisition time of each SERS spectrum was 1 s

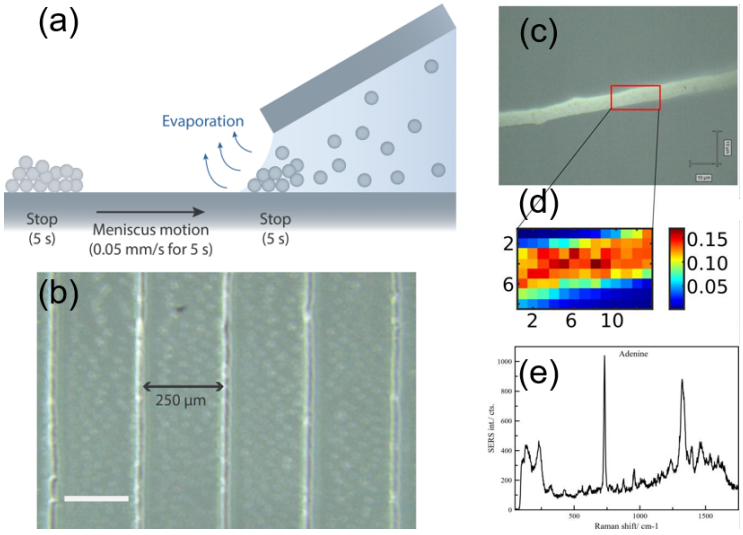

Figure 3.3: Characterization of the AgNW substrates. (a) Scheme of the stop-and-go process for synthesizing the AgNW. (b) Optical image of a representative AgNW substrate. The scale bar represents 200 μm. (c) Optical image of a representative silver nanowire (AgNW) taken with the 100x magnification microscope objective. (d) Normalized SERS intensity of Adenine (0.1 mM) mapped on the marked region acquired with the 633 nm laser, showing the uniformity of the SERS signal across (e) The SERS spectrum of Adenine.

(laser power 9 mW) and the time gap between consecutive acquisitions was on the order of minutes, no dehalogenation reaction of Br-Ade was observed (i.e., the decrease in the intensity of 760 cm^{-1} peak and increase in the 730 cm^{-1} SERS peak).

Figure 3.4(a-b) show the increase of the SERS intensity of Br-Ade after the addition of Ca^{2+} on two other substrates, confirming the increased adsorption affinity of Br-Ade after the addition of Ca^{2+}. These results are in line with previous SERS studies on the selective adsorption of positively and negatively charged molecules on AgNPs, due to adsorbed ions. Moreover, in Figure 3.4 (c), we show the calculated adsorption energy of Br-Ade on Ag(111) with and without Ca^{2+}. The adsorption energy increases from -0.58 to -1.05 eV upon the addition of Ca^{2+} ions.

At this point, we can start suggesting possible mechanisms for the results observed in Figure 3.5. Let us consider for a moment the structure of the electrical double layer at the Ag surface, and the mechanism of adsorption of like-charged molecules. A negatively charged Ag surface (due to the citrate surfactant) will adsorb charged ions, specifically and nonspecifically. Specifically adsorbed ions can possess a chemical or specific affinity for the Ag surface, whereas the nonspecifically adsorbed ions are attracted to the surface by purely Coulombic forces [97]. The plane defined by the specifically adsorbed ions defines the inner Helmholtz plane, while the hydrated ions adsorbed on the surface define the outer

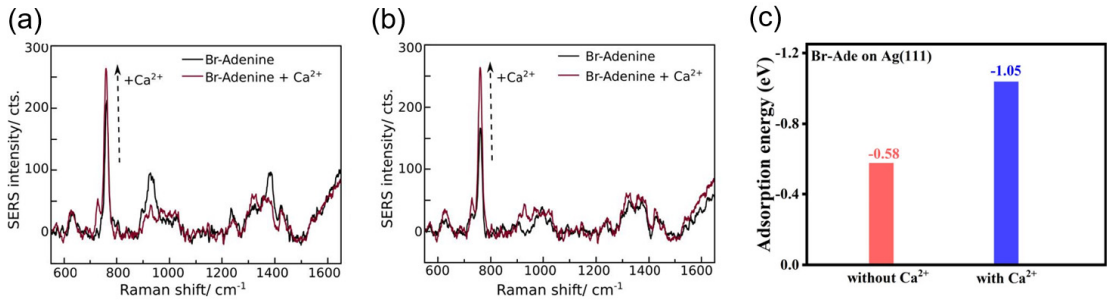

Figure 3.4: (a and b) The increase of the SERS intensity of Br-Ade on AgNW after the addition of Ca^{2+} on two independent AgNW substrates, suggesting an increase adsorption affinity of Br-Ade.(c) The calculated adsorption energy of Br-Ade on Ag(111) with and without Ca^{2+} ions, in an aqueous environment.

Helmholtz plane. Together they define the first layer of the electrical double layer. The second layer is called the diffuse layer and is located further away from the surface [98]. The presence of cationic species, such as Ca^{2+}, has been shown to decrease the magnitude of the negatively charged surface's zeta potential (which quantifies the variations in the electric double layer's charge) by increasing the positive charge density located in the first electrical double layer [99]

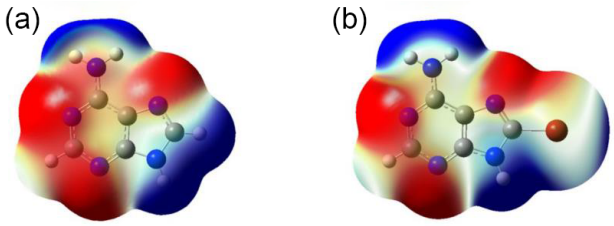

Figure 3.6: The molecular electrostatic potential maps of (a) Adenine and (b) 8 bromoadenine(Br-Ade). The red color indicates high electron density, whereas blue indicates low electron density. In the Br-Ade molecule, due to the Br atom, the molecule's charge density changes, with an electron build-up surrounding the Br atom, changing thus its dipole moment. Courtesy of Prof. Vasile Chis, from Babes-Bolyai University, Romania.

Let us consider now the adsorption of Br-Ade to the negatively charged Ag surface, shown schematically in Figure 3.5 (c-d). Due to the presence of the bromide atom, the charge distribution of Br-Ade changes compared to Ade (as shown by the molecular electrostatic potential maps in Figure 3.6, leading to a change in the dipole moment of Br-Ade compared to Ade. For adsorption to occur, Br-Ade must overcome Coulombic repulsion via hydrophobic interactions or be facilitated by the screening of counterions. If the attraction of Br-Ade to the surface overcomes repulsive forces, then the adsorption proceeds in time. Thus, within this framework, we can interpret our SERS results (and dark-field

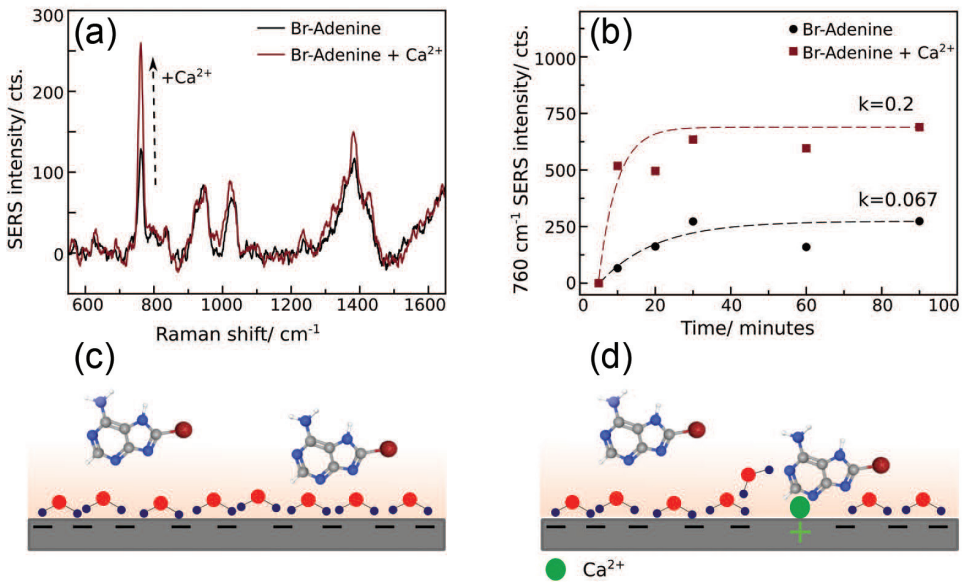

Figure 3.5: (a) A representative example of the increase of Br-Ade SERS intensity following the addition of Ca^{2+}. The SERS spectra were taken with the 785 nm laser, on the AgNW substrate. (b) The increase of the SERS intensity of 760 cm^{-1} SERS peak of Br-Ade on AgNW with and without Ca^{2+}, monitoredin time, at 785 nm excitation (1 s integration time, 9 mW). Due to the low integration time and high time-spacing between acquisitions (i.e., minutes), no dehalogenation of Br-Ade occurred. The time-dependent SERS intensity was fitted with a Langmuir curve (the dotted lines), yielding the adsorption constants of Br-Ade with Ca^{2+} ($k = 0.2$) and without Ca^{2+} ($k = 0.067$). (d) Schematic view of the adsorption of Br-Ade on the Ag surface without $Ca2^{2+}$ and (d) with the addition of Ca^{2+}, which leads to surface charge reversal locally. The shaded orange region represents the hydration layer of the Ag surface, while the negative charge of the Ag surface is given by the citrate surfactant.

scattering (DFS) results shown in Figure 3.11) as follows. Ca^{2+} ions increase the positive charge density in the first electric double layer at the AgNW surface, and thus decrease the Coulombic repulsion between the negatively charged Ag surface and Br-Ade, bridging the specific adsorption of Br-Ade. In fact, divalent ions such as Ca^{2+} or Mg^{2+} have been shown to reverse the local surface's charge (an effect called charge reversal), whereas monovalent ions such as Na^{+} or K^{+}, cannot counteract the surface's charge, although they increase the positive charge density in the first electrical double layer [100] In our case, the citrate capping layer of the AgNPs did not influence the adsorption of Br-Ade on AgNPs since there are no strong SERS bands of citrate in the spectra. This suggests that Br-Ade has a stronger affinity for the Ag surface than citrate.

At a more fundamental level, these surface ion specific effects are related to the Hofmeister

series, and the local water structure. The Hofmeister series is an empirical sequence describing the efficiency of different salts in precipitating proteins and suspensions in general (such as colloids) and since its report it left physical-chemists eluded as to what dictates this series. The Hofmeister series was then extended to describe interactions of ions with metal and organic surfaces; however, the mechanism remains partially known, at best [101–103] Until now, the best guess is that ions leave the bulk structure of water intact, however, they modify the local water shell around surfaces or proteins. In our case, Collin's law of matching water affinities applies [104] It states that the hydration shell of two cosmotropic ions may overlap, leading to ion pairing. However, a chaotropic ion may not penetrate the hydration shell of a cosmotropic ion. Consistent with this law, we can assume that strongly hydrated cosmotropic ions, such as Ca^{2+} or Mg^{2+}, can penetrate the surface hydration layer of Ag, while weakly hydrated chaotropic ions, such as Na^{+} or K^{+}, are excluded from the surface layer. Moreover, theoretical and experimental results have suggested that the cosmotropic ions are to some degree dishydrated (or even completely dishydrated), allowing close contact between the bare ion and the surface, analogous to close contact ion pairing between two cosmotropic ions in solution. Therefore, Ca^{2+} ions can bridge the adsorption of Br-Ade very close to the Ag surface.

3.3.2 Controlling chemical pathways

Next, we bring experimental evidence that Ca^{2+} ions, besides leading to an increase of the SERS intensity of Br-Ade, also increase the conversion of Br-Ade to Ade by a factor of ~ 2. We acquired time-series SERS measurements with the 785 and 633 nm lasers, for ~ 30 s (0.5 s integration time with 0.5 dwell time in-between acquisitions) and tracked the reaction dynamics of Br-Ade to Ade. The intensity of the SERS marker peaks at 760 cm^{-1} (for Br-Ade) and 730 cm^{-1} (for Ade) were used to quantify the conversion rate. The peak at 760 and 730 cm^{-1} were assigned by us to the ring breathing mode of Br-Ade and Ade, respectively, through density functional theory (DFT) calculations.

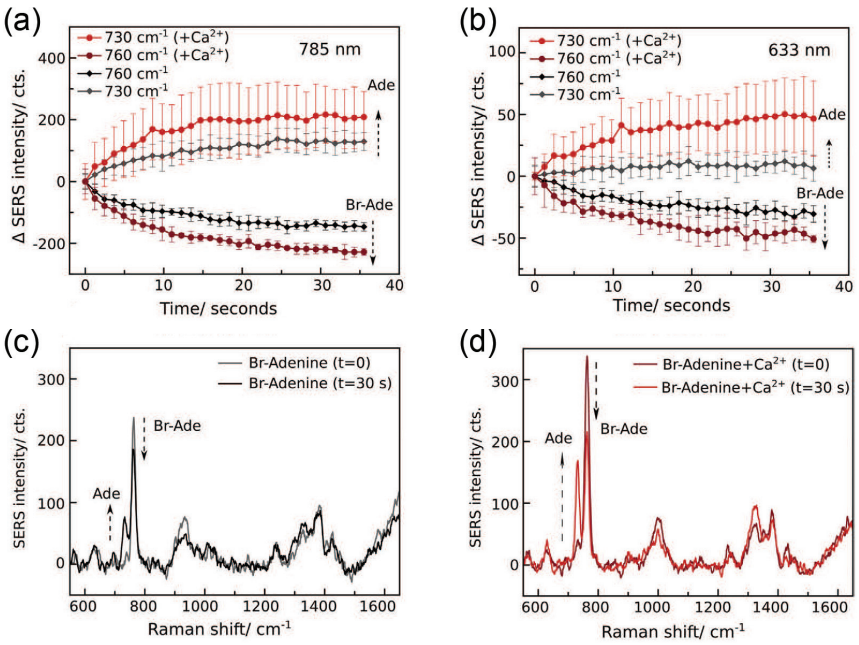

Figure 3.7: The dehalogenation of Br-Ade to Ade monitored through the time evolution of the SERS intensity of 760 and 730 cm^{-1} peaks, respectively. The Δ SERS (i.e., Intensity$t_{>0}$ − Intensity$_{t=0}$) for the 730 and 760 cm^{-1} peaks without Ca^{2+} (gray and black lines, respectively) and with Ca^{2+} added(deep red and light red, respectively) for (a) 785 nm and (b) 633 nm irradiation. In both cases, the 760 cm^{-1} SERS peak intensity decreases while the 730 cm^{-1} SERS peak intensity increases, corresponding to the conversion of Br-Ade to Ade. Moreover, in both cases, the conversion is significantly greater (almost twice) following the addition of Ca^{2+}. The bars represent the standard deviation from five measurements on different AgNW. (c-d) Representative SERS spectra (785 nm laser) of the first and last spectrum in the time series measurements, showing a significantly higher conversion rate of Br-Ade to Ade following the addition of Ca^{2+} (d). Also, note the higher SERS intensity of the 760 cm^{-1} peak at t = 0 in (d) compared to (d).

Figure 3.7 shows the dynamics of Br-Ade to Ade reaction during irradiation with 785

and 633 nm, through the difference in the SERS intensity of the 730 and 760 cm^{-1} peaks, with and without the addition of Ca^{2+}. In addition, Figure 3.8(a-b) shows the time-series SERS measurements from two other substrates with 785 nm irradiation, all showing the same outcome: Ca^{2+} increases the conversion of Br-Ade to Ade. Note that, since our analysis was based on the difference in the SERS intensity relative to the starting point (noted ΔSERS intensity in Figure 3.7), the results are independent of the initial SERS intensity of the 760 or 730 cm^{-1} peaks.

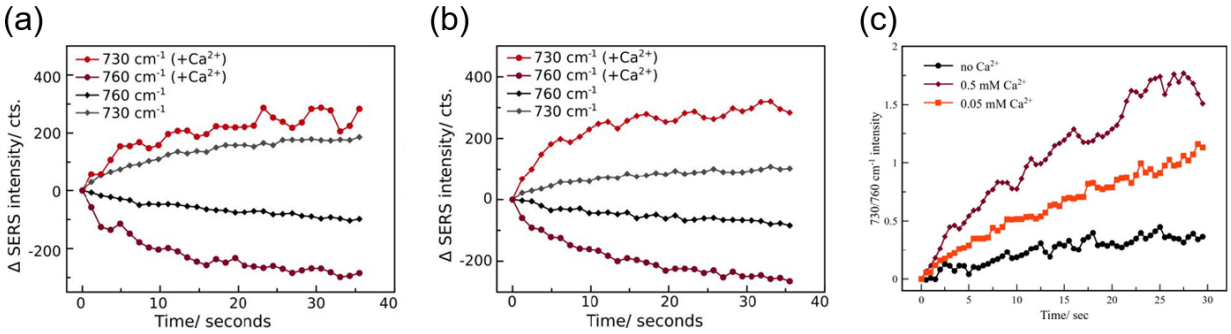

Figure 3.8: The dehalogenation of Br-Ade to Ade monitored through the SERS intensity of 730 and 760 cm^{-1} peaks. The ΔSERS (i.e., Intensityt¿0-Intensityt=0) for the 730 and 760 cm^{-1} peaks without Ca^{2+} added (gray and black lines, respectively) and with Ca^{2+} added (deep red and light red, respectively) for 785 nm excitation for two AgNW independent substrates. In both cases, the conversion rate is significantly greater (by a factor of 2) following theaddition of Ca^{2+}. (c) The conversion rate of Br-Ade to Ade without Ca^{2+}, with 0.5 mM C^{2+} and 0.05 mM Ca^{2+} final concentration. The measurements were performed with the 785 nm laser, consisting in 60 acquisitions and 0.5 sec per acquisition.

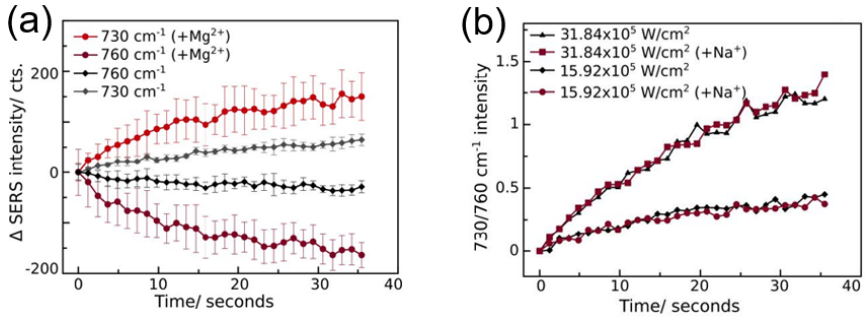

Figure 3.9: (a) The dehalogenation of Br-Ade to Ade under excitation at 785 nm, monitored through the SERS intensity of 730 and 760 cm^{-1} peaks by using Mg^{2+} ions (in the form of $MgSO_4$).(b) The dehalogenation of Br-Ade to Ade under excitation at 785 nm, monitored through the SERS intensity of 730/760 cm^{-1} by using Na^{+} ions (in the form of Na_2SO_4).

Mg^{2+} addition led to the same results as Ca^{2+}, increasing the dehalogenation rate of Br-Ade to Ade (Figure 3.9(a)), whereas Na^{+} did not lead to any significant changes (Figure 3.9(a)). This further supports the mechanism of divalent cations bridging the adsorption of Br-Ade to the Ag surface.

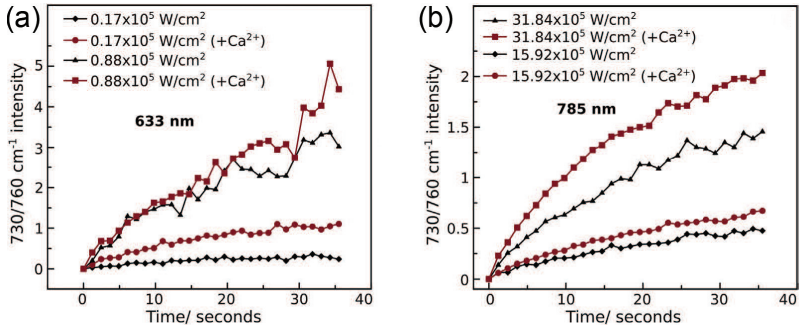

Figure 3.10: The conversion rate of Br-Ade to Ade at (a) 633 nm and (b) 785 nm excitation, for two laser power densities, quantified through the 730/760 cm^{-1} SERS intensity.

In order to quantify the dehalogenation rate of Br-Ade, we plotted the 730/760 cm^{-1} SERS intensity, which corresponds to the rate of Br-Ade conversion to Ade for 785 and 633 nm irradiation, at two different laser powers (Figure 3.10). First, it is evident that at 633 nm excitation the conversion rate is higher than at 785 nm, even though the power density is lower. This is due to the higher absorption of the AgNW at 633 nm, compared to 785 nm. Second, the addition of Ca^{2+} increases the Br-Ade to Ade conversion in all cases.

By fitting the experimental curves in Figure 3.10 with a fractal reaction kinetic model, we determined the reaction rate, k, for 633 and 785 nm. For 633 nm (0.17×10^5 W/cm^{-2}) we obtained a reaction rate of 0.023, which increased to 0.07 after the addition of Ca^{2+}. Likewise, for 785 nm (31.84×10^5 W/cm^{-2}) we obtained a reaction rate of 0.082, which increased to 0.11 after the addition of Ca^{2+}.

However, one must be careful in quantifying the dehalogenation rate through the ratio 730/760 cm^{-1} SERS intensity, since multiple effects can lead to a change in the SERS intensity. Particularly, in our case, for the 785 nm excitation, the decrease of 760 cm^{-1} peak intensity (i.e., Br-Ade dehalogenation) is symmetric with the increase of the 730 cm^{-1} peak intensity (Figure 3.7(a)). This suggests that indeed Br-Ade molecules were converted to Ade with a one-to-one ratio. However, for 633 nm excitation (Figure 3.7(b), without Ca^{2+}), the decrease of the 760 cm^{-1} peak intensity was always greater than the increase in the 730 cm^{-1} peak intensity. This result hints at a desorption induced by electronic transitions mechanism in addition to the Br-Ade conversion to Ade. Thus, at 633 nm, charge transfer from the Ag surface to Br-Ade will take place, and the kinetic energy of

the electrons imparted to Br-Ade molecules is high enough to cause desorption of Br-Ade molecules instead of conversion to Ade, resulting in a skewed time-evolution of the 760 and 730 cm^{-1} SERS intensity. We also note here that by irradiating the AgNW with 633 nm and higher power density (0.88×105 W/cm^{-2}), the effects of Ca^{2+} on the dehalogenation rate of Br-Ade are smaller compared to those when using 785 nm excitation (Figure 3.10(a)). We suspect that this is a result of two effects: i) thermal effects (which are not affected by surface dynamics are Ca^{2+} ions) could contribute to the dehalogenation of Br-Ade to Ade and ii) Landau damping could become the dominant charge transfer pathway at 633 nm wavelength, whereas at 785 nm in the presence of Ca^{2+} ions CID drives the reaction (see below).

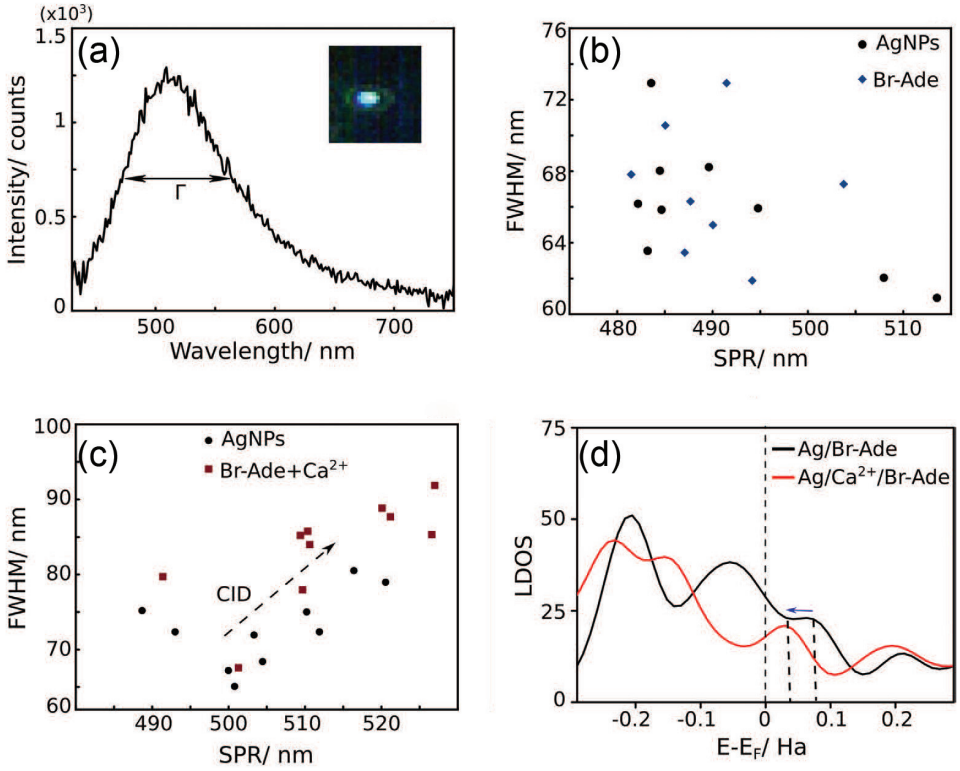

Figure 3.11: Monitoring the adsorption of Br-Ade on AgNPs following the addition of Ca^{2+} by dark field scattering (DFS). (a) A typical dark field scattering spectrum of AgNPs ($\sim$ 100 nm diameter) with 40x air objective, after normalization to the lamp spectrum. The scattering spectrum is characterized by a Lorentzian curve, with full-width-at-half-maximum (FWHM), Γ, and resonant wavelength given by the peak of the scattering spectrum. The resonant wavelength and Γ for ten AgNPs before and after adding (b) Br-Ade and (c) Br-Ade with Ca^{2+}. In the case where Br-Ade and Ca^{2+} were added, the AgNPs evidenced a strong CID effect, through the redshift of the resonant wavelength and an increase of the FWHM (c). In contrast, after the addition of Br-Ade alone, no significant differences were observed (b). (D) The local density of states (LDOS) of the Ag surface with adsorbed Br-Ade and Br-Ade and Ca^{2+}, respectively. A shift of the LDOS of the Ag-Br-Ade complex toward the Fermi level energy can be observed in the presence of Ca^{2+} ions, indicated by the blue arrow.

The increased adsorption affinity of Br-Ade to Ag surface following the addition of Ca^{2+} is also observed in the DFS measurements, shown in Figure 3.11. As mentioned in the Introduction, CID represents the direct electron transfer from the surface plasmon resonance to overlapping molecular orbitals. As a result of this new dephasing pathway, the plasmon resonance will decay faster, broadening the plasmon resonance lineshape in the frequency space. Additionally, a red-shift and decrease in intensity of the plasmon resonance can be observed' however, this depends also on the local refractive index. Therefore,

the broadening of the plasmon resonance is usually conidered a more reliable parameter for quantifying the CID.

In Figure 3.11, we probed the plasmon resonance of ten single AgNPs ($\sim$ 100 nm in diameter) in water and in a solution of Br-Ade and Br-Ade with Ca^{2+}, respectively. For the sample containing only Br-Ade, no significant differences were observed in the resonant wavelength or full-width-at-half-maximum (FWHM) of the surface plasmon resonance of AgNPs (Figure 3.10(b)). For the sample containing both Br-Ade and Ca^{2+} ions, a significant damping (broadening and red-shift) of the surface plasmon resonance was observed (Figure 3.10(c)) compared to the single AgNPs in water (see Figure 3.12). This suggests, as in the case of the SERS results presented in Figures 3.5 and 3.7, that Br-Ade alone is nonspecifically adsorbed at the surface of the AgNPs and, after the addition of Ca^{2+} (or Mg^{2+}), becomes specifically adsorbed, the adsorption being bridged by the Ca^{2+} (or Mg^{2+}) ions. Although the geometry of the AgNW substrates used for the SERS measurements is different from that of the single AgNP used in the DFS experiments, the surface chemistry is the same in both cases. The AgNW were synthesized from citrate capped AgNPs, the same as the AgNPs used in the DFS measurements. Thus, even though the surface plasmon resonance is obviously different on the two nanostructures, the surface dynamics should be very similar.

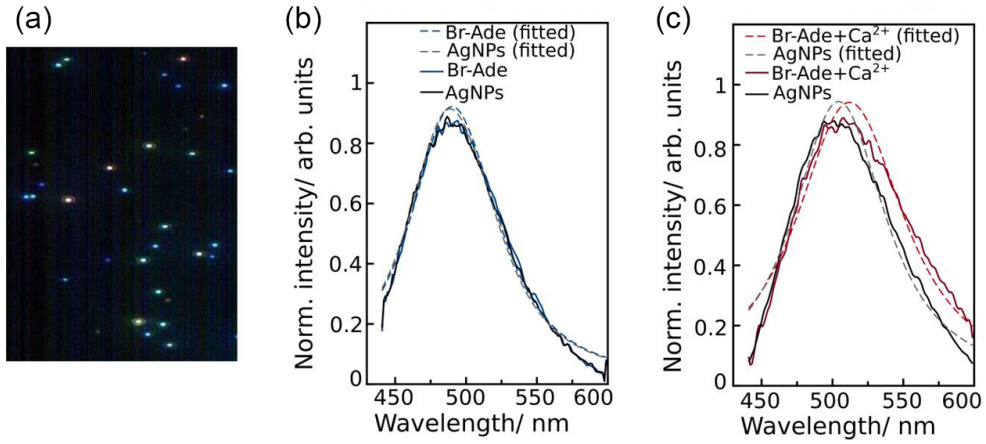

Figure 3.12: (a) A typical dark field scattering (DFS) image of AgNPs, taken with the 40X air objective. (b) The average DFS spectrum of AgNPs before (black curve) and after the addition of Br-Ade (blue curve), and the respective spectra fitted with a Lorentzian curve (dotted curves). (c) The average DFS spectrum of AgNPs before (black curve) and after the addition of Br-Ade and Ca^{2+} (deep red curve), and the respective spectra fitted with a Lorentzian curve (dotted curves). We note that small differences between the experimental and fitted DFS spectra appear due to the averaging over all spectra. However, by inspecting visually each individual DFS spectrum and the fitted Lorentzian curve, an excellent match was found.

CID is associated with the direct electron transfer from the Fermi level of AgNPs to acceptor molecular orbitals, when there is an overlap between the metal and molecular energy states (i.e., chemisorption). An increased damping of the surface plasmon resonance, observed in the case of Br-Ade with Ca^{2+}, suggests a significant CID caused by Br-Ade, due to the increased adsorption afinity provided by Ca^{2+}. Thus, we believe that through Ca^{2+} bridging the adsorption of Br-Ade on Ag surface, Br-Ade shifts from physisorption to chemisorption, facilitating the direct electron transfer from the surface plasmon resonance modes of Ag nanostructures to Br-Ade acceptor orbitals, characteristic of CID. Therefore, the increase in the dehalogenation rate of Br-Ade following the addition of Ca^{2+} is assigned by us to CID (i.e., direct electron transfer transitions), whereas in the lack of Ca^{2+} ions, the dehalogenation reaction is likely driven by Landau damping, as indicated in previous studies (i.e., hot-electrons). By the same token, thermal effects can be disregarded since the addition of Ca^{2+} ions would not influence in any way the temperature of the AgNW upon laser irradiation.

This interpretation is also supported by the shift of the local electronic density of states (LDOS) of Ag with Br-Ade and Ca^{2+} toward the Fermi level energy compared to only Ag with Br-Ade calculated theoretically. Figure 3.11(d) shows the LDOS for Ag (111) with adsorbed Br-Ade and Br-Ade-Ca^{2+}, respectively, with respect to the Fermi level energy of

Ag. We note first the strong contributions from the electronic d-states of Ag at energies below $\sim$ -0.11 Ha (corresponding to $\sim$ -3 eV) [105]. Most importantly, above the Fermi level energy the acceptor electronic states of the Ag/Br-Ade complex are observed at $\sim$ 0.09 Ha ($\sim$ 2.5 eV) which are shifted to $\sim$ 0.05 Ha ($\sim$ 1.36 eV) above the Fermi level energy (as marked by the blue arrow in Figure 3.11(d)). Interestingly, this is very close to the laser energy of the 785 nm laser ($\sim$ 1.5 eV). Therefore, these results could also explain why, at 633 nm excitation, Ca^{2+} ions do not have such a great influence as for 785 nm (see Figure 3.7).

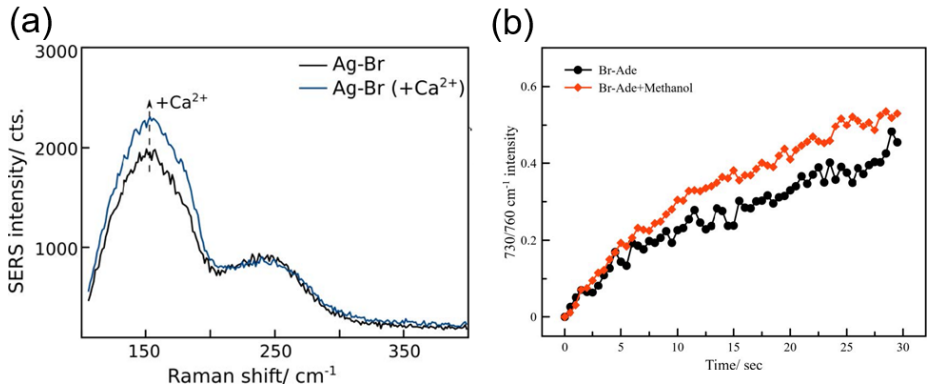

Figure 3.13: (a) The conversion rate of Br-Ade to Ade with and without methanol (15% concentration). The measurements were performed with the 633 nm laser, 60 total acquisitions and 0.5 sec per acquisition. The increased conversion rate in the presence of a hole-scavenger, methanol, indicates that indeed a metal-molecule electron transfer drives the dehalogenation of Br-Ade to Ade.(b) The increase of the Ag-Br SERS intensity following the addition of Ca^{2+} on the AgNW substrates, at 785 nm excitation. The KBr final concentration was 10 mM

To further highlight that the Br-Ade dehalogenation to Ade is driven by a metal-molecule electron transfer process, we tracked the conversion rate of Br-Ade to Ade in the presence of a hole scavenger, methanol (Figure 3.13(a)). The increase in the conversion rate in the presence of methanol supports our hypothesis that the Br-Ade conversion to Ade is driven by an electron transfer process.

For the dehalogenation of Br-Ade to Ade by metal-molecule charge transfer to take place, a counter reaction is needed to scavenge the holes left behind in the metal. It was previously proposed that the Br^- ions that are cleaved o Br-Ade molecules adsorb to the Ag surface, forming AgBr complexes, and act as hole scavengers, facilitating the electron transfer rather than the recombination of the hot-electrons with the corresponding holes in the metal states [83]. To validate this counter reaction, and explore the role of Ca^{2+} ions, we tracked the time-dependent intensity of the Ag-Br SERS band at $\sim$ 150 cm^{-1}. If, after

cleavage, the Br^- ions are adsorbed on the Ag surface, then we should see an increase in the intensity of the Ag-Br SERS band, correlated with the Br-Ade dehalogenation. Therefore, we acquired time-series SERS measurement of Br-Ade on AgNW at 785 nm, this time in the 50–1200 cm^{-1} wavenumber range.

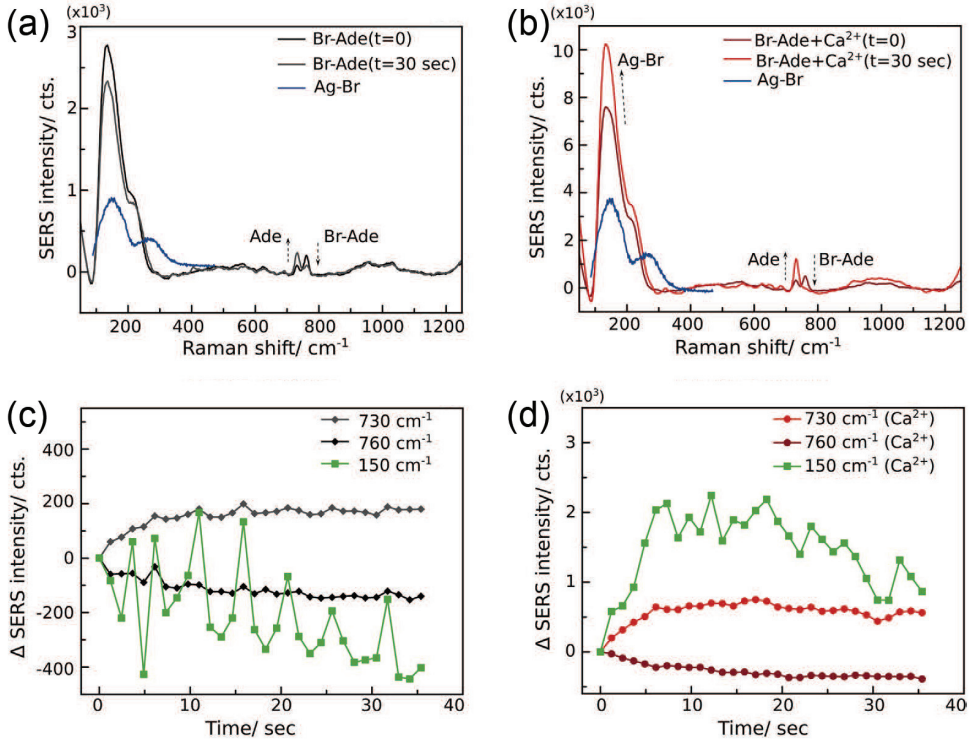

Figure 3.14: The surface dynamics of Br^- ions correlated with the dehalogenation of Br-Ade to Ade. Representative SERS spectra (785 nm laser, 0.5 s acquisition time, and 0.5 s dwell time) of the first and last spectrum in the time series measurements in the 50–1200 cm^{-1} range without(a) Ca^{2+} and (b) with Ca^{2+}, showing an increase of the Ag-Br SERS band at low wavenumbers, correlated to the conversion of Br-Ade to Ade following the addition of Ca^{2+}. The blue spectrum represents the SERS band of Ag-Br, with a maximum at $\sim$ 155 cm^{-1}. The Δ SERS intensity (i.e., $Intensity_{t>0}$ - $Intensity_{t=0}$) for the 730, 760, and 150 cm^{-1} peaks (c) without Ca^{2+} and (d) with Ca^{2+} added. The scatter plot represents the average of three separate measurements.

Figure 3.14 shows that on the AgNW with Br-Ade, the Ag-Br SERS band does not change much during the time-series measurement (Figure 3.14(a,c), only decreasing slightly. On the other hand, following the addition of Ca^{2+} ions, the Ag-Br SERS band increases in intensity significantly (Figure 3.8(b,d)).

In Figure 3.13(b), we show that the Ag-Br SERS peak on AgNW increases after the addition of Ca^{2+}, which is consistent with our earlier SERS studies regarding the adsorption

of negatively charged chemical moieties on AgNPs. This is attributed to the same cation bridging effect discussed above, by which the repulsive Coulombic forces between the Br^- ions and the negatively charged Ag surface are screened by Ca^{2+}.

A hurdle for testing this mechanism more conclusively is that in the same wavenumber region, there is another peak, which could possibly stem from plasmonic electronic Raman scattering in the Ag metal [106]. Thus, the peak at low wavenumbers in Figure 3.14 is probably a convolution of the Ag-Br SERS signal and the electronic Raman scattering from the metal substrate itself. This also explains why the peak at 150 cm^{-1} has such a high intensity. Nonetheless, the plasmonic electronic scattering peak should be constant in time, thus its observed variation in the presence of Ca^{2+} is most likely due to the increase of the Ag-Br SERS peak.

Interestingly, the variations in the Ag-Br SERS intensity (Figure 3.14(c,d)) could stem from the decomposition of the Ag-Br surface complexes under laser irradiation and the formation of Br2 within a few seconds. The results of Figures 3.11 and 3.14 show that both the stronger adsorption of Br-Ade to the Ag surface and the adsorption of Br^- ions to the Ag surface cooperate to increase the plasmon- assisted dehalogenation rate of Br-Ade to Ade under light irradiation.

3.4 Hot-electron meditated photocatalysis

Published in: "Investigating plasmonic catalysis kinetics on hot-spot engineered nanoantennae" Nano Letters (2023) [107]
Lin Nan, Jesús Giráldez-Martínez, Andrei Stefancu, Li Zhu, Min Liu, Alexander O. Govorov, Lucas V. Besteiro, and Emiliano Cortés.

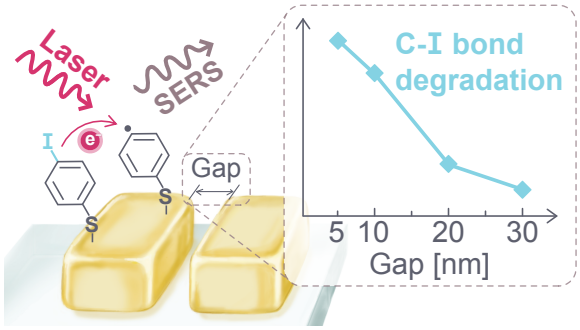

In the previous section, the effect of specific ions to plasmon-meditated photocatalytic dehalogenation was demonstrated. The next section aims to further investigate the roles of the sub-diffraction plasmonic nanostructures in photocatalytic activities.

Strong plasmonic hot-spots can not only facilitate chemical reactions thermally but also drive the chemical reactions by injecting hot-carriers, i.e. electrons and holes with sufficient kinetic energy to leave the metal, towards the reactants upon light illumination. These unique abilities, especially the latter, have been receiving vast attention

and driven a new branch of research focused on plasmon-meditated photocatalysis due to increasing demands for "greener" energy conversion methods. Despite the significant improvements made towards efficient plasmon-driven chemical reactions, it has not yet been able to match with the conventional heterogeneous catalysts [108–110]. To design an efficient plasmonic photocatalysis platform, it is crucial to unveil the role of the hot-carrier in chemical reactions. Theoretical studies have shown the hot-carrier production is highly dependent on the size, shape, and material [50, 111–115]. Even though it is an intrinsic ability of plasmonic nanostructures to generate hot-carriers, the generation rate is predominantly governed by hot-spots that are located at the areas with small curvatures or narrow interparticle distances [113]. In other words, the high energy carrier generation is greater and more tunable in plasmonic structures such as nanorods, nanostars, and dimers as compared to nanospheres. Indeed, photocatalytic degradation of Rhodamine B was almost two times faster for gold nanostars as compared to gold nanosphere and nanorods [116]. The reason to employ plasmonic nanostructures for photocatalysis is that they allow us to concentrate and manipulate the electromagnetic energy inducing a variety of chemical reactions in specially designated hot spots [108, 110, 117], and in addition, may eventually leads to chiral photocatalysis [118].

Although the most studied platforms are of ensemble nature, averaging due to the intrinsic heterogeneity such as morphology dispersion, variable surface reactive sites, dynamic changes of the reaction sites, *etc.* add complexities and ambiguity to the study [108]. Hence, a systematic study with tangible parameters at a single particle level is required [119]. Namely, surface enhanced Raman spectroscopy (SERS) is one of the most powerful methods for systematic investigation on hot-electron meditated catalysis because SERS information allows direct phenomenological observation on hot-carrier dynamics by tracing the photocatalytic reactant and product real-time [120–127]. Yet, low signal-to-noise ratio in single-particle SERS measurements remains a bottleneck. It is well known that SERS intensities are proportional to the square of the local-field intensity and number of the observed molecules. Increasing excitation laser power can help improve signal-to-noise ratio, but this will also destabilize the observed plasmonic structures especially under extended period of illumination. Accordingly, especially for time-dependent single particle studies, fabrication of stable single plasmonic nanoantennae with high local-field enhancement becomes essential. High local-field enhancement, $\sim 10^6$, can be achieved by forming small nanocavities or gaps in between plasmonic nanoparticles, and the most straightforward way to facilitate such strong hot-spots is to form aggregates from colloidal nanoparticles [94, 128, 129]. However, this method often requires molecular spacer on the surface which hinders the accessibiltiy of the Raman molecules. Moreover, due to the random nature of the colloidal aggregates, the precise fabrication of the hot-spots becomes

highly challenging, and thus further elude observed results [90, 129]. Therefore, top-down methods such as electron beam lithography (EBL) and focused ion-beam (FIB) milling being surfactant and spacer free fabrication methods, are highly suitable for systematic and mechanistic study on single particles by allowing high spatial precision.

In summary, investigating plasmon-meditated catalytic reaction on a single particle level helps to simplify the observed systems to deconvolute the governing parameters that promote efficient chemical reactions. For this, it is critical to build highly tunable plasmonic nanoreactors with wide range of local-field enhancement that can readily participate in photacatalytic reactions with a wide range of field enhancement ability. In this study, we designed and fabricated single nanostructures with specified hot-spots and light absorption profiles to investigate the plasmon-driven catalytic reactions. This study on specifically engineered structures was carried out to minimize the ambiguity caused by ensemble averaging in identifying the governing parameters for the reaction rate. *In-situ* SERS allowed us systematically tracking the reactions in real-time that can be directly correlated to the hot-carrier generation. Understanding the catalytic behaviors on such highly controlled platform could provide valuable insights towards optimizing the parameters in building efficient plasmonic nanoreactors.

3.4.1 Engineering nanonatennae optical properties

To assess the influence of hot-spots in photocatalytic reactions, gold nanoantennae with gap sizes of 5, 10, 20, and 30 nm were fabricated with electron-beam lithography followed by electron-beam Au deposition. The size of the Au nanoantennae (Figure 3.16) were tuned such that the scattering and absorption profiles of the dimer reactors are similar at 633 nm, which is the excitation laser wavelength for SERS. The well documented dehalogenation reaction of 4-iodothiophenol (4-ITP) was employed as a model chemical reaction to trace the hot-electron generation over-time in each Au dimer (i.e., gap size of 5, 10, 20 and 30 nm) [128–131]. The SERS signal of 4-ITP was tracked under focused 633 nm continuous wave (CW) laser illumination. Figure 3.15 describes the photocatalytic dehalogenation reaction of 4-ITP together with the basic geometry of our nanoantenna. 4-ITP molecules are transformed into thiophenol (TP) and 4,4'-biphenyldithiol (4,4'BPDT) upon laser irradiation. As it can be observed in the heatmap in Figure 3.15, the bands corresponding to the phenyl-ring ($\sim$ 1560 rel./cm^{-1}, indicated in red) and C-I bond ($\sim$ 1058 rel./cm^{-1}, indicated in blue) from 4-ITP decrease over-time. On the other hand, the Raman bands assigned to the product molecules, TP ($\sim$ 1580 rel./cm^{-1}, indicated in green) and 4,4'-BPDT ($\sim$ 1590 rel./cm^{-1}, indicated in yellow) increase in time. To extract the kinetics of 4-ITP dehalogenation reaction from the time-dependent SERS spectra, we

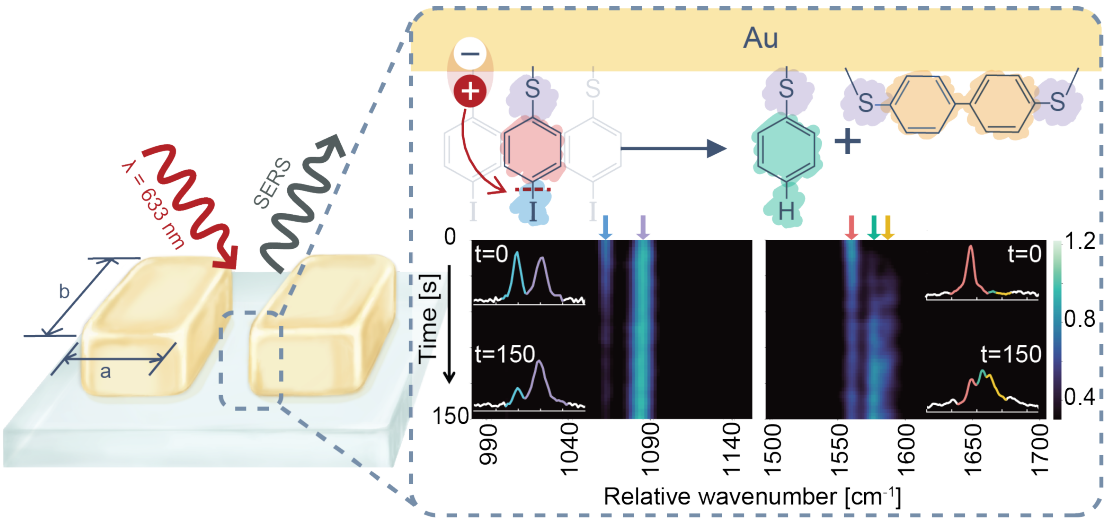

Figure 3.15: Schematic illustration of an *in-situ* SERS study on the interfacial transmission of hot-electrons using the photocatalytic dehalogenation of 4-ITP. 4-ITP can be degraded into thiophenol (TP) and 4,4'-biphenyldithiol (4,4'BPDT) upon interactions with hot-electrons. The heat-map represents the Raman intensities of 4-ITP, TP, and 4,4'BPDT overtime. Dehalogenation process can be traced from decreasing Raman peaks of C-I bond (denoted in blue) and phenly-ring (denoted in red) and increasing peaks of TP (denoted in green) and 4,4'-BPDT (denoted in yellow). The C-S peak (denoted in purple) is chosen as the reference.

tracked the intensity ratio of the C-I and C-S band. By taking the ratio of these two SERS bands (i.e., the C-I and C-S) within each time step, we overcame the difficulties caused by fluctuating intensities during the time-resolved measurement that arise from single-particle level SERS. This self-normalizing process also helps to eliminated contributions from other experimental parameters which could impede an accurate determination of the dehalogenation kinetics such as varying initial SERS intensities from dimer to dimer and possible minor drifts in the focus position during extended measurement.

For comparable and reproducible SERS analysis, the dimers were designed to have varying local-field enhancement at the hot-spots located at the gaps while maintaining a similar level of geometric anisotropy and transversal resonant profile. Each Au dimer was identified and selected with SEM imaging prior to the measurement. The dimensions of the four dimers and the electric-field enhancement at the hot-spots are shown in Figure 3.16. Upon illumination with 633 nm laser, the x-polarized field profile excites the transversal resonance mode, namely at the gap, and y-polarized profile excites longitudinal resonance mode in each dimer. As we learned from the electromagnetic simulations, the near-field enhancement at the gap (transversal) mode is $3 \sim 6$-fold greater than that of the longitudinal mode under 633 nm laser illumination. This indicates mainly that the transversal mode

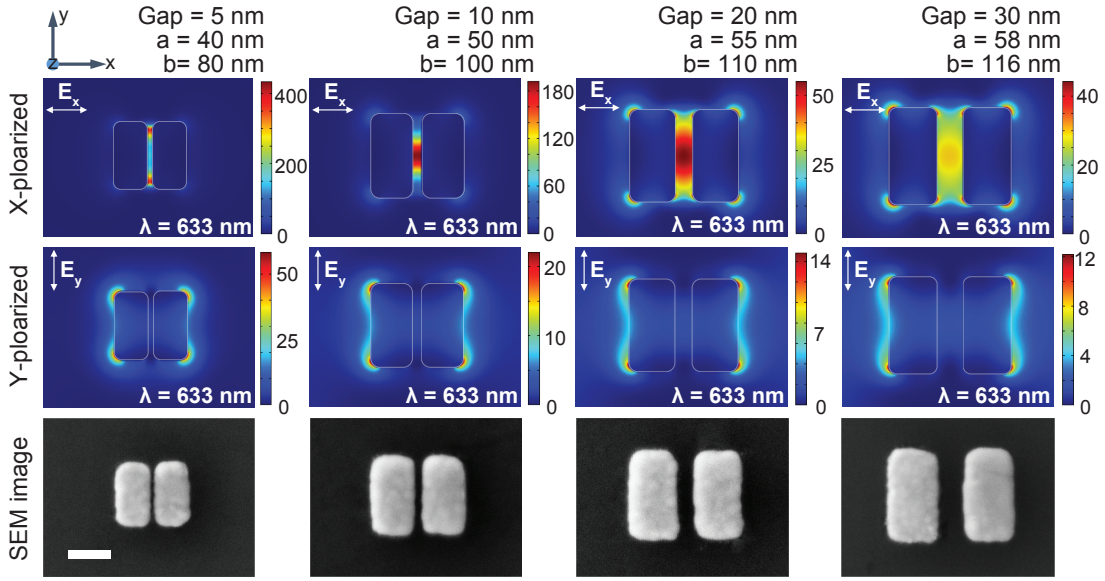

Figure 3.16: Field enhancement ($|\mathbf{E}|^2/E_0^2$) maps under x- and y- polarized light on each dimer, data shown at cross section at antenna mid-height (upper pannels), z = 20 nm; representative SEM image of each dimer (lower pannel), scale bar: 50 nm. The widths and lengths of the rods are denoted as a and b.

at the gap area is excited by the 633 nm laser. This can also be further supported by the calculated and measured darkfield spectra from Figure 3.17a. As expected, the local-field enhancement at the dimer with the smallest gap size, 5 nm, was the highest among all the dimers.

To investigate the role of the varying electromagnetic field enhancement on dehalogenation, *in-situ* SERS study was carried out under 633 nm excitation. As a result, we observed that the smaller gaps lead to the higher conversion rate of ITP to TP and 4,4'-BPDT due to the higher hot-carrier generation rate. Tightly confined electromagnetic fields have a significant impact over the generation of energetic hot-carriers through increased photon absorption inside the metal and contribute to the excitation of intraband hot carriers with their strong field gradients. In our nanostructures, the plasmon mode contributing most to the 4-ITP dehalogenation reaction is the gap (transversal) mode, which has a $4 \sim 8$ times higher maximum field enhancement than the longitudinal mode (Figure 3.16). The sizes of the dimers were engineered so that the transversal mode resonates at 633 nm since increasing the gap size on the fixed-sized dimers would cause blue-shift to the transversal mode due to decreasing interparticle coupling strength amongst the rods (Figure 3.17b). Since it has been reported that the anisotropy of the plasmonic reactors influences the reaction [116], the aspect-ratios of each rod were fixed for alll the dimers. Notably, the

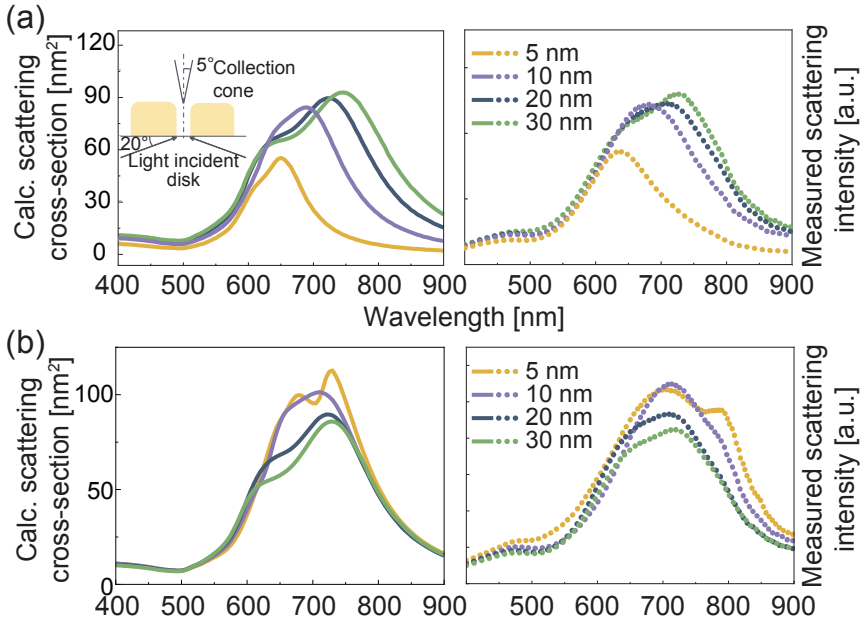

Figure 3.17: (a) Calculated darkfield cross-sections (left) compared with measured darkfield scattering intensity (right) of the dimers. The rod dimers were designed to have comparable scattering cross-sections at 633 nm. Numerical model was aimed to mimic the darkfield measurement setup under transmission mode. The representative schematics of the model is illustrated in the left panel. (b) Calculated darkfield cross-sections (left) compared with measured darkfield scattering intensity (right) of the dimers with fixed rod size and varying gap size.

excitation wavelength (633 nm) excites the transverse plasmon mode (x-polarized in Figure 3.16) in all gaps, while the longitudinal plasmon mode (y-polarized in Figure 3.16) increases in intensity and red shifts for the longer Au rods. Figure 3.17 demonstrates that the calculated and measured scattering profiles are in great agreement. Figure 3.18a presents the time-dependent cleavage of the C-I bond, monitored through *in-situ* SERS. By precisely engineering nano-reactors with accurate gaps we were able to eliminate nonlocal rate enhancement mechanisms such as heat and track locally the plasmon-driven reaction rate on single Au dimers [132]. Due to the homogeneity of our nano-reactors, corroborated with the fixed 4-ITP concentration (due to the formation of a self-assembled monolayer), we modeled the reaction kinetic rate with a first order reaction rate: $Rate_{\frac{(C-I)}{(C-S)}} = e^{-\kappa t} + constant$ [129]. That is, the reaction rate depends only on the hot-electron concentration, and not also on the molecular concentration. Similar studies on plasmon-induced dehalogenation were performed on aggregated colloidal nanoparticles that yield hot-spots with heterogeneous gap sizes. In such system, the use of more complicated reaction rates models such as fractal kinetic model is required [63, 129]. This leads to a more complicated interpretation of the

experimental results and an unclear distinction of local and nonlocal rate enhancement mechanisms. Indeed, the observed dehalogenation showed great agreement with the first-order reaction trend. The reaction rate, κ, under 633 nm laser with 0.5×10^6 mW/cm^2 fluence illumination was observed to be decreasing as the interparticle size increased over all. Average measured κ values were 0.09, 0.07, 0.03, and 0.02 s^{-1} for 5, 10, 20, and 30 nm-gap dimers respectively.

3.4.2 Hot-electron meditated dehalogenation

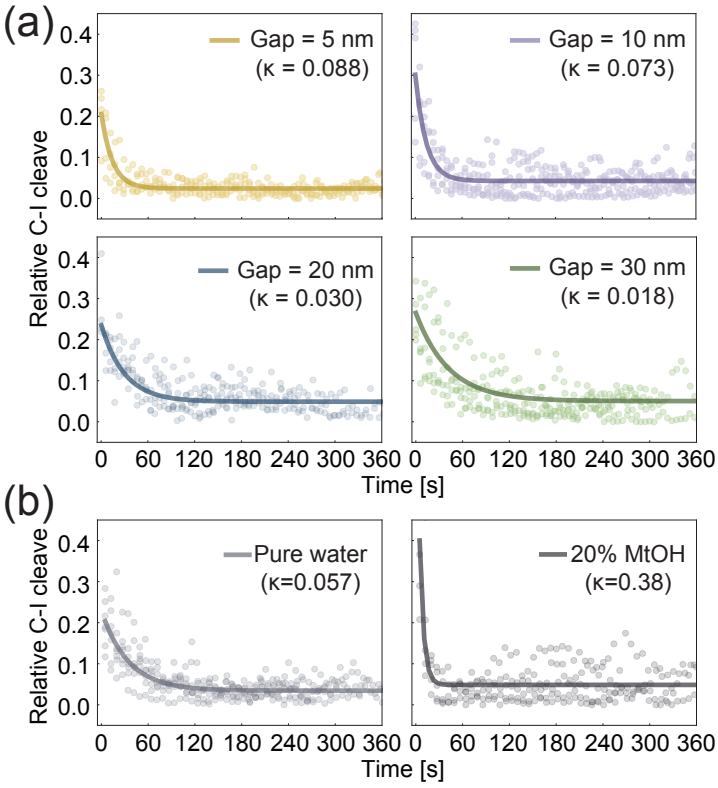

Figure 3.18: (a) SERS intensity integrated of C-I/C-S bands plotted over time. The result from each gap size was averaged over at least 4 individual measurements.(b) SERS intensity of C-I/C-S bands with (right) and without (left) hole-scavenger, methanol, over time. The excitation laser in all the measurements was 633 nm with 0.5×10^6 mW/cm^2 intensity.

To further confirm that the dehalogenation of 4-ITP is a first order reaction which depends on the concentration of hot-electrons we compared the dehalogenation rate with and without hole-scavenging agent, methanol, on identical rod dimers. As shown in Figure 3.18b, with 20% v/v added methanol, the reaction rate was improved by $\sim$ 6 times.

Since the nanoantennae subjected in the study was identical, it is safe to assume that the thermal contribution in both cases were identical under the same laser irradiation. Hence, the improvement in the reaction can be attributed to efficient hot-hole removal from the system preventing carrier recombination. This result is consistent with previous findings that the reaction is predominantly governed by hot-electrons when the density of the nanoantennae is low [132]. In this study, the authors demonstrated the electronic excitation of the adsorbates plays a main role in plasmon-meditated reactions when there are less than 10 plasmonic nano-reactors within $\sim 0.15\ \mu m^2$. [132].

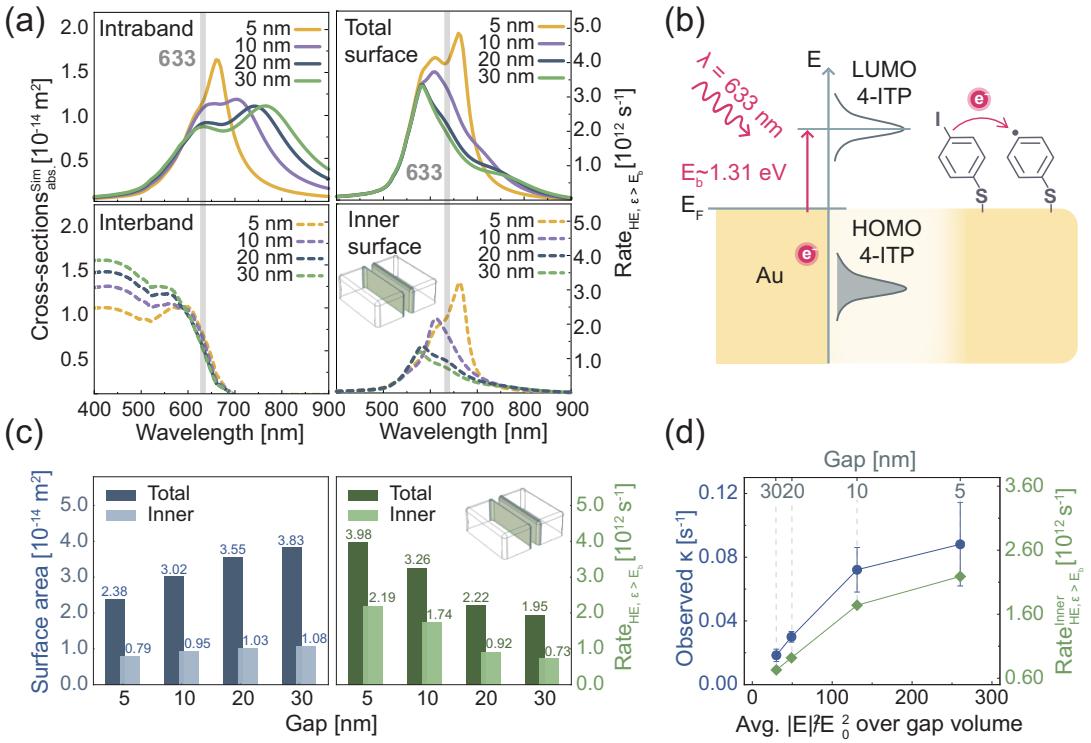

Figure 3.19: (a) Shows calculated intraband absorption (upper-left) and interband absorption (lower-left); and high energy (intraband) hot-electron excitation rate across the entire surface of the dimers (uppper-right) and inner surface at the gaps (lower-right). The schematic representative of the inner surface area is denoted as the shaded area on the right panel and the excitation wavelength 633 nm was highlighted on each panel. (b) Simplified schematics of plasmon-meditated electron transfer. The minimum hot-electron energy required to cleave C-I bond, $E_b \sim 1.31$ eV, is determined from density functional theory calculations. (c) Left panel shows the physical areas of the Au dimers: dark blue corresponds to the total surface areas and light blue corresponds to reactive areas located at the inner surfaces of the gap. Right panel represents calculated hot-electron generation rate, Rate_{HE}, of the dimers for carriers with energies in excess of 1.31 eV above the Fermi energy of Au across the entire surface and inner surfaces.(d) Shows field enhancement dependent observed reaction rate, κ, and calculated hot-electron generation rate, Rate_{HE}, of the dimers for carriers with energies in excess of 1.31 eV above the Fermi energy of Au. The y-scales are determined to reflect the true scale as compared the values at 30-nm-gap dimers. The independent variable was obtained by averaging the field enhancement over the gap volume.

The contributions of plasmon-mediated excited electrons were investigated with theoretical calculations. The roles of high and low energy electrons generated within the entire volume and surface of dimers were investigated. Upon excitation of the plasmonic modes, carriers are excited in the metal, and we can differentiate between carriers being excited

to low and high kinetic energies, the latter of which being the most interesting for photocatalysis performance, as these high energies allow them to traverse the energy barrier separating the metal and the molecules. These can be excited through intraband absorption, when allowed by processes such as surface scattering, or through interband absorption. Although high-energy hot carriers can be excited through intraband processes, most of the intraband absorption produces excited carriers close to the Fermi energy of the metal, which we refer to as Drude carriers. The classical absorption cross section associated to such process is shown in the left panel in 3.19a, while the excitation spectra of high-energy intraband carriers can be found from the right panel in 3.19a. The power absorbed through interband processes, whose cross-section for these systems is shown in upper-left panel of Figure 3.19a, produces low-energy electrons and high-energy holes. These transitions are a bulk-like process of absorption, whose cross-sections are shown in the lower left panel in Figure 3.19a. Our simulations show that, among the two mechanisms for excitation of high-energy carriers, the surface-assisted excitation of intraband hot-electrons reproduces the experimental trend of reaction rate across the dimers, as shown in Figure 3.19c and d, whereas the inter-band absorption cross-sections remain constant at 633 nm for all systems. Thus, together with the experimental evidence gathered using hole harvesters (Figure 3.18c), this supports the hypothesis that the injection of hot intraband electrons drives the reaction. Furthermore, since plasmonic hot-electrons are generated mainly at the interface between the metal and the molecule, whereas Drude electrons are generated across the entire volume dimers; we can conclude that the dehalogenation reaction of 4-ITP is predominantly mediated by the hot-electrons generated at the surfaces, with the inner dimer surfaces at the gap having a particularly relevant role (right panel in 3.19a).

To further understand the mechanism, the reaction was investigated under various power densities on dimer and single rod nanoantennae. As a result, no significant catalytic reaction was observed when the excitation power was lower than 0.4×10^6 mW/cm^2 on dimers; furthermore, when single rods were irradiated with the same power that results in the reaction on the dimers (0.5×10^6 mW/cm^2), there was no reaction observed either (see Figure S5 and S6). From this, we can conclude that there is a light intensity threshold where the 4-ITP molecules can be observed through SERS but is not sufficient to trigger the catalytic reaction, and the local-field intensity governs the number of the high-energy electrons generated. As it is depicted in Figure 3.15, the dehalogenated 4-ITP molecules will become TP and 4,4'BPDT. This is a multi-electron process, and the reaction will only start to be promoted when the number of the excited electrons is sufficient. It is to be noted that there is a kinetic energy requirement for the hot-electrons to overcome the energy difference between the Fermi level of the metal and the lowest unoccupied molecular orbital (LUMO) of the adsorbates [132–134]. The minimum energy required for

such dehalogenation, denoted as E_b in Figure 3.19b, was estimated via density functional theory calculation. Figure 3.19b shows simplified schematic of energy bands in the metal and the molecule: upon illumination, the generated hot-electrons that can overcome the minimum energy barrier, $E_b \sim 1.31$ eV, will excite the adsorbed molecules at the gold surface and cleave the C-I bond. Based on the calculated E_b value, we can safely assume that our excitation laser, 633 nm CW laser, can provide sufficient kinetic energy for the hot-electron to overcome E_b. Subsequently, we have calculated the generation rates of hot carriers with energies above E_b considering two regions: the whole surface of the dimer exposed to the molecule, and only the surfaces facing the gap (highlighted areas in the right panel of Figure 3.19c) were calculated. The rate of hot carrier excitation was computed using the following equation, derived from a quantum model of the plasmonic carrier dynamics, taking as input from the classical simulations the component of the electric field normal to the Au surface, and inside the antenna, $E_{normal}(\mathbf{r}, \lambda)$:

$$Rate_{HE}(\mathbf{r}, \omega) = \frac{2}{\pi^2} \frac{e^2 E_F^2}{\hbar} \frac{\hbar\omega - E_b}{(\hbar\omega)^4} |E_{normal}(\mathbf{r}, \omega)|^2 ds$$

where E_F is the Fermi energy of Au, $\hbar\omega$ is the incoming photon's energy, and ΔE_b is a threshold electronic energy above which we consider that the carrier can surpass the potential energy separating the metal and the 4-ITP molecule [112, 113]. The right panel of Figure 3.19c expands the theoretically calculated generation of hot carriers, and those arising at the total surface and the inner walls are shown separately. The excitation rates integrated along the reactivesurface areas across the entire surface and at the inner walls are shown in the right panel of Figure 3.19c separately. It can be observed that the reactive surface area at the gaps only constitutes $\sim 24\%$ at most, yet $37 \sim 55\%$ of the total hot-electrons generated over the energy barrier are from the gaps. This demonstrates the dominant role of the inner walls in the overall catalytic performances of the dimers.

To intuitively show the influence of hot-spot strength to the reaction, observed κ values and calculated hot-electron generation rates at the inner surfaces under 633 nm laser illumination are plotted with respect to the corresponding average field enhancement factor at the gap of each dimer in Figure 3.19d. Evidently, the trend of dehalogenation is in great agreement with calculated hot-electron generation rate at the inner faces of the dimers. The overall dehalogenation rate was observed to be faster on the dimers with higher local-field enhancement. As it is shown in the equation above, we can see that when all the dimers are excited by the same laser, the dehalogenation rate should only dependent on the local electric field and the surface area of the nanoantennae. Interestingly, the dehalogenation rate of the 10-nm-gap dimer was 4 times faster than that of 30-nm-gap dimers with only 1.7 times enhancement in the local-field. Further reduction in gap size did not improve the

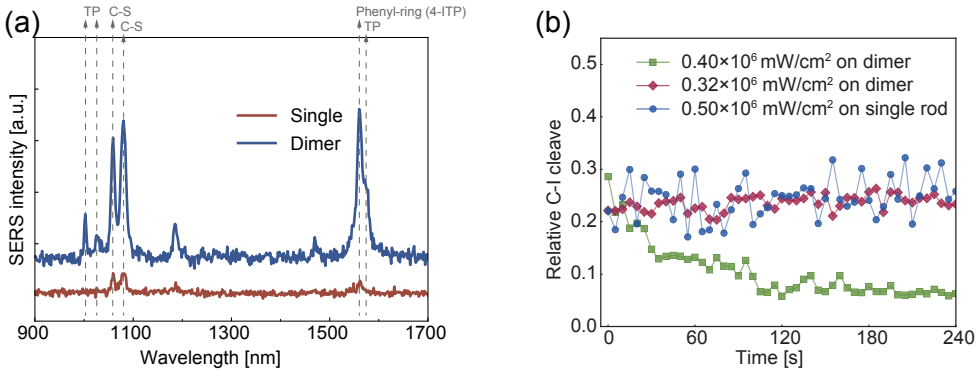

Figure 3.20: (a) SERS spectra measured on single rod (55 nm x 110 nm) and dimer (55 nm x 110 nm, gap 10 nm). (b)SERS intensity of C-I/C-S bands overtime on dimers and single rods under various excitation power.

reaction rate significantly even though the local-field was ~ 2 times stronger. This can be attributed to the competing relationship between decreasing surface areas and increasing field intensity with the decreasing antennae sizes.

3.5 Conclusions

In this section, the roles of the EM field and plasmon meditated hot-electrons to photocatalytic reactions were investigated. The AgNWs from 3.3 is fabricated with templateless capillary-assisted particle assembly method. The Au dimers from 3.4 is fabricated following the steps shown in Figure A.1(See Appendix). To guarantee accuracy and reporducibilty the overlay alignment method by precisely placing the left bar next to the already fabricated right bar. The precision of the alignment was ensured using the 4-point marker system.

In Section 3.3, it was showed for the first time the impact of specific ion effects, particularly Ca^{2+} and Mg^{2+}, in the plasmon-assisted dehalogenation of Br-Ade to Ade. More specifically, we show that divalent Ca^{2+} and Mg^{2+} ions can bridge the adsorption of negatively charged Br-Ade to the negatively charged AgNW surface, and thus facilitate the direct charge transfer from the plasmon resonance modes of Ag nanostructure to the acceptor orbitals of Br-Ade, resulting in the cleavage of the Adenine-Br bond. Based on the DFS measurements, we suggest that CID is the primary electron transfer mechanism driving the dehalogenation of Br-Ade, in the presence of Ca^{2+} ions, due to the stronger adsorption of Br-Ade to the Ag surface, which leads to an overlap of the metal states and molecular energy orbitals, as shown by the calculated density of states (DOS). Contrarily, in the lack of Ca^{2+} ions, Landau damping is probably the main electron transfer mechan-

ism. These results show how complex plasmonic interfaces can be, and that the surface dynamics of molecules and even of water molecules cannot be ignored.

Section 3.4 evaluated experimentally and theoretically the role of of the inperparticle hot-spots in plasmon meditated photocatalytic reactions in terms of electromagnetic field strength and surface area on highly controlled platforms. To eliminate the ensemble averaging, *in-situ* single-reactor SERS was employed on top-down fabricated gold nanorod dimers with varying interparticle distances. Comprehensive and systematic comparisons across the dimers were ensured by designing and fabricating the dimers that have similar absorption profiles and morphological anisotropy. Photocatalytic dehalogenation of 4-iodothiophenol (4-ITP) was employed to trace the hot-electron generation. From the highly controlled experiments, we successfully confirmed that the reaction follows first-order kinetics. We have identified the overall reaction across the dimers to be predominantly governed by the hot-electrons generated at the gaps. The reaction rate increased as the local-field intensity increased with decreasing interparticle distances. Unlike the signal intensity studies of the SERS platforms, the reaction rate improvement did not show quadratic increase with the field intensity at the gap. Decreasing the gap size by 10 nm has improved the reaction by more than 2-folds, but further decrease in the gap distance did not improve the reaction rate significantly. This study has demonstrated that changing only the gap-size will improve the reaction rate significantly wihtout changing any other reaction conditions.

In conclusion, a comprehensive understanding of plasmonic chemistry can be achieved by considering connected physical-chemistry aspects of the surface-molecule interaction, such as Hofmeister effects. By doing so, more efficient strategies can be designed for harnessing the full potential of plasmon-assisted chemical reactions at the nanoscale. The identified surface-specific contributions to the reaction offer opportunities to engineer reaction-specific hot-spots, enabling site-specific multiplexing capabilities for the plasmonic nanoreactors. These findings provide valuable insights for engineering photocatalytic platforms that ensure the field intensity while guaranteeing sufficient reactive surface and volume.

Chapter 4

Exploiting surface phonon polaritons

4.1 Phonon polariton dispersion in free-Standing SiC thin films

Published in: "Near-Field Retrieval of the Surface Phonon Polariton Dispersion in Free-Standing Silicon Carbide Thin Films." ACS Photinics (2022)
Mancini, Andrea, Lin Nan, Fedja J. Wendisch, Rodrigo Berté, Haoran Ren, Emiliano Cortés, and Stefan A. Maier.

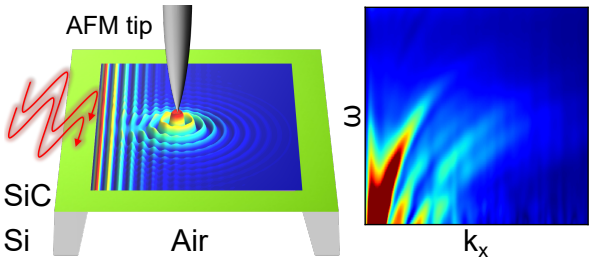

In the previous chapter, it was shown that plasmonic nanostructures can be used to enhance light-matter interactions and modulate photocatalytic activities in the visible region, by achieving sub-diffraction field enhancement. The present chapter aims to extend the wavelength of interest to the mid-IR to IR range, and explore sub-diffraction field modulation in this region. The material of interest in this chapter will be explored in depth in this section below along with the main characterization techniques scattering-type scanning near-field optical microscopy (sSNOM) and Fourier transform infrared (FTIR) spectrocopy.

This section focuses on discussing the presence of surface phonon polaritons (SPhPs) in SiC thin films and their dispersion retrieval through near-field measurements. As outlined in Chapter 2, an intriguing characteristic of phonon polaritons is the potential for anisotropic propagation due to the complex crystal structure of polar dielectrics. This is related to the simultaneous presence, at a fixed frequency, of both positive and negative terms in the dielectric tensor [135–140]. Thin films composed of layered van der Waals (vdW)

materials have garnered considerable attention due to their ability to support highly anisotropic hyperbolic and elliptical phonon polaritons, along with extreme subdiffractional confinement [140–147].

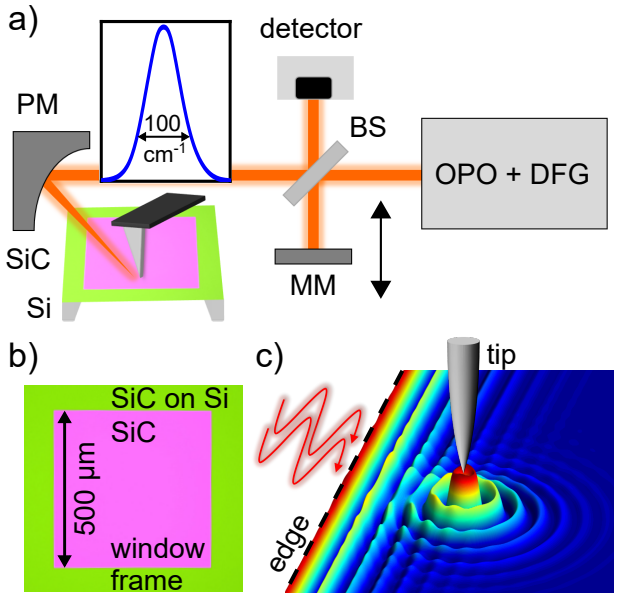

Figure 4.1: (a) Sketch of the nano-FTIR setup used in the experiments (BS, beam splitter; MM, moving mirror; PM, parabolic mirror). The light source is an OPO laser with a DFG module, resulting in a MIR pulse with a bandwidth of 100 cm^{-1}. Light is focused on the tip of an AFM by a parabolic mirror, and the back-scattered light is redirected towards a MCT detector by passing through a beam-splitter. (b) Optical image of a SiC membrane window with a thickness of 200 nm. (c) Artistic representation of SPhPs launched by both the tip and the window edge.

In our study, we have utilized scattering-type scanning near-field optical microscopy (sSNOM) to retrieve the dispersion of surface phonon polaritons (SPhPs) in free-standing membranes of SiC (polytype 3C) with thicknesses of 100 nm and 200 nm. sSNOM allows for direct polariton measurements by providing the missing momentum for excitation in unpatterned samples, while also providing subwavelength spatial resolution [141, 148]. Through position-dependent nano-FTIR spectra, we were able to reconstruct the dispersion relation at multiple frequencies in a single experimental run [148, 149]. Figure 4.5(a) displays a sketch of the experimental setup used in our study. The SiC membranes are supported by a silicon frame with a 500 µm × 500 µm square window in the center and a thickness of $\sim$ 400 µm. Figure 4.5(b) shows an optical microscope image of the top of a 200 nm membrane. During scanning on the membrane, SPhPs are launched from both the tip and the edge, as demonstrated in Figure 4.5(c), resulting in complex interference patterns that we analyze in detail in the following sections.

4.1.1 SPhPs dispersion in thin films

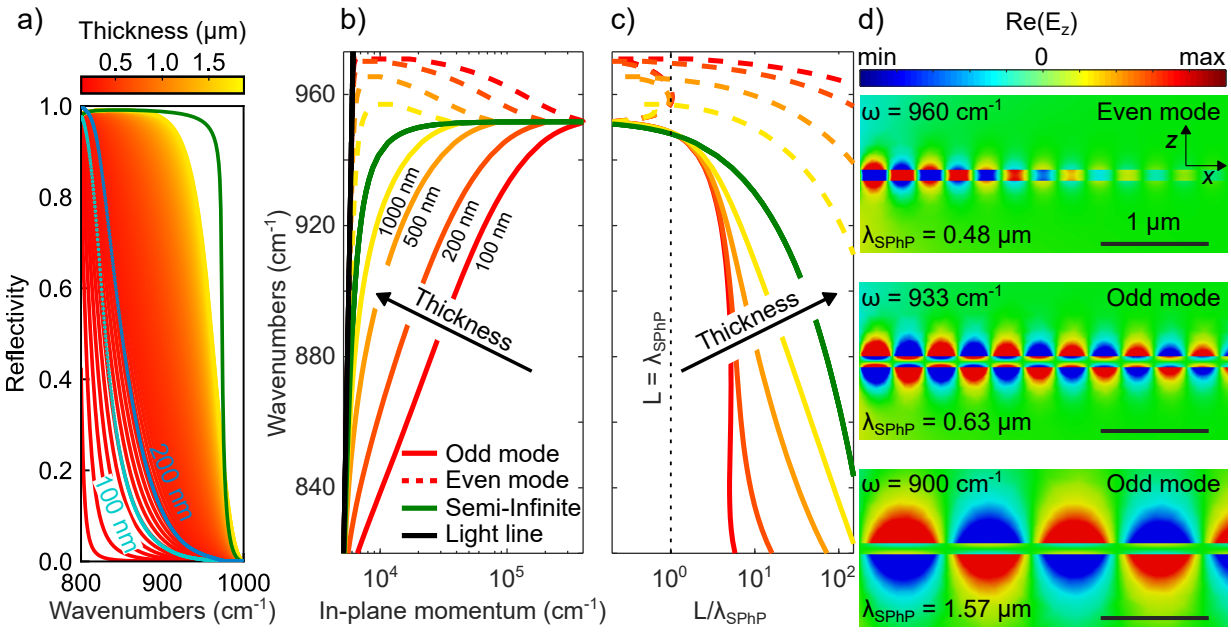

Figure 4.2: (a) Calculated normal incidence reflectivity for a free-standing layer of SiC of variable thickness in air. Markers are experimentally measured quasi-normal incidence reflectivity spectra for 100 nm (light blue) and 200 nm (blue) SiC membranes. The green line is the reflectivity for a semi-infinite SiC surface. (b) Theoretical SPhP dispersion in free-standing SiC films of various thicknesses. The single SPhP dispersion on a semi-infinite surface (green line) splits in films of finite thickness in a high energy mode (even mode) and a lower energy mode (odd mode). The splitting increases as the thickness decreases. For a range of frequencies above the green line asymptote, the even mode has two solutions. (c) Calculated ratio between the propagation length and the SPhP wavelength for the same thicknesses in (b). (d) Simulated field profile at three different frequencies for a 100 nm membrane. The even and odd modes are named with respect to the symmetry of the electric field in the z direction normal to the SiC surface.

To confirm the optical properties of the SiC membranes we first investigate their far-field response by FTIR spectroscopy. In Figure 4.2 (a) we show the analytically calculated normal-incidence reflectivity of free-standing SiC thin films of various thicknesses T in air, obtained from the Fresnel coefficients for a three-layer system. [150]. For decreasing T the reflectivity stays high around the TO phonon (at 797 cm^{-1}), while it substantially drops close to the LO phonon (at 973 cm^{-1}). The green line indicates the response of a semi-infinite SiC surface, showing high reflectivity in the whole RS band. Markers in Figure 4.2(a) show the measured reflectivities for the 100 nm (light blue) and 200 nm (blue) membranes. We used for the calculations of the reflectivity the same SiC dielectric function

employed in the previous chapter, which follows eq. 2.4 with $\varepsilon_\infty = 6.6$, $\omega_{TO} = 797\,\mathrm{cm}^{-1}$, $\omega_{LO} = 973\,\mathrm{cm}^{-1}$ and $\gamma = 1.4\,\mathrm{cm}^{-1}$. The close match between the calculated and experimental reflectivity confirms that the optical properties of the SiC membranes can be modeled from literature values of the dielectric function.

In plasmonic thin films the surface plasmon polariton (SPP) dispersion splits into a lower and a higher energy mode [18], resulting from hybridization of the separate SPPs existing at the top and bottom interfaces. The splitting becomes appreciable when the film thickness T is reduced to values comparable to the material skin depth, on the order of few tens of nanometers in metals [151, 152]. In SPhPs thin films the skin depth is much larger, with clear mode splitting visible already for $T = 1\,\mu\mathrm{m}$ as shown in Figure 4.2(b). The dispersion of the two modes for a film of thickness T in a homogeneous medium with dielectric constant ε_2 are given by the following implicit relations [18, 151]:

$$\begin{aligned} \varepsilon_1 k_2 + \varepsilon_2 k_1 \tanh\left(-i\frac{k_1 T}{2}\right) = 0 \\ \varepsilon_1 k_2 + \varepsilon_2 k_1 \coth\left(-i\frac{k_1 T}{2}\right) = 0 \end{aligned} \tag{4.1}$$

where $\varepsilon_1 = \varepsilon(\omega)$ is the dielectric function of the "metallic" layer and k_i are the wavevectors in the z direction (as the top and bottom materials are the same $k_2 = k_3$). In our case $\varepsilon(\omega)$ is the SiC dielectric function. The in-plane SPhP wavevector β is related to the out of plane wavevectors k_i by:

$$k_i^2 = \beta^2 - k_0^2 \varepsilon_i \tag{4.2}$$

where where k_0 is the free-space wavevector. By substituting eq. 4.2 in eq. 4.1 two equation for the in-plane wavevectors $\beta = k_{ev}$ and $\beta = k_{odd}$ of the two modes can be written:

$$\sqrt{\frac{k_{ev}^2(\omega,T) - k_0^2\varepsilon_2}{k_{ev}^2(\omega,T) - k_0^2\varepsilon(\omega)}} = \frac{\varepsilon_2}{\varepsilon(\omega)} \times \tanh\left(\frac{T}{2}\sqrt{k_{ev}^2(\omega,T) - k_0^2\varepsilon(\omega)}\right) \tag{4.3}$$

$$\sqrt{\frac{k_{od}^2(\omega,T) - k_0^2\varepsilon_2}{k_{od}^2(\omega,T) - k_0^2\varepsilon(\omega)}} = \frac{\varepsilon_2}{\varepsilon(\omega)} \times \coth\left(\frac{T}{2}\sqrt{k_{od}^2(\omega,T) - k_0^2\varepsilon(\omega)}\right) \tag{4.4}$$

Equation 4.3 describes the dispersion of the higher energy even mode k_{ev}, for which the field component perpendicular to the film surface E_z is symmetric (even mode), while equation 4.4 describes the lower energy mode k_{od} for which E_z is antisymmetric (odd mode).

In Figure 4.2(b) the numerical solutions of equations 4.3 and 4.4 for $\varepsilon_2 = 1$ are reported for selected values of T, along with the dispersion for a semi-infinite SiC slab in air (green line) and the vacuum light line $\omega = ck_0$ (black line). The energy splitting between the odd (solid lines) and even (dashed lines) modes increases as T is reduced, as shown in Figure 4.2(b). From Figure 4.2(b) one can see that for decreasing T the wavelength shrinking λ_0/λ_{SphP} for the odd mode is increased as the in-plane momentum increases at any given frequency. It should be noted that the even mode branch has two solutions above the frequency where $\varepsilon(\omega) = -1$ (corresponding to the asymptote of the semi-infinite slab dispersion), one close to the light line with practically no confinement, and another one at higher k. In Figure 4.2(c) we report the calculated ratio between the SPhP propagation length L and its wavelength λ_{SPhP}. While not showing appreciable field confinement, the low-k even mode solution features very long propagation lengths, efficiently transporting thermal energy and enabling the enhanced in-plane thermal conductivity reported in thin films of polar dielectrics [153–155]. For a mode to be detectable in a polaritonic interferometry experiment, it has to travel at least one wavelength before decaying. As a consequence, the high-k vector even mode solution cannot be detected in our experiments as the ratio L/λ_{SPhP} is below unity at all frequencies (see vertical dashed line in Figure 4.2(c)). In Figure 4.2(d) we show a snapshot of the simulated $\mathrm{Re}(E_z)$ field profiles at three selected frequencies for a $T = 100\,\mathrm{nm}$ membrane. In the top panel the high-k solution of the even mode (symmetric in E_z) can be identified due to the strong wavelength confinement and field symmetry. As it can be seen from Figure 4.2(b), this solution is characterized by negative group velocity ($d\omega/dk < 0$). This is a consequence of the field being concentrated in the "metallic" region where the Poynting vector parallel to the surface points in the negative direction (to the left in Figure 4.2(d)) [156]. The low propagation length of this mode is associated with increased losses in the SiC film due to the field being concentrated inside the material, which has been leveraged for enhanced second harmonic generation [157]. This weakly propagating mode is usually named epsilon near zero (ENZ) mode [158] as for sufficiently small T the even mode dispersion is pushed towards the $\varepsilon(\omega) = 0$ line. In the two bottom panels of Figure 4.2(d) the odd mode solution (antisymmetric in E_z) is shown for two different frequencies. From Figures 4.2(b, c) and the simulated field profiles, one can see that there is a general trade-off between propagation length and wavelength shrinking for the SPhPs. The $\mathrm{Re}(E_z)$ symmetry determines the energy of the two modes: the charges at fixed x inside the SiC layer at the top/bottom interfaces have the same sign in the even mode, raising the energy due to repulsion, while they have opposite sign for the odd mode, lowering the energy due to attraction.

4.1.2 Retrieval of the SPhPs dispersion

To experimentally reconstruct the SPhP dispersion in the membranes, we use the nano-FTIR sSNOM technique in a commercial setup (neaspec), where a broadband source is coupled to an AFM in an asymmetric interferometer configuration (see sketch in Figure 4.5(a), allowing the measurements of near-field spectra with subwavelength spatial resolution [148, 149, 159]. We use illumination from an optical parametric oscillator (OPO) laser (Stuttgart Instruments), feeding a difference frequency generation (DFG) module, where the MIR output is realized by DFG between the signal and idler outputs. The bandwidth of the MIR laser pulse is approximately $100\,\mathrm{cm}^{-1}$, resulting in high signal-to-noise measurements thanks to the high power per frequency [160]. This is essential as the low membranes reflectivity close to the LO phonon leads to a very weak signal [161].

In our measurements we use the edge of the SiC window to launch and reflect SPhPs, but equivalent experiments can also be performed by etching a slit in the membrane [162]. SPhPs are in principle also launched outside of the window on the frame, however the presence of the high refractive index Si substrate redshifts the odd mode and dramatically reduces the SPhPs excitation efficiency [162]. It is well known that the measured polariton fringes periodicity is in general different from the wavelength of the polariton itself [152, 163, 164]. The sSNOM signal originates from interference between propagating polaritons and directly back-scattered light (interference between different polaritons can be neglected due to their small intensity [152]), which can be written as:

$$I(x) \approx |E_{bs}|^2 + 2\sum_l |E_{bs}||E_l(x)|\cos((\phi_{bs} - \phi_l)(x)) \tag{4.5}$$

where x is the scan direction. Here E_{bs} is the field directly back-scattered from the tip, related only to the properties of the material below the tip which we consider to be position independent. $E_l(x)$ is the field of the polaritons launched by the tip, by an edge or any other scatterer in the sample that can provide the missing momentum for polariton excitation. The phase difference between the field back-scattered from the tip and the phase accumulated by the polariton $\Delta\phi_{bs,l} = (\phi_{bs} - \phi_l)(x)$ determines the positions of maximum and minimum constructive interference and the fringes periodicity Λ. The accumulated phase depends not only on the polariton propagation, but also on the phase acquired in the optical pathways for excitation and scattering of the polaritons [165, 166]. We summarize in Figure 4.3(a-d) the main pathways producing a signal in our sSNOM experiments. Black arrows indicate the optical path of the directly tip scattered light E_{bs}, while red arrows indicate the path of the polaritons E_l (and of their in-out scattering optical path). The light incident angle with respect to the surface normal direction and with the window edge are respectively indicated as θ and φ. In Figure 4.3(a) the scheme for tip-launched polaritons

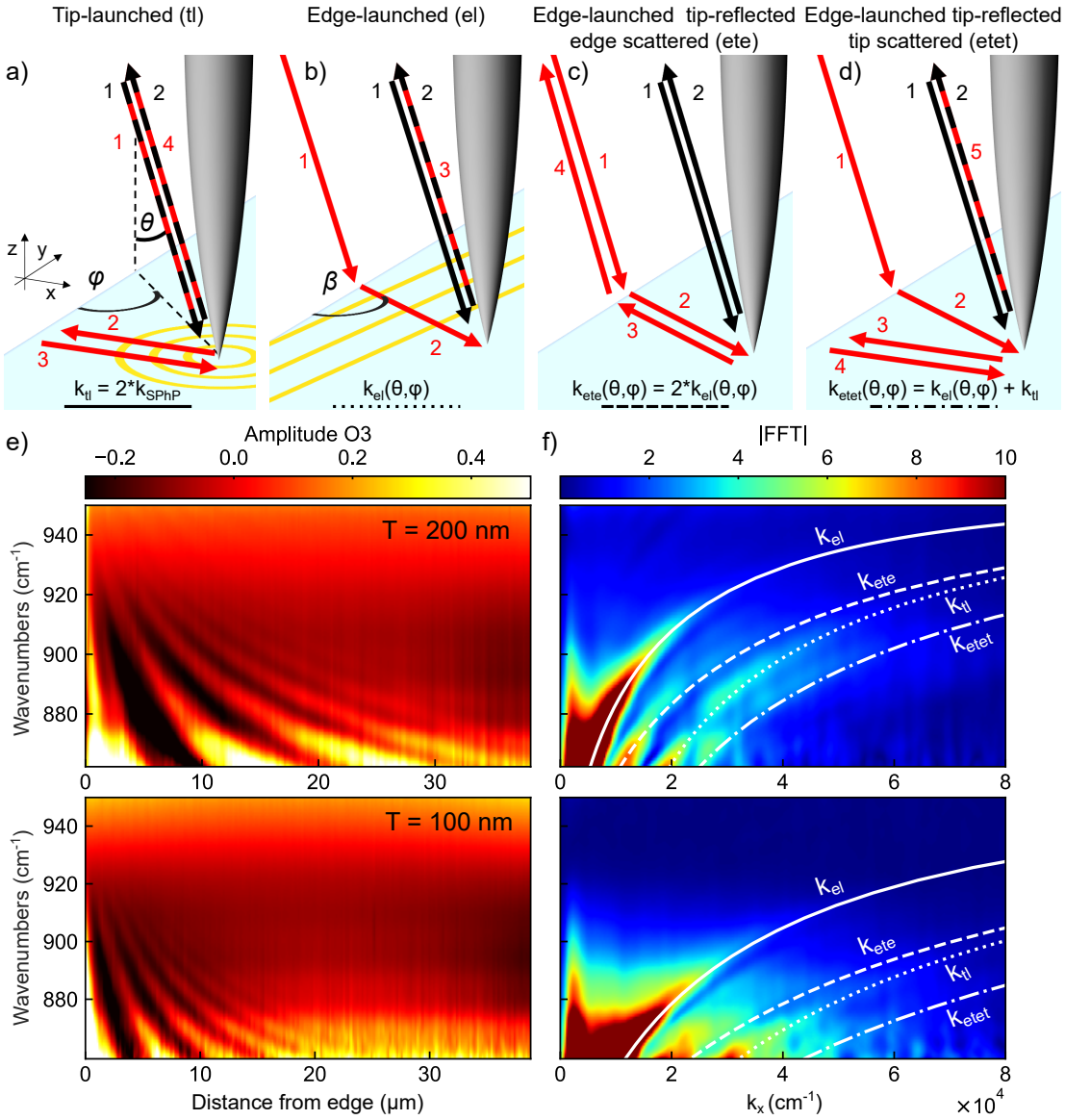

Figure 4.3: Multiple SPhP pathways (red arrows) contribute to the sSNOM signal by interfering with the tip backscattered light (black arrows). (a) SPhPs radially launched from the tip are reflected by the edge $k_{tl} = 2k_{SPhP}$. (b) SPhPs are launched from the edge and scattered by the tip and $k_{el}(\theta, \varphi)$ depends on the angles θ and φ. (c) Edge-launched SPhPs are reflected as spherical waves from the tip and back-scattered from the edge $k_{ete} = 2k_{el}$. (d) Edge launched SPhPs reflected by the tip and subsequently by the edge produce a signal at $k_{el} + k_{tl}$. (e) Baseline subtracted nano-FTIR amplitude spectra obtained by scanning from a window edge for $T = 200\,\text{nm}$ (top) and $T = 100\,\text{nm}$ (bottom) membranes. f) $|\,\text{FFT}\,|$ of the maps in (e) along the x-axis. White lines are predicted dispersions corresponding to the processes in (a-d) with $\theta = 60°$ and $\varphi = 65°$.

is shown. Here, SPhPs are radially launched by the tip and reflected at the edge, travelling twice the tip-edge distance d, accumulating double the phase delay and producing fringes at $\Lambda_{tl} = \lambda_{SPhP}/2$. This is the most dominant contribution in 2D materials as the tip near-field momentum distribution matches well with the momentum of highly confined polaritons [142]. In Figure 4.3(b) the edge-launched contribution is illustrated: polaritons are launched by the edge and propagate towards the tip, which back-scatters them in the far-field. The total phase difference accumulated for edge-launched polaritons is the sum of ϕ_{edge} accumulated by the free-space light travelling towards the edge and the ϕ_{SPhP} acquired by the SPhP when propagating from the edge to the tip, minus the free-space phase acquired by the light directly hitting the tip $\Delta\phi_{el} = \phi_{edge} + \phi_{SPhP} - \phi_{tip}$. The angle β of the polariton propagation is determined by momentum conservation $k_{0,y} = k_{SPhP,y}$ along the edge direction y [152]. The polariton accumulated phase depends in this case from (θ, φ), producing fringes with periodicity of [152, 163]:

$$\Lambda_{el}(\theta, \varphi) = \frac{\lambda_0}{-\sin(\theta)\sin(\varphi) + \sqrt{\sin^2(\theta)(\sin^2(\varphi) - 1) + n^2}} \tag{4.6}$$

where $n = \lambda_0/\lambda_{SPhP}$. While the processes described in Figure 4.3(a, b) are the most common contributions to the sSNOM signal, multiple reflections between tip and edge are also possible [149]. In Figure 4.3(c, d) we illustrate two of these possible multiple-interference pathways. Edge-launched polaritons can be re-launched by the tip towards the edge, causing back-scattering towards the detector, as shown in Figure 4.3(c). The phase accumulated by the polaritons is here doubled compared to the edge-launched case, producing fringes with periodicity $\Lambda_{ete} = \Lambda_{el}/2$. Finally, the edge-launched polaritons which are re-launched by the tip can be reflected again by the edge and scattered by the tip towards the far-field as shown in Figure 4.3(d). In this case the phase accumulation is the sum of the phase accumulated in tip-launched polaritons and edge-launched polaritons, leading to a fringe spacing of $\Lambda_{etet} = (\Lambda_{tl} + \Lambda_{el})/\Lambda_{el}\Lambda_{tl}$.

To reconstruct the SPhPs dispersion and confirm the existence of the processes described in Figures 4.3(a-d), we record spectra along a line perpendicular to one of the edges of the membrane. We align the membranes in order to have an angle φ between the k-vector of the incident light and the edge of $\varphi \approx 65°$. In Figure 4.3(e) we show the baseline subtracted spectra obtained in this way as a function of the edge-tip distance. In the top panel we report the result for $T = 200\,\text{nm}$, while in the bottom panel the one for $T = 100\,\text{nm}$. As anticipated in Figure 4.2(b) we see fringes with a higher spacing for $T = 200\,\text{nm}$ than for $T = 100\,\text{nm}$ due to the larger λ_{SPhP} (smaller in-plane momentum) in the thicker membrane. As can be seen from Figure 4.2(c), we expect the propagation length to be similarly reduced as does the polariton wavelength (the lines for $T = 100\,\text{nm}$

and $T = 200\,\text{nm}$ are almost overlapping). In order to retrieve the in-plane momentum $k_x(\omega)$ dispersion we fast fourier transform (FFT) each row in the maps of Figure 4.3(e) along the x axis. We follow the procedure outlined in previous works [148, 149] to obtain the maps of the FFT absolute value shown in Figure 4.3(f). Briefly, before performing the FFT, we mirrored the linescans along the first column, performed baseline subtraction for each row, applied a window function to have a smooth decrease at the edges and 0-padded the maps to increase resolution in k space [162].

In Figure 4.3(f) several branches appear in the dispersion maps, showing the complexity of the interference phenomena underlying the sSNOM signal in this system. From $k = 2\pi/\lambda$, we can reconstruct the expected dispersion related to the processes illustrated in Figures 4.3(a-d). Predicted dispersion relations are plotted as white curves in Figure 4.3(f) for $\theta = 60°$ and $\varphi = 65°$, showing good agreement with the experimental data (solid line for edge-launched, dashed for edge-launched-edge-scattered, dotted for tip-launched and dot-dashed for edge-launched-tip-scattered).

To confirm the accuracy of the interference model, we performed additional measurements at different rotations of the membrane. For further analysis, we isolate the edge-launched contribution by multiplying the maps of Figure 4.3(f) by a window function centered around the solid white lines. We fit the windowed maps row by row, and the extracted peak positions k_{exp} can be compared with the theoretical SPhP dispersion by inverting the relation $k_{el} = f(\theta, \phi, k_{SPhP})$

The data extracted in this way are plotted as green squares in Figure 4.4(a), in the top panel for T = 200 nm and in the bottom one for T = 100 nm. The experimental data are shown together with the analytically calculated dispersion and with the calculated imaginary part of the Fresnel reflection coefficient obtained using the transfer matrix method. The extracted experimental data closely match the theoretically predicted values for the SPhP dispersion in a thin film, demonstrating the reconstruction of the SPhP dispersion through sSNOM. These results have been further confirmed by nano-imaging at selected wavelengths, where the laser bandwidth is reduced using a monochromator. Black lines in Figure 4.4(a) indicate points with constant $n = \lambda_0/\lambda_{SphP}$, quantifying the freespace wavelength shrinking. In Figure 4.4(b,c), we report the amplitude and phase of the inverse FFT (iFFT) of the isolated edge-launched branch. In this case, we multiply the maps of Figure 4.3(f) by a Hanning window centered around k_{el} to obtain a smooth iFFT. White lines in Figure 4.4(b) are the theoretical propagation length $L = 1/2Im(k_{odd})$ for the odd mode. We report the theoretical L for different values of the damping parameter γ, determining the imaginary part of the SiC dielectric function and the SPhP damping. Experimentally, we extract the propagation length L by fitting each row (each frequency) of Figure 4.4(b) with an exponential function. We plot the extracted values as blue lines in

Figure 4.4(b) for frequencies where the exponential fit gives reliable results. We find that the value of γ in these films has to be in between 3 and 6 to reproduce the experimental data. Values as low as $\gamma = 1.4$ have been reported for high-quality bulk SiC, suggesting that improved crystal growth might lead to longer propagating SPhPs in free-standing SiC films. From the propagation length L and the group velocity $v_g = d\omega/dk$, the SPhP lifetime τ can be extracted as $\tau = L/v_g$. The average values of τ over the investigated frequency range are $\tau \sim 8$ ps for the 200 nm film and $\tau \sim 9.5$ ps for the 100 nm film.

The intensity profile of Figure 4.4(b) at fixed x is the result of the convolution between the sSNOM signal strength (which depends on the reflectivity of the material), and the unknown(possibly) frequency-dependent scattering efficiency of the window edge. The maps in Figure 4.4(c) represent the phase profile of SPhP, clearly showing the stronger wavelength shrinking for the T = 100 nm membrane. Together, Figure 4.4(b,c) gives a visual representation of the experimentally measured edge-launched SPhP excitation efficiency, propagation length, and wavelength shrinking.

4.2 Tuning of phonon polartion vortices via sublinear dispersion

Submitted as: "Tuning of phonon polartion vortices via sublinear dispersion"

Andrea Mancini1, Lin Nan, Rodrigo Berté, Emiliano Cortés, Haoran Ren, and Stefan A. Maier.

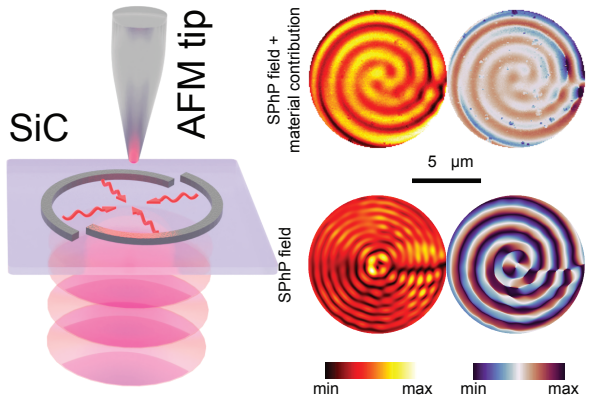

The SPhPs in suspended SiC membrane were experimentally explored in the previous section. With the experiences in the characterization and data treatment, the possibility of manipulate the topological charge in such system through designing the sub-diffraction SPhPs structures has been sought.

Optical vortices (OVs) promise to greatly enhance optical communication rates via orbital angular momentum (OAM) multiplexing. The need for on-chip integration of OAM technologies prompted research into highly confined polaritonic OVs. How-

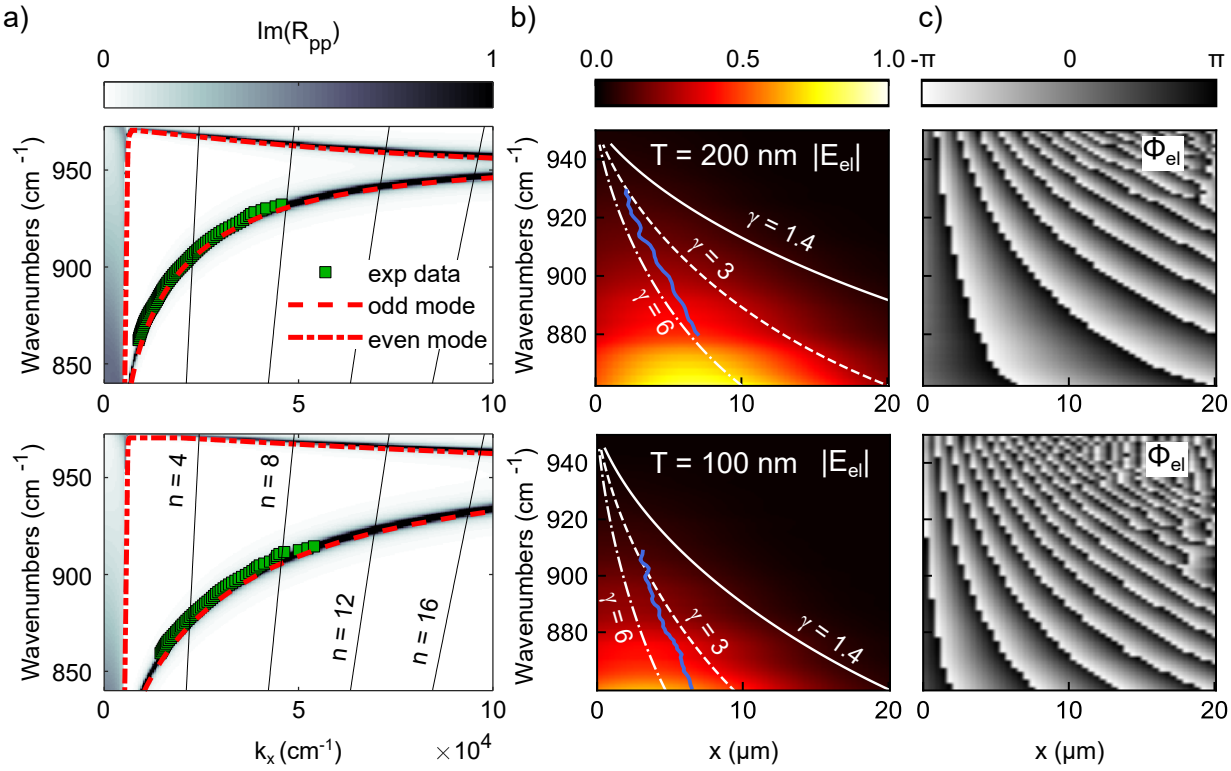

Figure 4.4: Retrieval of the SPhPs dispersion from the isolated edge-launched branch. Transfer matrix calculation of the imaginary part of the complex Fresnel reflection coefficient $\mathrm{Im}(R_{pp})$ for membranes of $T = 200\,\mathrm{nm}$ (top) and $T = 100\,\mathrm{nm}$ (bottom). Red dashed lines are analytical solutions for the even and odd modes from equations 4.3 and 4.4. Green squares are extracted from the experimental data by fitting the isolated edge-launched SPhPs and inverting the relation $k_{el} = f(\theta, \varphi, k_{SPhP})$. Thin black lines indicate the confinement factor $n = k_x/k_0$. Amplitude (b) and phase (c) obtained by iFFT of the isolated edge-launched polariton branch. White lines in (b) correspond to the theoretical value for the odd mode propagation length for different values of the damping parameter γ, while blue lines are the experimentally extracted values of the propagation length.

ever, up to this point the topological order of these OVs was fixed by the structure used for the transduction from free-space OAM beams to surface polaritons. Here, we overcome this limitation via dispersion-driven topological charge tuning. We switch the OV topological charge within a small $\sim 3\%$ frequency range by leveraging the strong sublinear dispersion of low-loss surface phonon polaritons (SPhP). We directly map the near-field signature of SPhP OVs in silicon carbide suspended membranes through transmission scattering-scanning optical near-field microscopy. We further explore the deuterogenic effect, which predicts the coexistence of multiple topological charges in polaritonic OVs. Our work demonstrates a viable method to manipulate the topological charge of polaritonic OVs, paving the way for the exploration of novel OAM-enabled light-matter interactions at mid-infrared frequencies.

Vortices with defined topological features are an ubiquitous phenomenon in physics, appearing in different systems including superconductors [167], superfluids [168], exciton polaritons [169, 170] and magnetic materials [171, 172]. Recently, propagating vortex beams characterized by twisted helical wavefronts carrying intrinsic orbital-angular momentum (OAM) have been realized with electrons [173, 174], neutrons [175, 176] and helium atoms [177], providing a new emerging tool for the investigation of fundamental particles and interactions [178]. Optical vortices (OVs), the photon counterpart of such beams, constitute a theoretically unbounded set of orthogonal OAM modes, promising multiplexed optical [179–181] and quantum [182–184] information processing. Pioneered by Allen [185], OVs are most usually generated by spiral phase plates [180], spatial light modulators (SLM) [179], and more recently with metasurfaces [186–191]. Regardless of the method, the minimum size of free-space OVs is fundamentally limited by the diffraction limit of light. On the other hand, reduction of the OVs footprint is required for applications such as on-chip integration [192–196] and unveiling of new light-matter interaction regimes [197–199].

A route for realizing subwavelength OVs is via coupling OAM beams to highly confined surface states such as Surface Plasmon Polaritons (SPPs) [18, 200–208] and Surface Phonon Polaritons (SPhPs) [5,209,210] through spin-orbit interactions [211]. However, the topological charge ℓ of these polaritonic OVs is always a fixed quantity stemming from the interplay between the spin and OAM states of the incident light with the surface structure used for polariton launching, which can provide additional phase delay due to polariton propagation. The additional OAM $\Delta\ell$ imprinted by the structure can be written as:

$$\Delta\ell = \pm m\frac{\delta}{2\pi}k \tag{4.7}$$

where δ is the additional charge imparted by each one of the m arms of a vortex generator (VG) [200] and k is the polariton wavevector. The same principle holds for

spiral phase plates, where an azimuthally-varying phase delay is imparted by propagation in a medium with refractive index $\hat{n}$. In Figure 4.5(a) we report sketches illustrating the generation of free-space and polaritonic OVs through a spiral phase plate and a VG. As geometrical features of phase plates and VGs are pre-defined during fabrication, a way to tune $\Delta\ell$ according to eq. (4.7) is to increase the wavevector by an integer factor nk.

The required frequency variation to achieve a certain wavevector increment is governed by the dispersion, a general property of waves relating energy and momentum. It plays a pivotal role in electromagnetic waves propagation and light-matter interactions. For a spiral phase plate in vacuum, $\delta = h(\hat{n} - 1)$ in eq. (4.7) where h is the height and $\hat{n}$ the refractive index of the spiral plate. As n varies slowly for non-absorbing dielectrics and the light dispersion is linear, doubling the momentum requires a 100% frequency increase, making this approach impractical for most applications. In polaritonic OVs this tuning mechanism is potentially more beneficial as their dispersion lies to the right of the light line, approaching asymptotically the surface polariton frequency [5, 18]. In the graph of Figure 4.5(a) we compare the linear and sublinear dispersions of light and of a typical polariton, showing that with the same frequency change $\Delta\omega$, the associate momentum variation is much larger for polaritons Δk_{SP} than for free-space photons Δk. While great research efforts have focused on SPPs, their dispersion considerably departs from the linear behavior only in the region of high material losses [20], drastically reducing the propagation length.

SPhP thin films characterized by low losses and strong sublinear dispersion are an ideal platform for dispersion-driven topological charge tuning. Recently, this concept was implemented to produce distinct phonon-polariton vortices at different frequencies in an hBN film on gold [210]. However, the measured OVs profiles were distorted due to the tilted illumination used for the near-field mapping, obscuring a clear evaluation of the OVs topological order.

Here we demonstrate, via normal-incidence transmission near-field mapping, dispersion-tuned topological charges in highly confined SPhP vortices based on suspended 100 nm silicon carbide (SiC) membranes. We realize polaritonic OVs with distinct topological orders from the same VG by a small $\sim$ 3% variation in the excitation frequency. By introducing a set of suitable reference functions, we quantitatively determine the purity of the experimental SPhP vortices. We precisely track the evolution of the OV purity while changing the topological order through dispersion-tuning. Finally, we investigate the deuterogenic effect predicting the coexistence of multiple modes in polaritonic vortices [204].

4.2.1 Tuning the topological vortex via SPhP dispersion

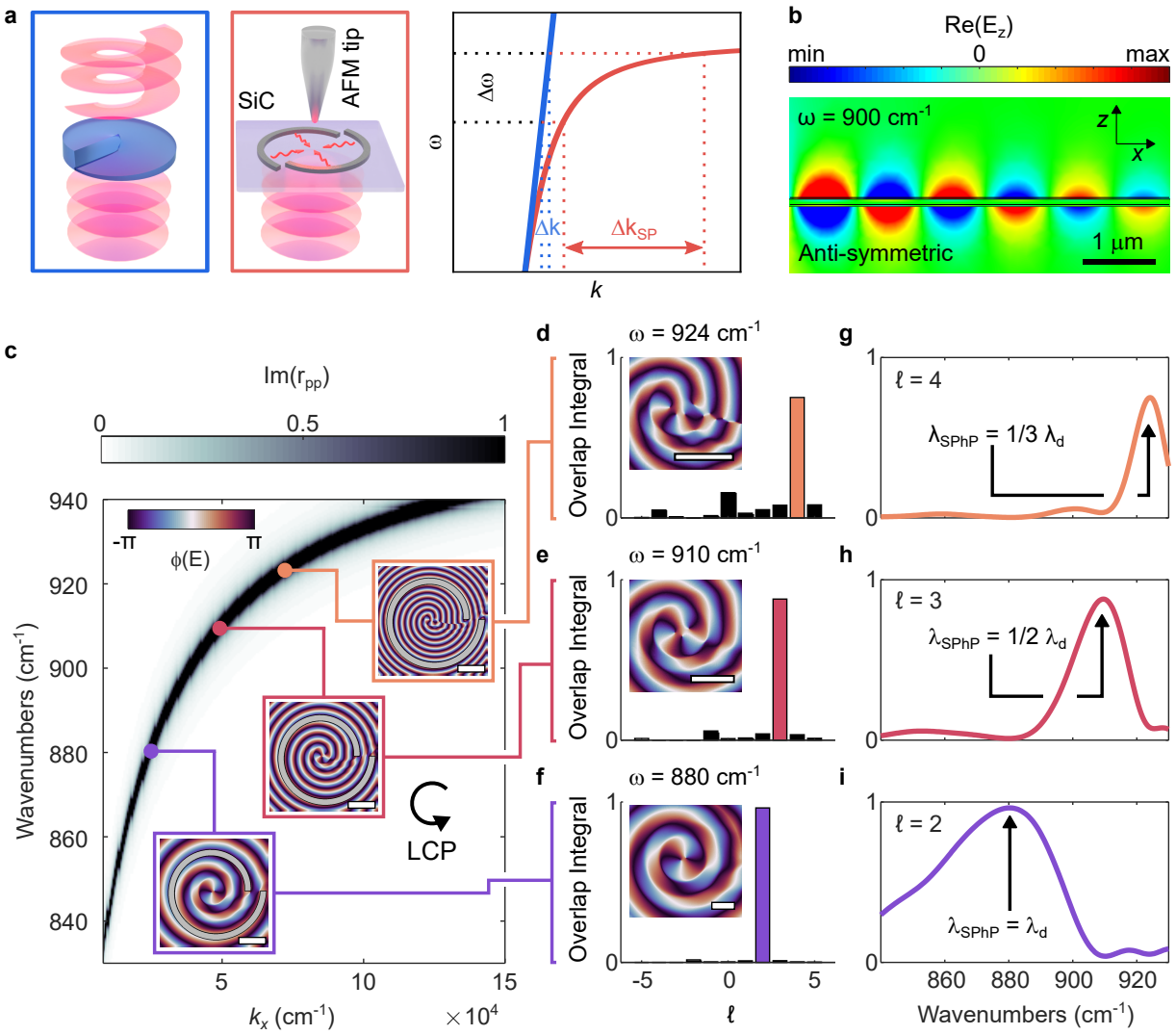

Figure 4.5: Topological vortex tuning via SPhP dispersion. (a) Dispersion-driven tuning for free-space and polaritonic OVs based on azimuthally-varying phase delay. The strong sublinear dispersion of surface polaritons allows a greater Δk increase for the same $\Delta\omega$ compared to the free-space case. (b) Simulated electric field distribution for the anti-symmetric mode in a 100 nm SiC membrane. (c) Calculated dispersion of the anti-symmetric mode of a 100 nm SiC membrane. As insets, simulated near-field phase maps for a SPhP vortex at three different frequencies launched by the same VG with $L = 1$ designed at $\omega = 880\,\mathrm{cm}^{-1}$ excited by LCP light. Scale bar: 2 µm. (d-e) Mode purity overlap integral at $\omega = 924\,\mathrm{cm}^{-1}$, $\omega = 910\,\mathrm{cm}^{-1}$ and $\omega = 880\,\mathrm{cm}^{-1}$. Insets: zoom of the maps center shown in (c). Scale bar: 1 µm (g-i) Overlap integral for orders $\ell = 4$, $\ell = 3$ and $\ell = 2$ as a function of excitation frequency. λ_d indicates the SPhP wavelength used for the VG design.

We map the near-field pattern of the polaritonic OVs by employing a transmission scattering-scanning near-field optical microscope (sSNOM). Transmission sSNOM has the advantage of normal incidence excitation and reduced tip-sample interaction, and has been the method of choice to investigate complex SPP patterns [201,202,212,213] and resonating plasmonic nanoantennae [214–217]. The experimental setup is sketched in the middle panel of Figure 4.5(a). Right (RCP) or left (LCP) circularly polarized light impinges from below the sample at normal incidence. SPhP are launched by a thin 20 nm Chromium (Cr) VG fabricated by standard electron beam lithography on the SiC membrane. The near field from the OVs is scattered by a metallic AFM tip, which oscillates at $\Omega \approx 280\,\mathrm{kHz}$ for background suppression obtained by demodulation of the signal at $n\Omega$ with $n > 1$. The width of the VG arms is chosen to be 2.5 µm, which we confirm is appropriate for efficient SPhP launching by estimating the appropriate ridge width for the VG fabrication by directly measuring the SPhP emission from a triangle-shaped Cr ridge. The minimum and maximum ridge thickness are 0.5 µm and 10 µm. We measure at a selected frequency $\omega = 880\,\mathrm{cm}^{-1}$ scanning from the flat side of the triangle, as shown in Figure 4.6(a). We can estimated the launching efficiency by averaging in row-by-row after, as shown in Figure 4.6(b). We start averaging from the first SPhP fringe to exclude the signal due to scattering at the Cr edge. Before averaging we rotate the image so that the SPhP straight edge of the Cr ridge is vertical. Knowing the slope of the triangle, we can relate the vertical position to the Cr width. We detect a maximum SPhP launching efficiency at around 4 µm. For ease of fabrication we choose a Cr width of 2.5 µm, where the launching efficiency is close to the maximum and the VG footprint is slightly smaller.

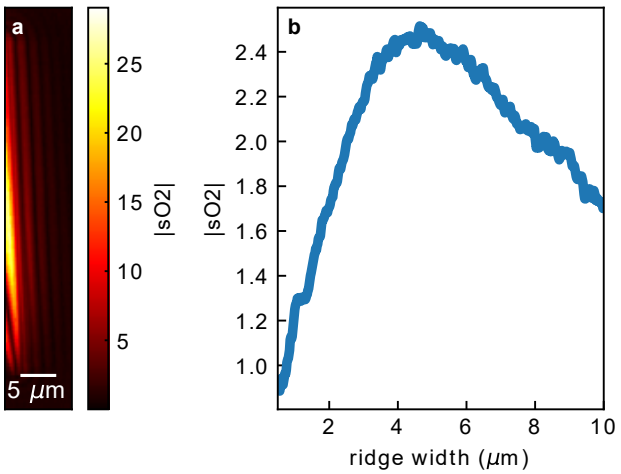

Figure 4.6: (a) Transmission sSNOM amplitude of SPhP launched by a triangle-shaped Cr ridge. (b) Extracted launching efficiency as a function of the Cr ridge width.

The VG shape is designed according to [200]:

$$r(\varphi) = \lambda_{SPhP}\left(M + \frac{mod(L\varphi, 2\pi)}{2\pi}\right) \tag{4.8}$$

where λ_{SPhP} is the SPhP wavelength and $mod(a, b)$ indicates the remainder of the division of a by b. L is the topological order of the VG determining the number of arms and M is an integer number setting the VG radius. The total OAM ℓ of the polaritonic OV at the design wavelength is given by $\ell = L + l + \sigma$, where l and $\sigma = \pm 1$ are the OAM and spin states of the incident beam.

SiC suspended membranes allow us to perform transmission measurements at normal incidence and at the same time provide strong SPhP confinement due to mode hybridization [162]. We use SiC as it features a wide, high-energy reststrahlen band with low losses, but the underlying physics is the same for other isotropic polar dielectrics. We avoid using reflection sSNOM, where light is focused on the tip at a tilted angle, as this inevitably distorts the OVs pattern for multiple reasons. First, the the VG design assumes excitation with a normal-incident plane wave; and second, the edge-launched SPhP fringes periodicity in reflection sSNOM depends on the relative angle between the incident beam k-vector and the edge in-plane normal direction [152,162,218,219], which varies along the VG geometry.

Hybridization between the individual SPhPs supported by the top and bottom interfaces of the SiC film occurs when the membrane thickness becomes comparable to the skin depth [162]. In this regime, splitting into two distinct modes with symmetric and anti-symmetric electric field distributions in the direction perpendicular to the film is observed [151]. The symmetric mode has higher energy and is strongly damped as the field is concentrated inside the lossy material. The anti-symmetric mode is found at lower energies and features strong wavelength shrinking, while maintaining good propagation properties [162]. We consequently use this latter mode for the realization of SPhP OVs. The simulated field distribution for the anti-symmetric mode at $900\,\mathrm{cm}^{-1}$ in a 100 nm SiC membrane is shown in Figure 4.5(b). The corresponding dispersion relation calculated through the transfer-matrix approach [220] is shown in Figure 4.5(c). The wavevector of the modes can also be calculated by solving numerically two implicit equations [162], which we use to determine λ_{SPhP} in eq. (4.8). To reduce the frequency shift needed for the dispersion-tuning mechanism, the polariton dispersion should be strongly sublinear, corresponding to a small group velocity $v_g = \partial\omega/\partial k$. As the mode hybridization reduces the group velocity of the SPhP, thin films are particularly suited to implement the dispersion tuning method. While the lowest group velocity is achieved close to the surface phonon polariton frequency $\omega_{SPhP} \approx 951\,\mathrm{cm}^{-1}$, losses grow close to ω_{SPhP}, resulting in a trade-off between v_g and propagation length.

The out-of plane component of the SPhP field launched by the VG ridge can be sim-

ulated through the Huygens principle [213, 221]. We consider here the E_z component, as it is the one mainly probed by sSNOM. We place a number N of dipoles in the positions determined by eq. (4.8) with each dipole producing a field $E_{z,i} = \exp(i\boldsymbol{k}_{SPhP} \cdot \boldsymbol{r_i} + \phi_i)/\sqrt{r_i}$ where $\boldsymbol{r_i} = \boldsymbol{r} - \boldsymbol{r_{0,i}}$ with $\boldsymbol{r_{0,i}}$ the position of the $i-$th dipole. The total field is computed by summing the contribution of all dipoles. RCP and LCP excitation are simulated by relating the phase ϕ_i of each dipole with its angular position.

In Figure 4.5(c) the dispersion-driven tuning of the vortex topological order is shown through simulations. A VG with $L = 1$ and $M = 2$ is designed according to eq. (4.8) at $880\,\mathrm{cm}^{-1}$ where the predicted SPhP wavelength is $\lambda_d = 2.5\,\mu\mathrm{m}$. We use the convention that anti-clockwise rotation is associated with a $+$, while clockwise rotation with a $-$ sign. The simulated phase of the SPhP field under LCP excitation is shown at $880\,\mathrm{cm}^{-1}$, $910\,\mathrm{cm}^{-1}$ and $924\,\mathrm{cm}^{-1}$ where the SPhP wavelength is predicted to be $\lambda_{SPhP}^{910\,\mathrm{cm}^{-1}} = \lambda_d/2$ and $\lambda_{SPhP}^{924\,\mathrm{cm}^{-1}} = \lambda_d/3$. From the simulated phase maps it can be seen that the resulting vortex OAM is $\ell^{880\,\mathrm{cm}^{-1}} = 2$, $\ell^{910\,\mathrm{cm}^{-1}} = 3$ and $\ell^{924\,\mathrm{cm}^{-1}} = 4$, as the geometrical phase delay imprinted by the VG goes from 2π at $880\,\mathrm{cm}^{-1}$ to 6π at $924\,\mathrm{cm}^{-1}$.

To quantitatively assess the purity of the obtained polaritonic OVs, an overlap integral between the simulated or experimental data with a set of reference functions is commonly used [190, 204]. While for free-space OAM beams Laguerre-Gaussian (LG) modes are employed as reference, these are not suited to represent the characteristic spiral phase pattern appearing in SPhP and SPP OVs, which is a result of material losses. We calculate from an integral approach the E_z of a SPhP vortex at various ℓ, constituting a set of suitable basis functions used to evaluate the OVs purity. We discuss how we obtain these reference functions in the following sections. The overlap integral OI can be computed as:

$$OI = \frac{|\int E_z E_{z,ref}^* \, dr \, d\varphi|^2}{\int E_z E_z^* \, dr \, d\varphi \int E_{z,ref} E_{z,ref}^* \, dr \, d\varphi} \tag{4.9}$$

where $E_{z,ref}$ is the reference function and E_z the vortex field of which we want to evaluate the purity. As the reference functions depend on k_{SPhP}, they vary depending on the operating frequency. An overlap spectrum can be computed by changing the topological order ℓ of the reference functions in eq. (4.9).

In Figure 4.5(d-f) the overlap spectra for the simulated maps reported in Figure 4.5(c) are shown. The spectrum in Figure 4.5(f) shows the high purity of the simulated $\ell = 2$ vortex. The purity decreases in Figure4.5(d, e), but the spectra clearly peak at $\ell = 3$ and $\ell = 4$, as expected. The overlap integral can also be evaluated at fixed ℓ as a function of frequency as shown in Figure4.5(g-i). A clear peak can be observed as expected for $\ell = 4$ at $924\,\mathrm{cm}^{-1}$, for $\ell = 3$ at $910\,\mathrm{cm}^{-1}$ and for $\ell = 2$ at $880\,\mathrm{cm}^{-1}$. Intriguingly, these plots demonstrate that from theoretical simulations a single fixed VG can lead to the creation

of vortices with different topological orders. By leveraging the strong sublinear SPhP dispersion, a slight tuning of the incident frequency is sufficient to switch the polaritonic vortex order.

4.2.2 Mapping the near-field pattern of the polaritonic OVs

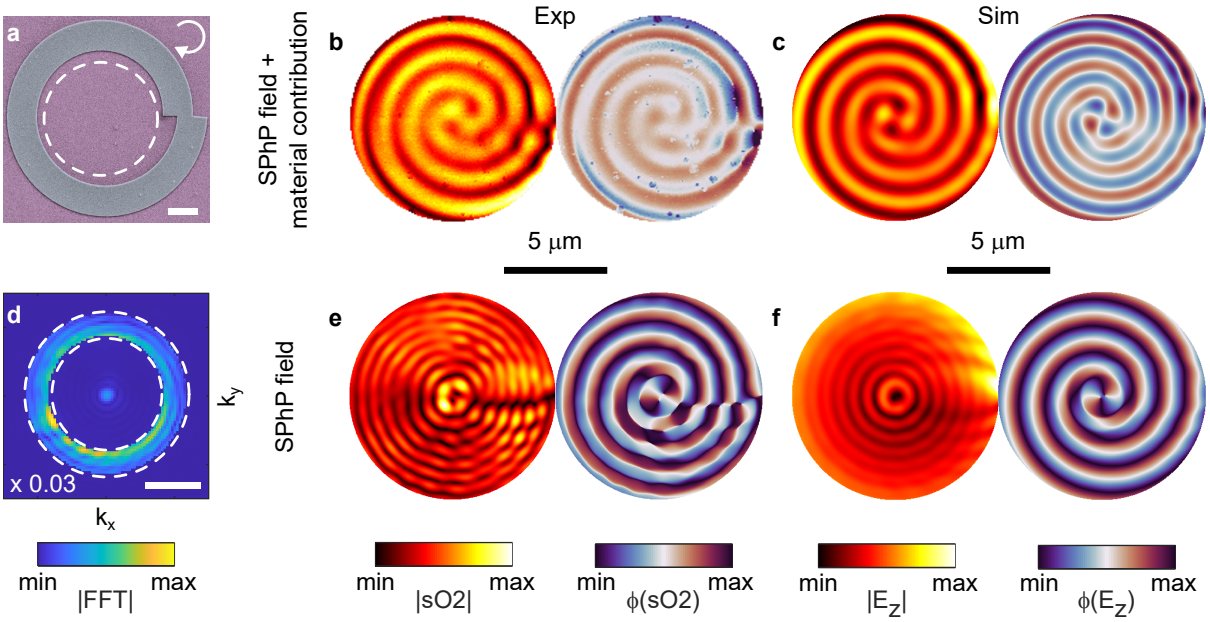

Figure 4.7: Experimental near-field mapping of a $\ell = 2$ SPhP vortex. (a) False color SEM of a VG with $L = 1$ excited by LCP light. Scale bar: 2.5 µm. Dashed lines indicate the region where experimental data are shown. (b) Transmission sSNOM amplitude and phase maps from the VG in (a) at $\omega = 913\,\mathrm{cm}^{-1}$. The pure SPhP field interferes with the bare material contrast. (c) Simulated corresponding vortex, where a constant complex background is added to the SPhP E_z field. (d) Removal of the material contrast through FFT filtering. Only the region between the dashed lines is kept. The rest of the map is shown multiplied by 0.03. The bright spot at the center represents the position-independent material contrast. Scale bar: $10k_0$ (e) Experimental maps after inverse FFT of the filtered data shown in (d). (f) Simulated corresponding SPhP E_z field.

In Figure 4.7(a) we report a SEM image of a VG with $M = 3$ and $L = 1$, designed at $\omega = 913\,\mathrm{cm}^{-1}$ and fabricated on top of the SiC membrane. The VG is excited with LCP light at the design frequency, and the measurements are shown for the circular region indicated by the white dashed line. The amplitude and phase experimental maps demodulated at twice the tapping frequency 2Ω are shown in Figure 4.7(b). The data are clipped and corrected. The as-recorder raw data for a $L = 2$ vortex are shown in Figure 4.8a, including

topography, amplitude and phase maps. We treat all the experimental maps in the same way. We first clip the data with a circular map, as shown in Figure 4.8b. Then we remove the scars produced by some dirt present on the sample from the fabrication steps as shown in Figure 4.8c. We accomplish this through the inpaint function of OpenCV [222]. We use the topography map for the threshold needed for scar correction, which we apply to the optical maps. The data above threshold in the topography map are shaded in red in Figure 4.8(c).

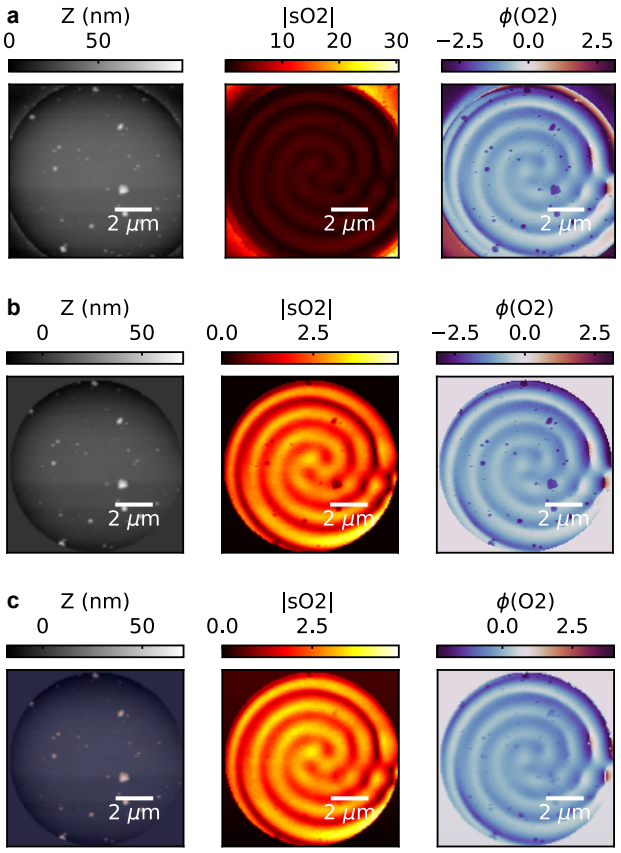

Figure 4.8: (a) Raw topography, amplitude and phase maps of of $\ell = 2$ vortex collected from transmission sSNOM. (b) the data are clipped with a circular mask. (c) Scars in the optical images are corrected by an image reconstruction algorithm. We use the topography for individuating the pixels to be corrected, which are shaded in red.

The resulting vortex is deeply subwavelength as $\beta = \lambda_0/\lambda_{SPhP} = 7$ at this frequency. We demonstrate a maximum SPhP vortex confinement of $\beta = 15.6$ at $\omega = 930\,\mathrm{cm}^{-1}$, corresponding to $\lambda_{SPhP} = 0.7\,\mu\mathrm{m}$ as shown below.

We investigate the maximum SPhP confinement at which we can produce a vortex. We fabricate multiple VG with $L = 1$ designed at different wavelengths, which we excite

with LCP light. The corresponding experimental amplitude and phase maps of the $\ell = 2$ vortexes are shown in Figure 4.9. We investigate a range of frequencies from 860 cm^{-1} to 930 cm^{-1} corresponding to confinement factors $n = \lambda_0/\lambda_{SPhP}$ from $n = 3$ to $n = 15.5$. The maps in Figure 4.9 are reported on the same scale to give a visual impression of the vortex shrinking with increasing frequency. In the background the SiC membrane dispersion calculate with the transfer-matrix method is reported

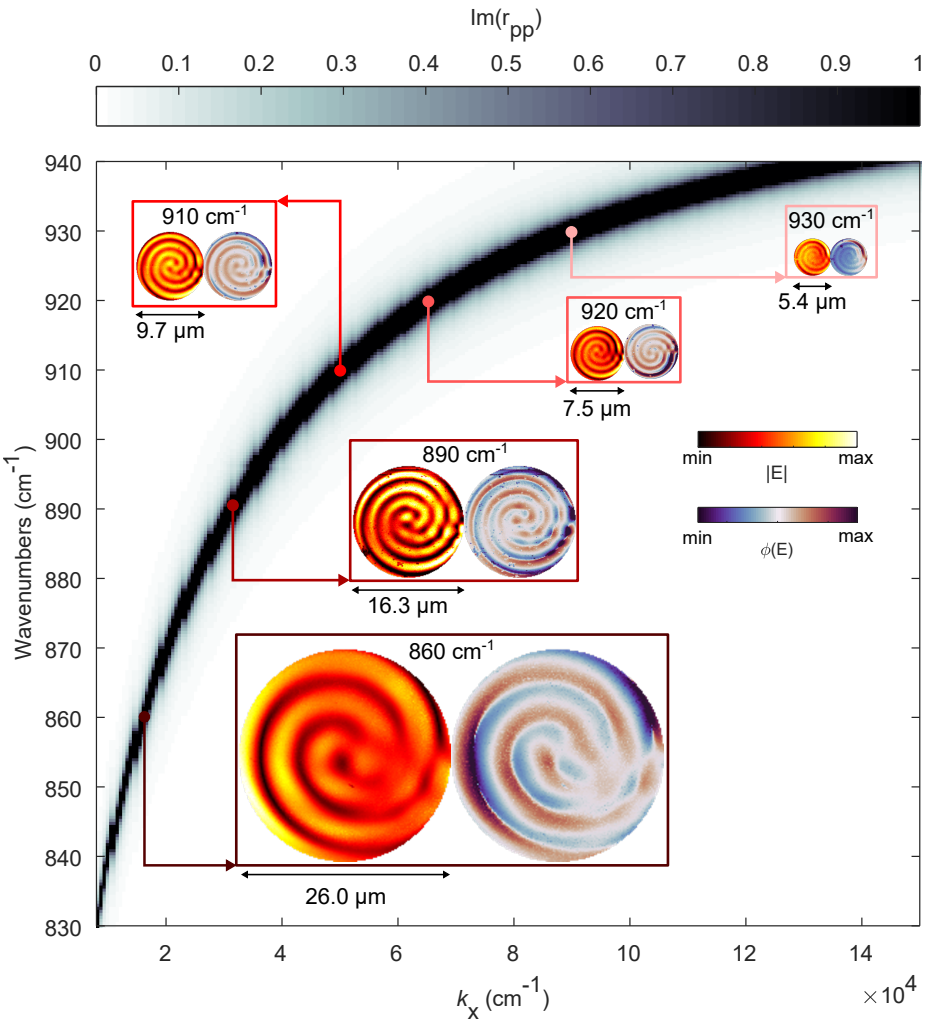

Figure 4.9: Eperimental amplitude and phase maps for SPhP vortex of order $\ell = 2$ at different excitation frequencies. In the background the claculated SiC membrane dispersion is reported.

In the sSNOM signal, the interference between the SPhP field and the bare response of the material, also called material contrast [223], is measured. This effect explains why we detect a spiral pattern for the vortex amplitude, while a series of concentric rings is normally expected [202]. At the same time the phase jumps along the SPhP propagation direction

are expected to go from $-\pi$ to π, while we measure smaller oscillations. To reproduce the experimental maps, it is sufficient to add a constant complex material background $E_{mat} = A_{mat} \exp(i\phi_{mat})$ to the simulated SPhP field. By choosing the correct values of A_{mat} and ϕ_{mat}, we obtain good agreement with the experimental maps as shown in Figure 4.7(c). The position-independent material contribution can be removed by filtering the 2D Fast Fourier Transform (FFT) of the experimental data. The absolute value of the experimental FFT map is shown in Figure 4.7(d). Only a region around the value of the predicted k_{SPhP} is retained by multiplication with a mask that is 0 outside the region highlighted by the white dashed lines in Figure 4.7(d), and 1 inside. In Figure 4.7(d) the region to be masked is multiplied by 0.03 to show the dominant central peak associated with the constant material contrast. The amplitude and phase maps obtained by inverse FFT of the masked complex FFT data are shown in Figure 4.7(e). The corresponding simulated SPhP field is shown in Figure 4.7(f), demonstrating good agreement with the retrieved experimental maps.

4.2.3 Definition of reference functions for vortex-purity estimation

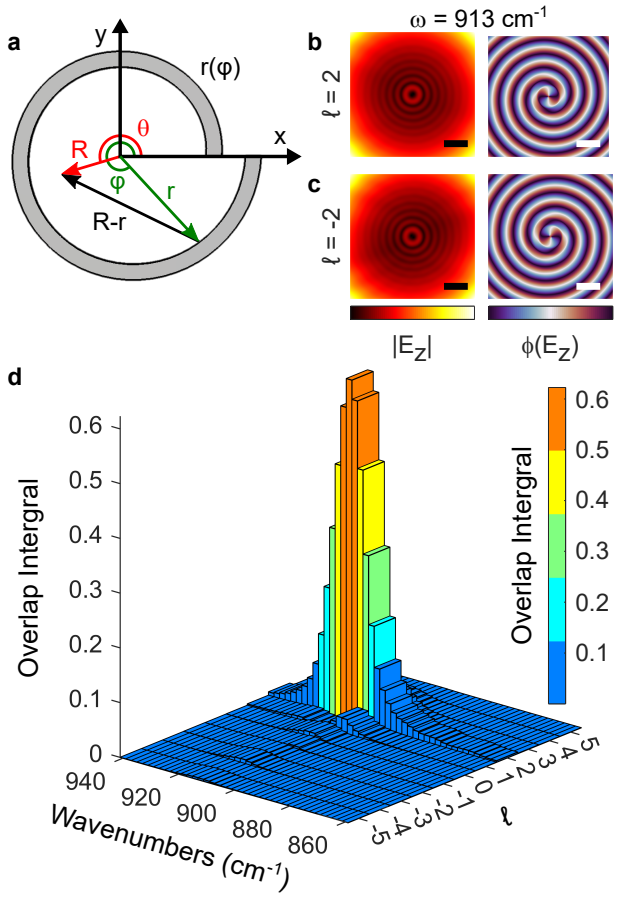

Figure 4.10: Definition of reference functions for vortex-purity estimation. (a) Sketch for the calculation of the reference functions. Example of the amplitude and phase of the calculated base functions for $\ell = 2$ (b) and $\ell = -2$ (c). Scale bar: 2 µm. (d) Overlap integral as a function of frequency and topological order ℓ for the FFT filtered experimental data shown in Figure 4.7e. The proposed metric shows excellent agreement with the visually assessed $\ell = 2$ order observed in experiments.

With the filtered maps shown in Figure 4.7(e), we can calculate the overlap integral in eq. (4.9) to evaluate the purity of the generated SPhP vortex. The usual LG modes are not suited as a set of reference functions because they do not show the spiral phase pattern we get from the experimental and simulated data. The fundamental difference is that for LG beams no losses are included as they represent free-space propagating beams. In the case of negligible SPhP losses, we show that each polaritonic vortex converges to the corresponding LG profile. We show here that the SPhP vortex converge to the LG

profiles in the absence of losses.

To define a set of basis functions, we consider the emission from an infinitesimal section of the VG ridge, which we assume to be acting as a dipole source. We only consider the out-of plane component of the SPhP field and assume incident radial polarization, so that the vortex OAM is solely determined by the VG structure and therefore $\ell = L$. The total field at coordinates (R, θ) can be expressed as the integral of the dipolar emission over the VG profile, as sketched in Figure 4.10(a). In polar coordinates [224, 225]:

$$E_{z,ref}(R,\theta) = \int_0^{2\pi} e^{i\boldsymbol{k}\cdot(\boldsymbol{R}-\boldsymbol{r}(\varphi))} r(\varphi)\, d\varphi = \int_0^{2\pi} e^{ik|R-r(\varphi)|} r(\varphi)\, d\varphi \tag{4.10}$$

where $\boldsymbol{k}$ is the SPhP wavevector and $r(\varphi)$ is the VG radius at the angle φ, as defined from eq. (4.8). The second equality in eq. (4.10) is justified since $\boldsymbol{k}$ and $\boldsymbol{R} - \boldsymbol{r}(\varphi)$ point in the same direction, and $|R - r(\varphi)| = R^2 + r(\varphi)^2 - 2Rr(\varphi)\cos(\theta - \varphi)$ by applying the cosine theorem. The value of M is chosen large enough so that we only consider the field produced inside the VG. We avoid any of the approximations (ignoring propagation losses $\mathrm{Im}(k) \approx 0$, considering $\boldsymbol{k}$ and $\boldsymbol{r}$ to be in opposite directions $-\boldsymbol{k}\cdot\boldsymbol{r} \approx kr$, assuming VG size much larger than the surface polariton wavelength $\lambda_{SP} \ll M\lambda_{SP}$) often employed to get an analytical solution of eq. (4.10) in terms of Bessel functions [200, 204, 224, 225]. We use eq. (4.10) to define a set of base functions by changing the value of L in eq. (4.8). We can confirm numerically minimal cross-talk between modes with different ℓ when integrating in a region close to the vortex center as shown below.

Earlier, we define a set of functions used as reference for the vortex purity estimation. We show that they have minimal cross-talk when calculating their overlap integral in a region around the vortex center. We show the overlap integral in Figure 4.11(a) the calculated overlap integral for the base functions calculated at $\omega = 900\,\mathrm{cm}^{-1}$. We detect only a small amount of cross-talk, which can be reduced by further decreasing the integration region if needed. In Figure 4.11(b) we show some examples of reference functions that are used to calculate the overlap integrals in Figure 4.11(a).

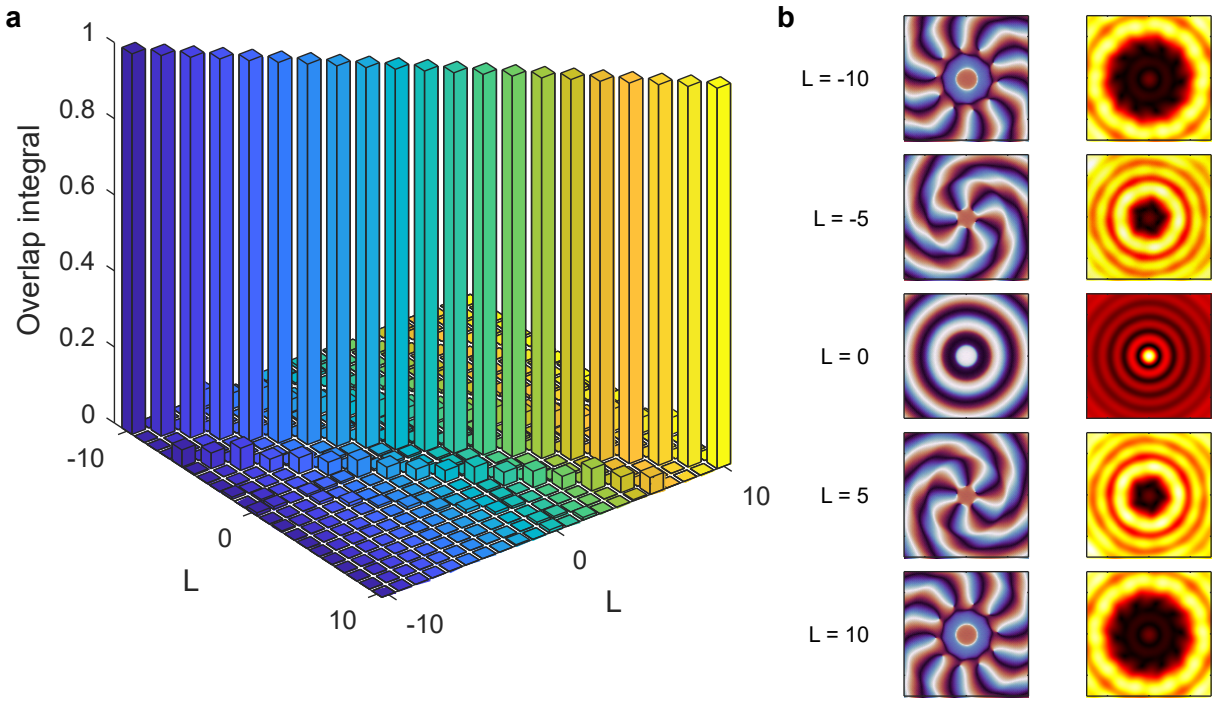

Figure 4.11: (a) Overlap integral for reference functions defined at $\omega = 900\,\mathrm{cm}^{-1}$. (b) Amplitude and phase of some base functions used for the calculation of panel (a). The size of the maps is $7 \times 7\,\mu\mathrm{m}^2$

These functions constitute the reference fields to be used in eq. (4.9) to estimate the vortex purity. They depend on the operation frequency through the SPhP momentum k_{SPhP}. In Figure 4.10(a, b) we show an example of the reference functions for $\ell = 2$ and $\ell = -2$, respectively.

We use these base functions to estimate the purity of the experimental filtered maps shown in Figure 4.7(e). The resulting overlap integrals as a function of both ω and ℓ are shown in Figure 4.10(d). We find a good vortex purity of > 0.6 for $\ell = 2$ with negligible cross-talk with other modes at the frequency of operation $\omega = 913\,\mathrm{cm}^{-1}$. To ensure optimal centering of the experimental data and reference functions, we shift the latter in 2-dimensions and we select the maximum overlap integral value to determine the shift needed to center both maps. We thus demonstrated a useful metric to evaluate the purity of polaritonic OVs from the near-field data. We stress that retrieving both the amplitude and phase of the field from the experiments is necessary to perform the integration in eq. (4.9) correctly.

4.2.4 Experimental realization of topological order tuning

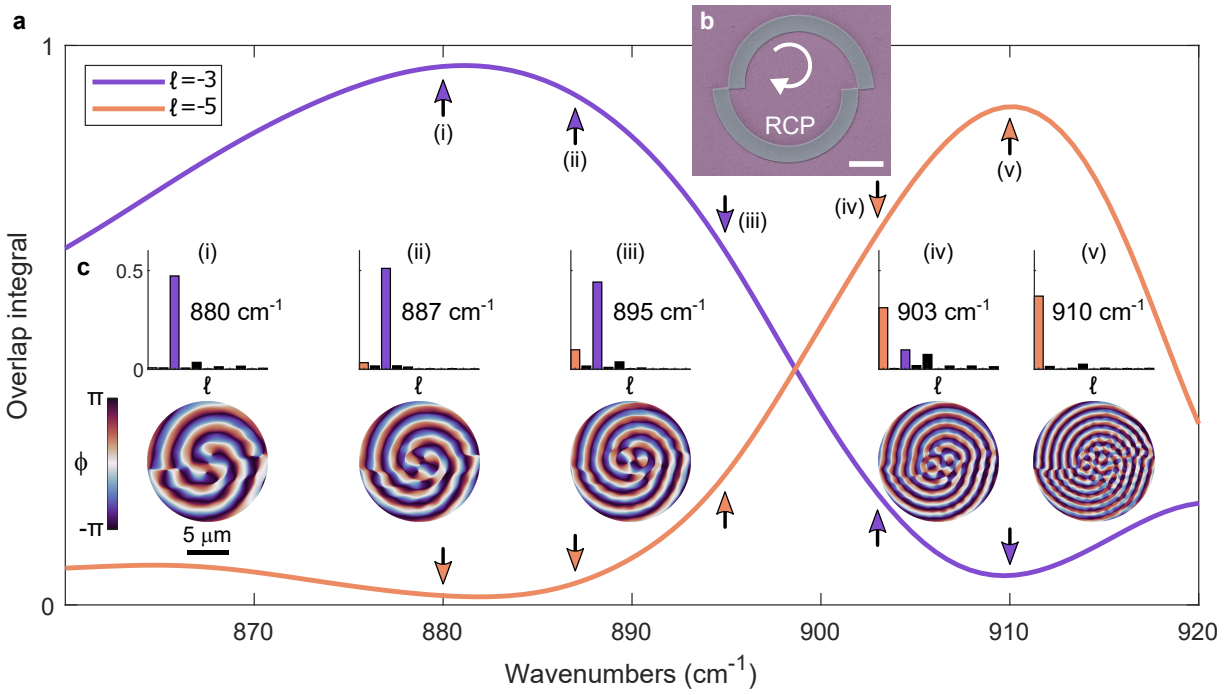

Figure 4.12: Experimental realization of topological order tuning via SPhP dispersion. (a) Simulated overlap integral as a function of frequency for a $L = -2$ VG excited with RCP light designed at $\omega = 880\,\mathrm{cm}^{-1}$. Purple and orange lines indicate overlap with $\ell = -3$ and $\ell = -5$ modes respectively. (b) False color SEM image of the $L = -2$ VG used for the experiments. Scale bar: 2.5 µm. (c) Top: overlap integral of the experimental data at different frequencies. ℓ goes from -5 to 5 and the purple and orange bars correspond to $\ell = -3$ and $\ell = -5$ respectively. Bottom: corresponding FFT filtered experimental phase maps. Arrows and roman numbers indicate the position of the predicted overlap integral at the corresponding experimental frequencies.

To experimentally confirm the dispersion-driven topological tuning mechanism, we quantitatively assess the topological order of a SPhP vortex when changing the excitation frequency. In Figure 4.12(a), we report the simulated integral overlap for a vortex designed at $\omega = 880\,\mathrm{cm}^{-1}$ with $L = -2$ and $M = 2$ excited by $\sigma = -1$ RCP light. We show the obtained spectra for $\ell = -3$ and $\ell = -5$ with purple and orange curves, respectively. A peak at the design frequency $\omega = 880\,\mathrm{cm}^{-1}$ for $\ell = -3$ can be seen in Figure 4.12(a) labeled as (i). The spectrum for $\ell = -5$ instead shows a peak at $\omega = 910\,\mathrm{cm}^{-1}$ indicated by (v), where $\lambda_{SPhP} = \lambda_d/2$ and λ_d is the SPhP wavelength at the design frequency. In Figure 4.12(b) we report a false-color SEM image of the fabricated VG. We carry out experiments at five different frequencies, $\omega = 880\,\mathrm{cm}^{-1}$, $\omega = 887\,\mathrm{cm}^{-1}$, $\omega = 895\,\mathrm{cm}^{-1}$, $\omega = 903\,\mathrm{cm}^{-1}$

and $\omega = 910\,\mathrm{cm}^{-1}$, labeled from (i) to (v) in Figure 4.12. For each wavelength we report in Figure 4.12(c) the FFT filtered phase map along with the calculated overlap integral. We indicate with purple bars the contribution at $\ell = -3$ and with orange bars the one at $\ell = -5$. The simulated values of the overlap integrals at the measured frequencies are highlighted by purple and orange arrows for $\ell = -3$ and $\ell = -5$, respectively. The experimental data are in excellent agreement with the simulations, as we can track the gradual change from $\ell = -3$ to $\ell = -5$ while also quantifying intermediate states given by a superposition of both vortex modes.

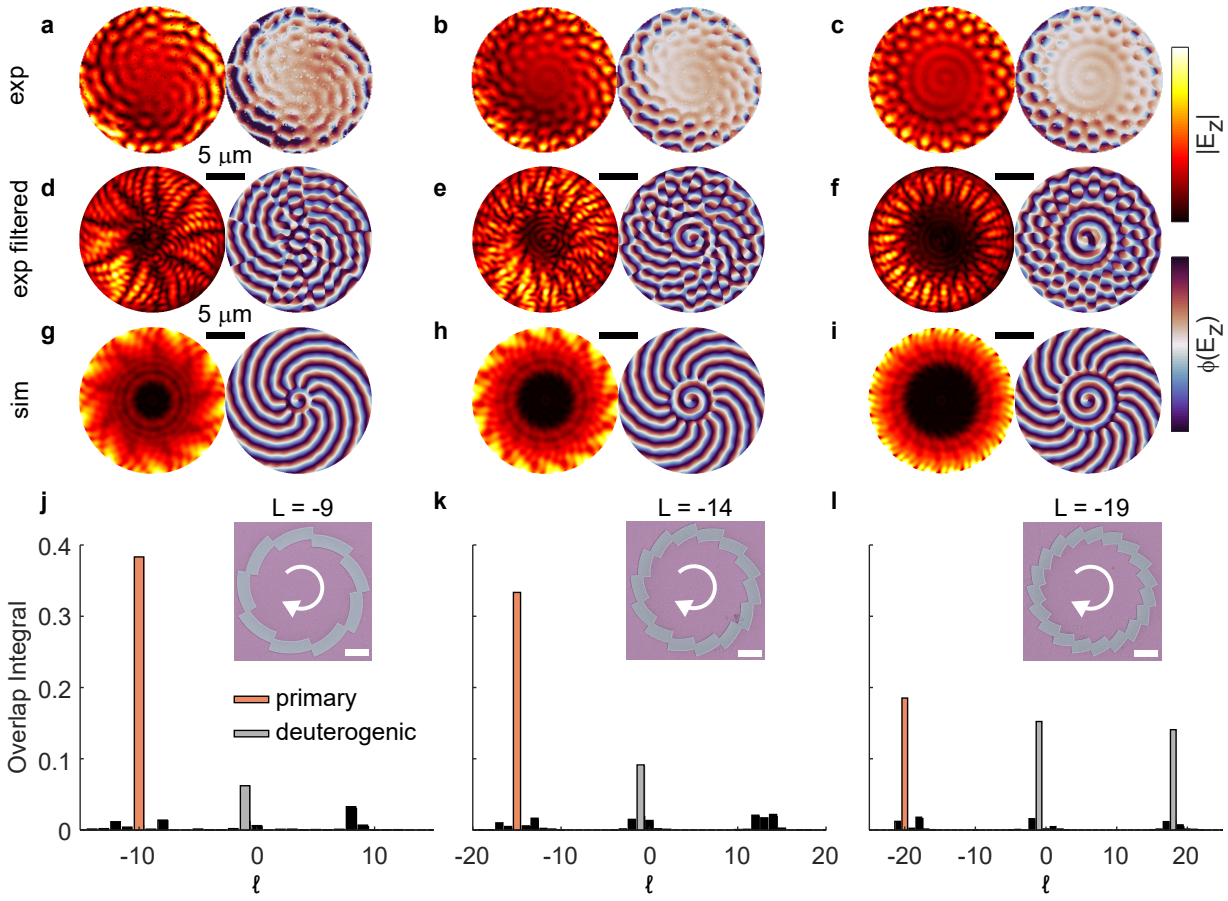

Figure 4.13: Deuterogenic effect in high order SPhP vortex at $\omega = 900\,\mathrm{cm}^{-1}$. Amplitude and phase transmission sSNOM maps at $\omega = 900\,\mathrm{cm}^{-1}$ for VG of $L = -9$ (a), $L = -14$ (b) and $L = -19$ (c) excited by RCP light. (d-f) Experimental maps after FFT filtering. (g-i) Corresponding simulated SPhP vortex. (j-l) Overlap integrals evaluated for the experimental data. Orange bars indicate the expected $\ell = -10$ in (j), $\ell = -15$ in (k) and $\ell = -20$ in (l). Gray bars indicated values of ℓ at which we detect the coexistence of additional modes predicted from the deuterogenic effect. Insets show false-color SEM of the fabricated VG used in the experiments. Scale bar: 5 µm

Thanks to the high purity of the measured SPhP vortices, we can investigate higher order modes. In particular we look into the deuterogenic effect, which predicts the coexistence of multiple OAM orders for polariton OVs produced by a VG [204]. According to this principle, the total OAM order of a polariton OV is given by

$$\ell = l + \sigma + nL \tag{4.11}$$

with $n = 0, \pm1, \pm2, \ldots$ and l and $\sigma = \pm1$ the OAM and spin states of the excitation beam. In Figure 4.13(a-c) we report amplitude and phase near-field maps for vortices of order $\ell = -10$, $\ell = -15$ and $\ell = -20$ respectively. The measurements are performed at $900\,\mathrm{cm}^{-1}$ with RCP excitation. As the footprint of higher order vortex is larger, we use here $M = 5$ in eq. (4.8) for the definition of the VGs. In Figure 4.13(d-f) we report filtered amplitude and phase maps, together with the corresponding simulations shown in Figure 4.13(g-h). We calculate the associated overlap integrals as displayed in Figure 4.13(j-l) together with false-color SEM images of the Cr ridges used for SPhP launching. We observe that for higher ℓ the mode purity decreases. In Figure 4.13(j, k) we detect the coexistence of modes $\ell = -10$ and $\ell = -15$ with the $\ell = -1$ order, as predicted from eq. (4.11) for $n = 0$ and $\sigma = -1$. The modes associated with the deuterogenic effect are indicated by gray bars. For the $\ell = -20$ vortex we can also observe a strong peak at order $\ell = 18$, which is again expected from eq. (4.11) for $n = -1$, $\sigma = -1$ and $L = -19$. While the deuterogenic effect for $n = 0, 1$ has been observed for SPP [204], we report here the first experimental detection of a $n = -1$ contribution, indicating that further terms in eq. (4.11) have to be considered to properly describe the generated polaritonic OV.

Intuitively, the generation of the central $\ell = -1$ vortex can be associated with the SPhP launched by the corners of the VG arms, which overall constitute a circle of emitting dipoles. In this case there is no additional phase delay from the structure, and the vortex ℓ is equal to the sum of the SAM and OAM of the incident beam. This effect can be attenuated by reducing the number of arms of the VG and increasing the phase delay imprinted by each section of the VG. A balance between attenuation of the central lobe and the azimuthal distortion due to propagation losses has to be found depending on the application.

4.3 Bound state in the continuum with SiC Babinet structures

In preparation as: "Phonon polarition bound state in the continuum in Babinet metasurfaces"

Lin Nan, Andrea Mancini, Thomas Weber, Rodrigo Berté, Emiliano Cortés, Andreas Tittl, and Stefan A. Maier.

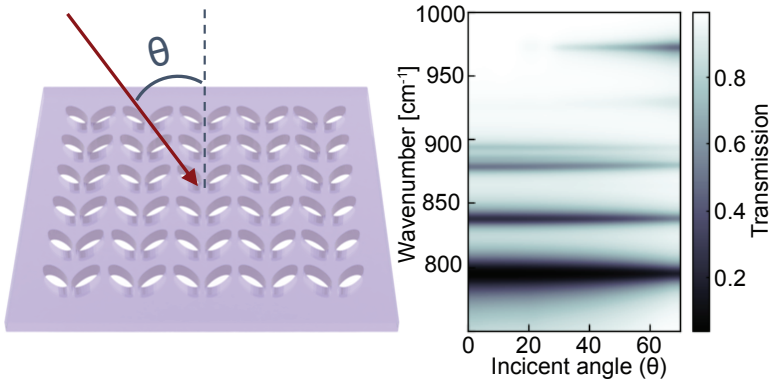

In the previous section, we have demonstrated tuning the topological orders with structures that supports surface phonon polaritons (SPhPs) in the near-field. In this following section, it will be demonstrated that the SPhPs structures can be further developed for far-field modulation.

SPhPs nanoresonators are capable of enhancing the coupling between molecular vibrations and infrared light, leading to the creation of localized hybrid polariton modes that can be studied using far-field spectroscopy to analyze nanoscale vibrational strong coupling (VSC). In particular, these nanoresonators can exhibit bound states in the continuum (BIC) modes, which are resonant modes that do not radiate and are immune to radiation losses, allowing for strong coupling with minute amounts of matter. To investigate the BIC modes of PhP nanoresonators composed of SiC and their interaction with molecular vibrations, Fourier transform infrared (FTIR) spectroscopy is utilized. In this study, the SPhPs meditated BIC metasurfaces were fabricated on suspended SiC films on Si frames and demonstrated the incident light angle independence of the metasurface and strong VSC with polyehylene glycol (PEG) molecules. To our knowlege so far, it will be the first reported BIC that is supported by SPhPs that is invariant to the incident light angles.

4.3.1 Bound state in the continuum

High-quality factor Q is a common physical characteristic that describes how much energy a physical system can store. In nanophotonic systems, traditional methods for

achieving high-Q resonances at the nanoscale involve driving below the optical wavelength using total internal reflection, such as microcavities based on whispering gallery modes and photonic bandgap cavities, which can utilize high-Q values to modulate optical phenomena like Raman lasers and harmonic generation. As research has progressed, some attention has shifted to metal-based metasurfaces, but the inherent Ohmic losses of metals result in broad spectral resonances in the visible and near-infrared, making it difficult to achieve narrowband high-Q values. Recently, metasurfaces based on all-dielectric materials have overcome this drawback of metal losses and exhibited high-Q values through "Fano" resonances and "EIT" phenomena, driving a range of interesting fundamental research and practical applications such as refractive index sensing and nonlinear optical effects. The continued pursuit of compact photonics systems supporting high-Q values has fostered rapid development of a class of structures called bound states in the continuum (BIC). This chapter will introduce the basic concepts of BIC in the continuum and primarily discuss BIC in symmetrically protected continuum.

BIC was first proposed by von Neumann and Wigner in the field of quantum mechanics in 1929 [226]. They theoretically constructed a special three-dimensional quantum potential well, whose potential energy function oscillates in a certain way and extends to infinity. This allows the potential well to support a special type of electronic state, whose energy is within the continuous spectrum but whose wave function is still confined to the potential well, i.e. BIC in the continuous domain. Since the potential well is too difficult to implement, BIC of electrons has not been observed experimentally. Considering the universality of the Schródinger's equation in wave physics, the concept of BIC also applies to electromagnetic waves and sound waves, and has gradually been observed experimentally [227]. In recent years, thanks to the development of photonics, metasurfaces and photonic crystals, they have become ideal platforms for studying BIC. Based on the unique non-radiative properties of BIC, it has been widely applied to applications such as lasers, sensing, filters, and low-loss optical fibers.

In a quantum mechanical system, the energy spectrum of a typical quantum well contains two types of modes: the continuum, where the wave function distribution can propagate to infinity, and the bound states, which are confined within the potential well. The energy levels of these two types of modes are clearly discretely distributed. However, when a special oscillation is introduced into the potential well, an unusual BIC can be obtained, which is confined around the potential well in space, but its energy level is within the continuum. Figure 4.14 shows an illustration of a BIC. For an open photonic structure, its spectrum is usually composed of continuous extended states (blue region) and discrete bound states (discrete green solid line). Taking a sine wave$e^{-i\omega t}$ as an example, where t represents time and ω represents angular frequency. For a resonance mode (orange solid

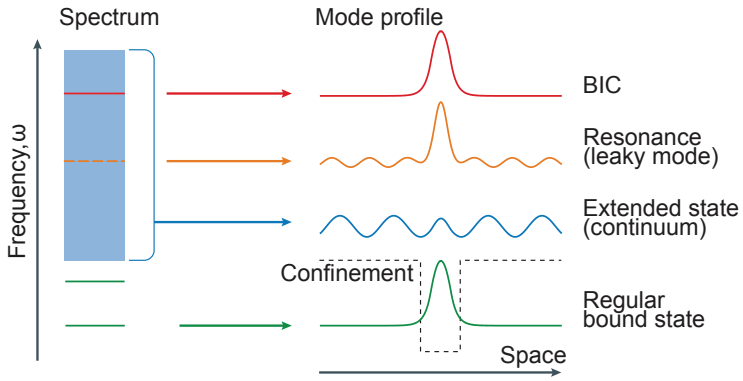

Figure 4.14: BIC photonic systems. In an open system, the frequency spectrum is composed of a range of spatially extended states (blue) and discrete levels of bound states (green) that do not emit outgoing waves. The confinement of the bound states is due to a constraining structure or potential (represented by the black dashed line). States within the continuous spectrum usually couple with the extended waves and emit radiation, leading to leaky resonances (orange). The BIC (red) exist within the continuous spectrum but remain localized and do not radiate [227].

line) located in the continuum, it appears as a bound state in the localized space, but in fact it couples with extended states and leaks to infinity. The mode has a complex frequency $\omega = \omega_0 - i\gamma$, where the real part ω_0 represents the resonance frequency, and the imaginary part γ represents the speed at which the mode leaks into free space [228]. For bound states outside the continuum, they cannot couple with radiation channels, and their eigenfrequency is a real number. In addition to these two common modes, there is another peculiar optical mode: BIC. This mode also lies within the continuum range but can be perfectly localized in the photonic structure in space without leaking into free space. Therefore, the eigenfrequency of BIC is also a real number, with γ equals to zero, a zero linewidth, and a quality factor $Q = \omega_0/2\gamma$ being infinity.

According to their different generation mechanisms, BIC can be divided into two categories: symmetry-protected BIC and accidental BIC, the former resulting from the mismatch between the mode itself and the symmetry of the radiation channel in the environment, while the latter resulting from interference effects between multiple radiation channels or modes. In this study we will mainly discuss the former. Figure 4.15 shows the basic idea of the symmetry-protected BIC and accidental BIC [229]. One way to explain this can based on the vanishing of Fourier coefficients associated with open diffraction channels, which occurs due to the symmetry of the photonic structure. At high-symmetry points of the reciprocal space, such as the Γ point, the continuous spectrum is divided into modes of different symmetry classes with respect to the reflectional and rotational symmetry of the photonic system. Bound states of one symmetry class can be embedded

in the continuum of another symmetry class, and their coupling is forbidden as long as the symmetry is preserved. Such BIC is referred to as symmetry-protected, and they can be interpreted in terms of topological charges defined by the number of times the polarization vectors wind around the BIC, which are presented as vortex centers in the polarization field [230]. In contrast to the symmetry-protected BIC, accidental BIC [227, 230–233] can be observed out of the Γ point due to the accidental nulling of the Fourier (coupling) coefficients via fine tuning of parameters of the photonic system [234].

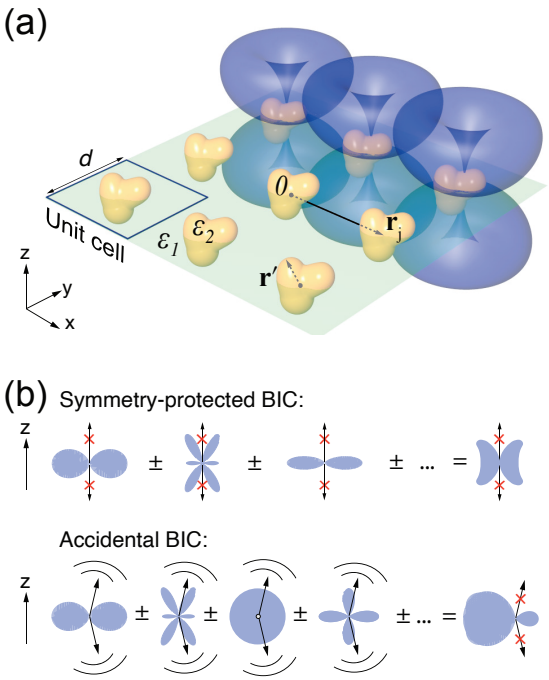

Figure 4.15: (a) An example of dielectric metasurface and it's meta-atoms (b) Formation mechanism of symmetry protected, at-off-Γ, (upper panel) and accidental, off-Γ, (lower panel) BIC as an interference of multipole moment of the unit cell. [229].

The topological nature of symmetry-protected BIC can be explained through the robust BIC in photonic crystal shown in Figure 4.16 In photonic crystal slabs, the polarization direction of the far-field radiation is represented by a 2D vector, $E_{//}= (E_x, E_y)$. BIC exist at the intersection points between the nodal lines of $E_x = 0$ and $E_y = 0$, and they do not radiate. In the k-space, each BIC is surrounded by a polarization vector that forms a vortex, and each vortex has a corresponding topological charge (q). Topological charges are conserved and quantized quantities protected by boundary conditions, and therefore, a BIC cannot be removed unless it is cancelled out by another BIC with the exact opposite topological charge. The occurrence of a BIC requires significant changes in the system parameters, which cannot suddenly disappear. Examples of different topological charges

(q = 1, -1, -2) are shown in Figure 4.16(b), along with a case with no BIC (q = 0).

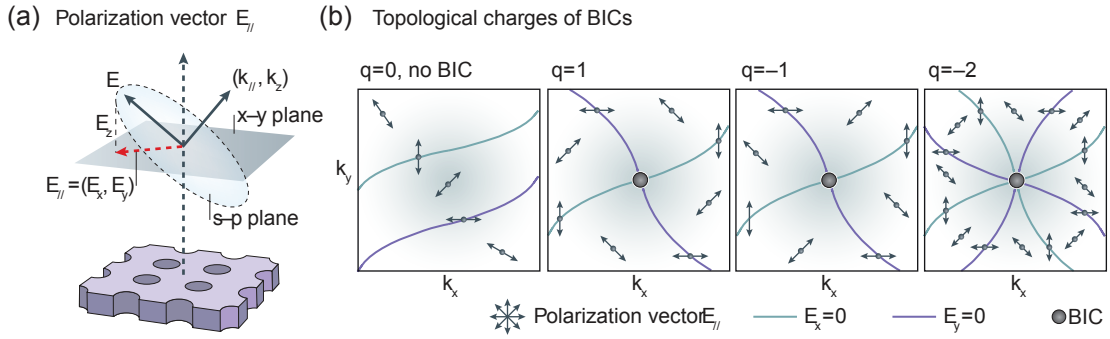

Figure 4.16: Topological nature of BIC in 2D photonic crystals. Each BIC in k-space is surrounded by a polarization vector that forms a vortex with a topological charge (q). The topological charges of BIC are conserved and quantized quantities, meaning that they cannot be removed unless they are cancelled out by another BIC with the exact opposite topological charge. The figure shows examples of BIC with different topological charges (q = 1, -1, -2) and a case with no BIC (q = 0) [227].

The strong polarization dependency Figure 4.16 translates to that in a BIC system, the probing and observing orientation is a crucial factor. Generally, for designing a robust optical system, this kind of strong dependency is considered to undesirable. However, the study has shown in Figure 4.14 successfully exploded this feature to multiplex the resonances of a single metasurface through changing the indecent and observation angle for molecular sensing in IR. With incoherent illumination and detection, this was able to correlate the molecular absorption to the total reflectance signal at each incident angle allowing spectrometer-less operation.

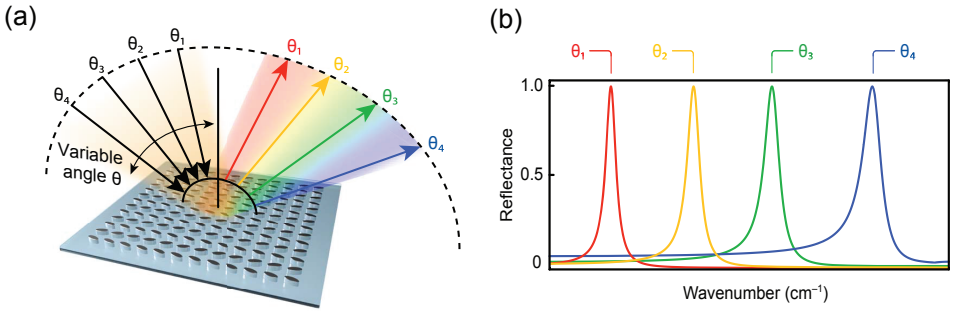

Figure 4.17: A metasurface made of germanium and featuring high-Q all-dielectric properties can produce extremely sharp resonances at specific frequencies for any angle of incidence (θ) while also covering a broad spectral range. By continuously adjusting the incidence angle, a wide range of resonances can be generated within a desired fingerprint range, making this angle-multiplexed configuration well-suited for surface-enhanced molecular absorption spectroscopy in the mid-infrared range [235].

It should be noted that true Friedrich–Wintgen type of BIC only exists in infinitely large and lossless structures or in structures with extreme parameters. In actual experiments, due to the limited size of the samples, the materials used are not completely lossless, and the scattering loss caused by processing errors and structural defects, etc., it is impossible to realize the true BIC. However, it is possible to obtain quasi-bound states in the continuum (Q-BIC) with finite high Q values by introducing a perturbation. By improving the system parameters such as topological parameters and the position of electromagnetic response in momentum space, the characteristic of the resonance peak disappearing can still be observed. At the same time, quasi-BIC can be excited and detected in the far field, which enables the experimental observation of this optical mode and implementation for various applications. Hence, BIC structures that we deal with in this study is in fact Q-BIC.

4.3.2 Tuning the BIC resonance in SiC

BIC resonances occur when a radiating system (such as a nanoparticle) is embedded in a host medium in such a way that its radiative losses are inhibited, leading to a sharp resonance peak in the scattering spectrum. The BIC resonance frequency is determined by the size and shape of the resonant structure as well as the refractive index of the host medium. There are several well-known ways to tune the BIC resonance.

For this study, negative elliptical nanoantennae are employed. These antennae consist of a pair of elliptical hollow structure with subwavelength dimensions on a suspended 100 nm SiC membranes, which can support resonant modes that are confined within the structure due to destructive interference with other modes that propagate away from the structure.

One advantage of using elliptical nanoantennae for BIC resonances is that they can be easily fabricated using standard lithography techniques. Additionally, their elliptical shape allows for tuning of the resonance frequency by adjusting the major and minor axis dimensions of the ellipse. This tunability makes them a versatile platform for a wide range of applications, including sensing, spectroscopy, and optical communication.

Another advantage of using elliptical nanoantennae for BIC resonances is that they can support both electric and magnetic dipole modes, which can enhance the light-matter interactions in the near-field of the structure. Furthermore, the symmetry breaking of the elliptical shape can lead to the excitation of higher-order modes that are not present in symmetric structures, further expanding the range of available resonances.

The most straight forward way to tune the BIC resonance is by changing the unit cell size, ie., scaling factor. The size scaling factor of a resonant structure refers to the change in its size and shape, which affects its resonance frequency when it is embedded in a host medium. Specifically, increasing the size scaling factor of a resonant structure in a host medium with a high refractive index leads to a red-shift of the BIC resonance frequency. This is because a larger resonant structure can excite a longer wavelength resonance mode, and the higher refractive index of the host medium further shifts the resonance frequency to longer wavelengths. On the other hand, decreasing the size scaling factor of a resonant structure in a host medium with a low refractive index leads to a blue-shift of the BIC resonance frequency. This is because a smaller resonant structure can excite a shorter wavelength resonance mode, and the lower refractive index of the host medium further shifts the resonance frequency to shorter wavelengths.

The Figure 4.18 displays the BIC spectra obtained from both experimental measurements and numerical simulations for various size scaling factors of a resonant structure in a host medium. The simulations predict that as the size of the resonant structure decreases, the BIC resonance frequency shifts towards longer wavelengths, which is confirmed by the

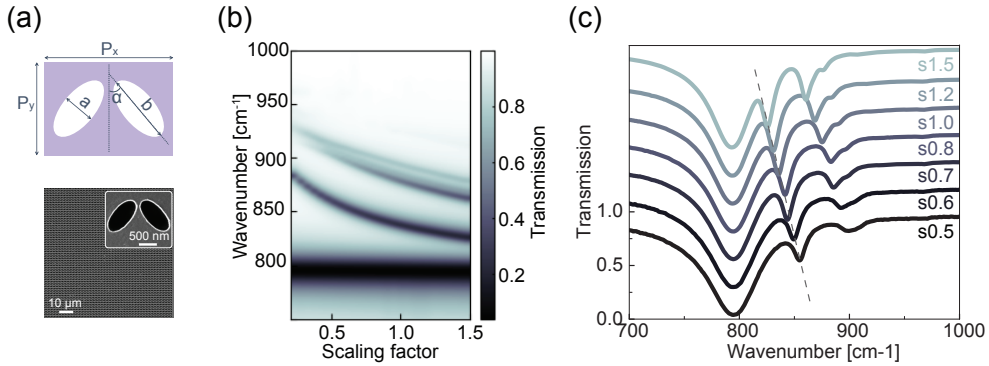

Figure 4.18: By changing scaling factor, s, it is possible to tune BIC resonance. (a) Numerical calculation for the changing unit-cell scaling factor, (b) an example SEM image of scaling factor 0.4 (c) FTIR spectra for s0.5 to s1.5. The base parameter for s = 1.0 was set as follows: a = 560 nm, b = 1190 nm, Px = 2100 nm, Py = 1610 nm, and $\alpha = 40°$. The dashed-line indicates the BIC mode. The constant peaks around 795 cm^{-1} arise from the material response of 100 nm SiC membrane. The other smaller peaks are combination of material response and higher order BIC modes.

experimental measurements. This red-shift of the BIC resonance frequency occurs because smaller resonant structures can excite longer wavelength resonance modes that are more strongly coupled to the host medium. Therefore, the Figure 4.18 provides further evidence that the size scaling factor is an essential parameter that significantly influences the BIC resonance frequency of a resonant structure in a host medium.

Another way to tune the BIC resonance in elliptical system is to break the symmetry of the antenna. One way to break the symmetry is by changing the angle between the major and minor axes of the ellipse. This can be achieved by using elliptical nanoantennae with non-uniform dimensions or by introducing a tilt angle between the antenna and the plane of incidence.

When the symmetry of the elliptical nanoantenna is broken, the BIC resonance splits into two orthogonal polarizations, with different resonance frequencies. The magnitude of this splitting depends on the degree of symmetry breaking, which is determined by the angle between the major and minor axes of the ellipse. By adjusting the angle, one can tune the resonance frequency of the BIC mode.

Furthermore, the polarization of the emitted light can also be controlled by adjusting the angle between the major and minor axes of the ellipse. The polarization of the emitted light is determined by the orientation of the electric and magnetic dipole moments of the antenna. By breaking the symmetry of the antenna, the orientation of the dipole moments can be controlled, leading to control over the polarization of the emitted light.

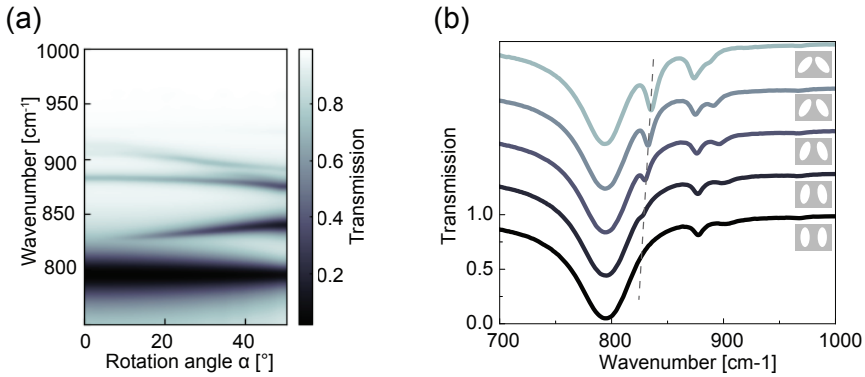

Figure 4.19: By changing the angle between the ellipses, α, it is possible to change the BIC resonance. (a) Numerical calculation for the changing α, (b) FTIR spectra for varying α from 0° to 40°. The base parameter for s = 1.0 was set as follows: a = 560 nm, b = 1190 nm, Px = 2100 nm, Py = 1610 nm. The dashed-line indicates the BIC mode.

4.3.3 Incidenct angle independence

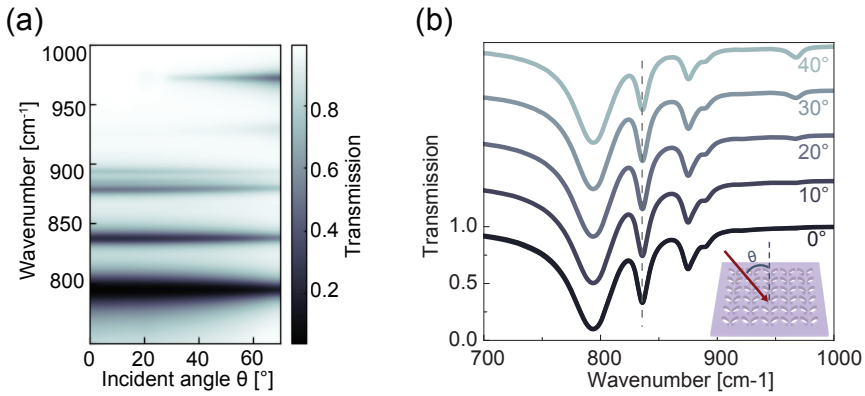

Figure 4.20: By changing scaling factor, s, it is possible to tune BIC resonance. (a) Numerical calculation for the changing unit-cell numbers BIC, (b) an example SEM image of scaling factor 0.4 (c) FTIR spectra for s0.5 to s1.5. The base parameter for s = 1.0 was set as follows: a = 560 nm, b = 1190 nm, Px = 2100 nm, Py = 1610 nm, and α = 40°.The dashed-line indicates the BIC mode.

In Chapter 2, the intrinsic nature of polarization dependence of a BIC structure was discribed. However, due to the extremely sub-diffraction size of the Babinet structure, it is reasonable to speculate that it may exhibit unusual behavior. To investigate this, FEM simulations was performed, and the results (shown in Figure 4.20) indicate that the Babinet BIC structure indeed shows an unusual incident angle-independent behavior, as predicted by numerical calculations.

This unique behavior can be attributed to the extremely small sub-diffractional unit-cell size of the Babinet structure, which is approximately 10 times smaller than the wavelength of the light of interest (i.e., the size of the unit-cell is only about 1/10 of the wavelength, which is around 11 μm). This type of behavior is only observed in Babinet structures, which are characterized by complementary arrangements of two materials that haver distinct refractive indices.

The small unit-cell size in the Babinet structure creates a high spatial frequency of the structure, which makes it difficult for the light to distinguish between different angles of incidence. As a result, the Babinet BIC structure exhibits angle-independent behavior, which is highly desirable for practical applications in nanophotonics and its applications.

Moreover, the angle-independent behavior of the Babinet BIC structure makes it possible to achieve high-efficiency light coupling over a wide range of incident angles. This is a significant advantage over conventional optical structures that typically exhibit strong polarization or angle dependence.

4.3.4 Near-field study on Babinet BIC

Opposite to the usual elliptical BIC with positive antennae, the BIC mode in Babinet structures are excited by the TE polarization. This can be shown from the near-field study that is shown in Figure 4.21. The near-field pattern was mapped by employing sSNOM that is described in Section 4.2. Transmission sSNOM has the advantage of normal incidence excitation and reduced tip-sample interaction. The probing wavelength was chosen to be at the BIC resonance and the polarization was set to excite the TE mode which is the BIC mode in our sample. The amplitude and phase profile from the measurement showed great agreement with the simulated result further demonstrating the unusual behavior of the Babinet BIC.

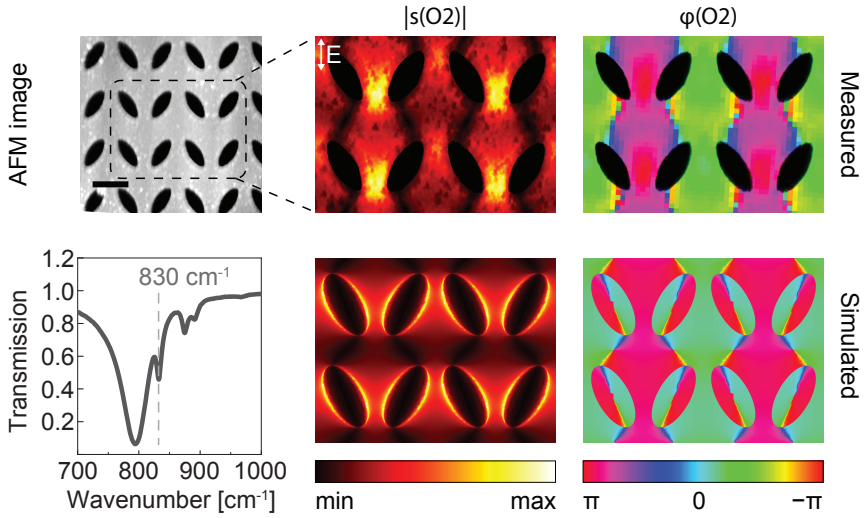

Figure 4.21: Experimental near-field mapping of a O2. Top left panel shows the AFM image from the near-field scanning area (scale bar: 1 μm). The right panel compares the experimentally acquired near-field O2 amplitude and phase with the simulated results. The near-field was mapped under transmission mode with TE polarization at the BIC resonance frequency, 830 cm^{-1}.The dashed-line indicates the BIC mode.

4.3.5 BIC driven vibrational coupling

Vibrational strong coupling refers to the interaction between light and matter when the energy difference between two vibrational states of a molecule matches the frequency of the light field. This results in the exchange of energy between the vibrational and electromagnetic modes, leading to the formation of hybrid light-matter states known as polaritons. In this regime, the coupling strength between the molecular vibrations and the electromagnetic field becomes comparable to the energy dissipation rates, resulting in an

exchange of energy between the two modes and a significant modification of the spectral properties of the system.

Vibrational strong coupling has been shown to be a promising approach for infrared (IR) sensing applications. In traditional IR spectroscopy, the absorption of infrared radiation by a material is measured and analyzed to provide information about the molecular vibrations of the sample. However, this approach is limited by the low sensitivity and resolution of conventional IR spectroscopy techniques.

With vibrational strong coupling it is possible to overcome some of these limitations by enhancing the interaction between the IR radiation and the sample, leading to significant changes in the spectral properties of the system. By tuning the resonance of a metasurface to match the vibrational frequency of the target molecule, it is possible to achieve strong coupling between the molecular vibrations and the electromagnetic field, resulting in the formation of polaritons.

This approach can provide several advantages over traditional IR spectroscopy, including enhanced sensitivity, increased spectral resolution, and the ability to detect small concentrations of molecules. Furthermore, the ability to tune the resonance of the metasurface to match the vibrational frequency of different molecules allows for the selective detection of specific analytes.

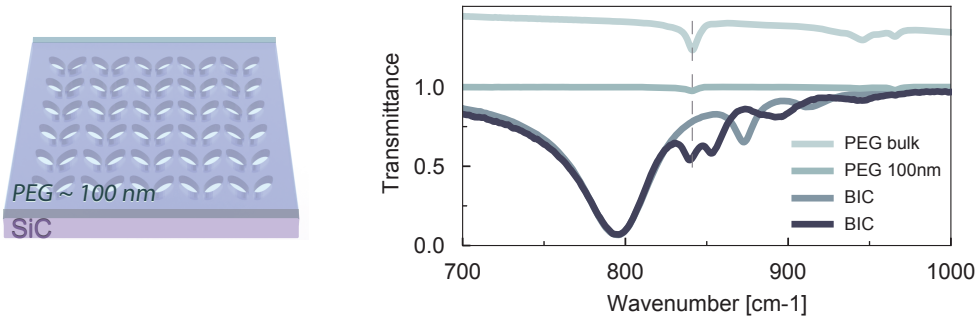

Figure 4.22: Vibrational strong coupling in between the metasurface and PEG.The bulk PEG has an absorption band at approximately 841 cm^{-1} (dashed line) that falls into SiC Reststrahlen band, and the metasurface shows BIC resonance at 870 cm^{-1}. After coupling, BIC peak red-shifted and exhibited vibrational coupling.

To achieve strong vibrational coupling, we utilized the SiC Babinet metasurface platform and tuned its BIC resonance with the target molecule, polyethylene glycol (PEG). To observe the strong-coupling behavior, it is necessary for the target molecule to have an absorption band within the Reststrahlen band of BIC. Figure 4.22 shows the results of our proof-of-concept study where a SiC Babinet BIC metasurface was used for vibrational strong-coupling enabled IR sensing of the target molecule, PEG. The absorption

band of PEG was found to be at approximately 841 cm^{-1} when measured in bulk. To account for possible resonance shifts due to changes in refractive index, we selected a BIC metasurface that exhibits a resonance around 870 cm^{-1} as the proof-of-concept structure. A 100 nm thick layer of PEG was then spin-coated onto the metasurface and analyzed via FTIR transmission measurements. The results revealed that the BIC peak shifted towards the red end of the spectrum and exhibited vibrational coupling with the molecular spectra. These findings demonstrate the potential of the SiC Babinet BIC metasurface for strong-coupling enabled IR sensing applications.

The vibrational strong coupling is evaluated with two criteria (see A in Appendix):

$$\begin{aligned} c_1 &= \omega_R/(\gamma_B IC + \gamma_P EG) > 1 \\ c_2 &= g/\sqrt{(\gamma_B IC^2 + \gamma_P EG^2/2)} > 1. \end{aligned} \tag{4.12}$$

This analysis yield c_1= 1.01, and c_1= 1.01, respectively. Exceeding the required conditions marginally we have demonstrated the SiC Babinet BIC metasurface indeed reaches the strong coupling regime. Our demonstration of the SiC Babinet BIC metasurface for strong-coupling enabled IR sensing has exceeded the required conditions by a slight margin, which bodes well for its potential practical application. The ability to achieve strong coupling between the molecular vibrations and the electromagnetic field from this proof-of-concept study demonstrated the potential in observing Rabi splitting across the signature molecular absorption fingerprint wavelength. The follow-up study with BIC structures various scaling factors of which their resonances cover the full range of molecular absorption wavelengths within the Reststrahlen band will be carried out based on the findings in this chapter.

4.4 Conclusion

In conclusion, the SPhPs meditated topological charge manipulation was realized through carefully designed sub-diffraction nanostructures. Section 4.2 have demonstrated the generation and precise control of highly pure SPhP vortices with high topological order in SiC suspended membranes using transmission sSNOM. Our findings highlight the strong sublinear SPhP dispersion that can be leveraged to obtain vortices with different topological orders by a small increase in the incident frequency. The SiC membranes used in our study are commercially available and can be obtained through CMOS-compatible fabrication, making our results particularly relevant for mid-IR technologies.

We have also introduced a suitable set of reference functions to quantitatively evaluate

the SPhP vortex purity and investigated high OAM states with $|\ell|$ up to 20, as well as the coexistence of multiple OAM states for high order vortices. Our study has paved the way for applications in structured thermal emission and explorations of dipolar-forbidden transitions by highly confined electromagnetic fields carrying OAM.

Furthermore, Section 4.3 the potential of SiC Babinet BIC metasurfaces as a promising platform for strong-coupling enabled IR sensing. The precise tuning of the resonance frequency to match the vibrational frequency of the target molecule offers greater selectivity and sensitivity over other detection methods. By carefully designing the metasurface structure and selecting the appropriate materials, it is possible to achieve strong coupling over a broad range of frequencies and with a wide range of target molecules. Our findings could lead to the development of highly sensitive and selective detection platforms for a wide range of applications, including biomedical sensing, environmental monitoring, and chemical analysis.

Chapter 5

Conclusions and perspectives

The main objective of this thesis is to investigate different aspects of sub-diffraction nanostructures and their optical characteristics, with a particular focus on materials with negative permittivity. The study will delve into their unique ability to support surface polaritons, which can be exploited to manipulate light at a sub-diffraction scale. The research will explore the fabrication techniques of these nanostructures and the impact of their geometries and compositions on their optical properties.

Through a systematic study of these nanostructures, ie., Ag, Au, and SiC, the thesis aims to provide a comprehensive understanding of their optical properties and behavior, including their near-field and far-field responses. To achieve this, experimental techniques such as dark-field spectroscopy, surface-enhanced Raman spectroscopy, and Fourier transform infrared spectroscopy, and scanning near-field optical microscopy were employed to obtain detailed insights into the structure and optical properties of these nanostructures.

Chapter 3 of the thesis explores the role of sub-diffraction antennae in photocatalysis in the visible region. In Section 3.3, the impact of specific ion effects, particularly Ca^{2+} and Mg^{2+}, in the plasmon-assisted dehalogenation of Br-Ade to Ade is investigated. The study shows that CID is the primary electron transfer mechanism driving the dehalogenation of Br-Ade in the presence of Ca^{2+} ions, while Landau damping is the main electron transfer mechanism in the absence of Ca^{2+} ions. In Section 3.4, the role of interparticle hot-spots in plasmon-mediated photocatalytic reactions is evaluated experimentally and theoretically. The results show that the reaction rate follows first-order kinetics and is dependent on the local-field intensity, which increases with decreasing interparticle distances. The study confirms that the overall reaction is predominantly governed by the hot-electrons generated at the gaps, and decreasing the gap size by 10 nm improves the reaction rate by more than 2-folds. The study also highlights the importance of considering connected physical-chemistry aspects of the surface-molecule interaction, such as Hofmeister effects,

to achieve a comprehensive understanding of plasmonic chemistry. The findings provide valuable insights for engineering photocatalytic platforms and offer opportunities to engineer reaction-specific hot-spots, enabling site-specific multiplexing capabilities for the plasmonic nanoreactors.

To further expand the wavelength of interest, manipulation of topological charges in the Mid IR to IR region that is supported by SPhPs was explored in Chapter 4. Specifically, it has been demonstrated that the generation and precise control of highly pure SPhP vortices with high topological order in SiC suspended membranes using transmission sSNOM. Our findings highlight the strong sublinear SPhP dispersion that can be leveraged to obtain vortices with different topological orders by a small increase in the incident frequency. Furthermore, we report SPhPs BIC metasurface for the first time and its unique polarizability was demonstrated. We also demonstrated strong vibrational coupling in between the SiC BIC and PEG molecules as a proof-of-concept study. Our findings suggest that through meticulous design of the metasurface structure and strategic material selection that it is feasible to achieve robust coupling across a wide spectrum of frequencies and with various target molecules. This discovery implies for advancing the potential enhanced IR reflection or absorption spectroscopy with SiC Babinet BIC metasurfaces.

The results obtained from this research have implications for the development of novel optical devices and technologies that can achieve enhanced sensitivity, precision, and control. The understanding gained from this research has the potential to inform the design and optimization of optical components for specific applications. In addition, the research findings may contribute to the development of new techniques for chemical analysis and sensing, which can have far-reaching implications in fields such as healthcare, environmental monitoring, and materials science.

Appendix A

Supplementary Information

Fabrication methods

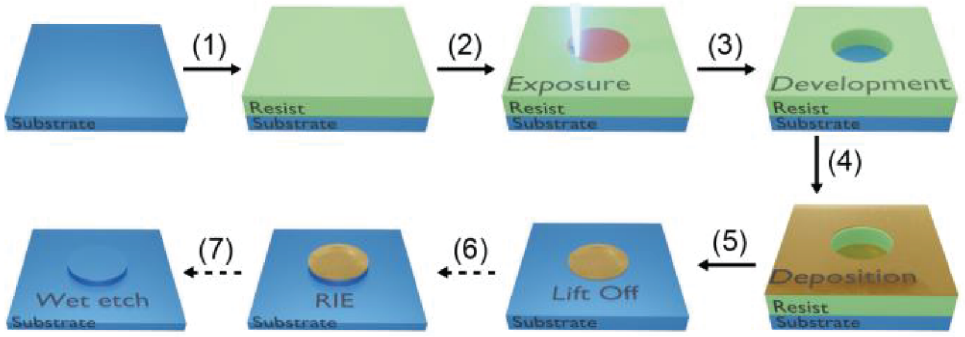

Figure A.1: Schematic that shows a general top-down fabrication process. (1) A thin layer of an electron sensitive resist (in green) is spin-coated onto the substrate (in blue). (2) Selective regions of the photoresist are exposed to a focused electron beam. The electron sensitive resist undergoes chemical changes (in red) upon exposure and can partially be dissolved afterward, that is, the development (3). (4) The desired material (in yellow) is deposited using thermal or electron beam evaporation covering substrate and resist. (5) The residual, undesired polymer covered with material is dissolved during lift off leading to the desired nanostructure on the substrate. (6) Optionally, the deposited material can be used as a hard mask for reactive ion etching (RIE), which removes material from the unprotected regions together with a final wet etch (7) of the hard mask [10].

The samples mentioned in Sections 3.4, 4.2, and 4.3 are fabricated following the top-down processes. The spirals in Section 4.2 was fabricated by following the steps (1)-(5) from Figure A.1. The Au rod dimers in Section 3.4 are fabricated with overlay alignment method by precisely placing the left rod next to the already fabricated right rod to guarantee the spatial accuracy and reporducibilty. The precision of the alignment was ensured using

the 4-point marker system. The dimers are shown in Figure A.3. The Babinet structures from section 4.3 are fabricated following steps (1) through (7) from Figure A.1. The only difference is that the polymer masks are realized with the negative-toned e-beam resist other than the positive toned variation that is depicted in the figure. Figure A.2 shows the various samples that the author has fabricated during their study.

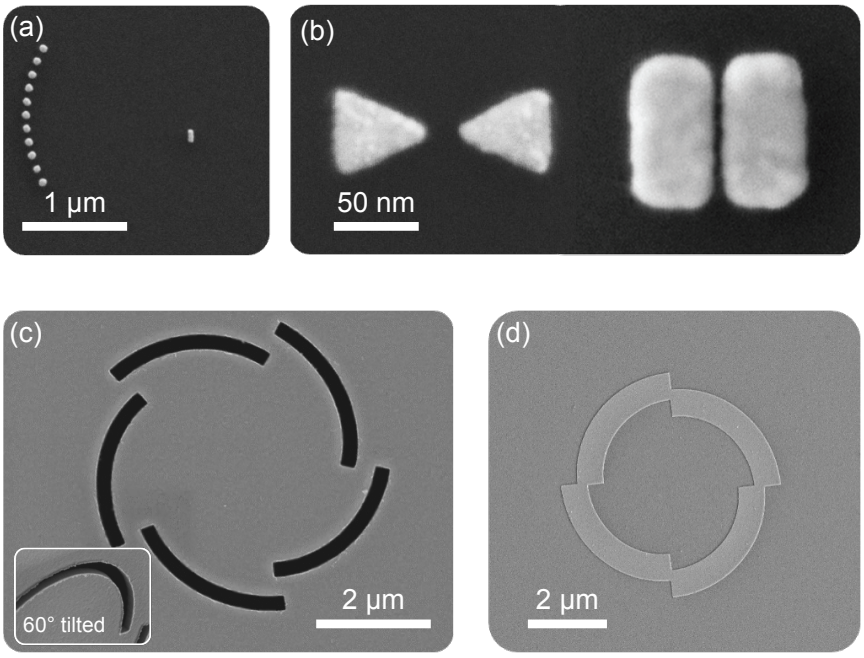

Figure A.2: (a) Au arrays and antenna for hypersonic focusing, (b) Au antennae dimers fabricated for SERS, and (c) negative and positive spiral ridges that on suspended SiC membranes for topological vortex generation. The positive ridges are made of 20 nm thick Cr.

Figure A.3: SEM images for the dimers with gap size 5m 10, 20, and 30 nm.

Complete and simplified coupled oscillator models for strong coupling

Temporal coupled mode theory (TCMT) is an effective method for characterizing the behavior of resonances in open cavities, including their coupling properties to the far-field and other modes. It provides a comprehensive framework for understanding the dynamics of cavity modes and their interaction with input and output port as shown in FigureA.4 [236, 237]. In our study of the molecule-BIC metasurface system, we employ a model that utilizes ports to accurately describe the behavior of transmitted and reflected waves. The system is excited by external fields through port 1, represented as $\mathbf{s}_+ = (s_{1+}, 0)^T$, which are subsequently affected by the metasurface described by the scattering matrix $\mathbf{S}$. The resulting output fields decay through both ports 1 and 2 with equal proportion due to mirror symmetry, represented as $\mathbf{s}_- = (s_{1-}, s_{2-})^T$.

The external fields are transmitted and reflected by the metasurface, with the resulting fields at the output ports given by

$$\boldsymbol{S}_- = S\boldsymbol{s}_+. \tag{A.1}$$

The symmetric 2x2 matrix for the scattering in two-port system is given by

$$\mathbf{S} = \begin{pmatrix} s_{11} & s_{12} \\ s_{12} & s_{22} \end{pmatrix} = C + K[i(\omega I - \Omega) + \Gamma]^{-1} K^T. \tag{A.2}$$

We can assign the S-parameters $s_{11} = s_{1-}/s_{1+} = r$ to the reflection coefficient and

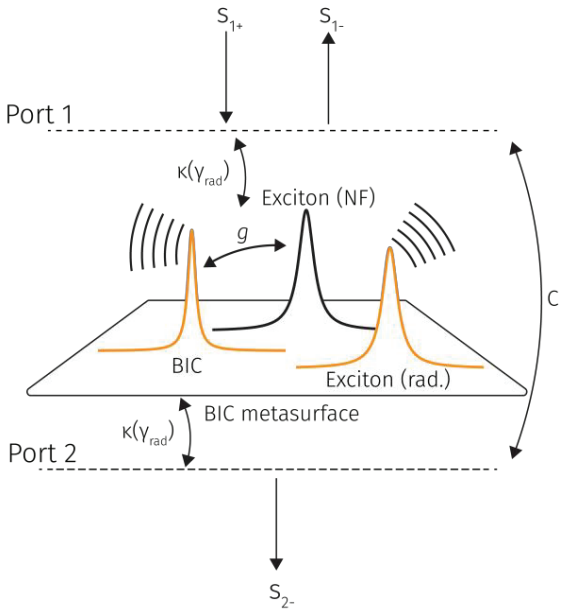

Figure A.4: Schematic representation of TCMT model used in this study. The model consists of a two-port system with three resonances: a BIC and two excitons to describe the near-field coupling and radiative contributions. The metasurface is excited via an incident field ($\mathbf{s}_+ = (s_{1+}, 0)^T$) and allows for reflected ($\mathbf{s}_- = (s_{1-}, s_{2-})^T$) and transmitted waves. The near-field coupling between BIC and the exciton is described by the coupling parameter g, while the far-field coupling is described by the parameter κ, which is a function of the radiative damping rate of the respective resonance. The direct port coupling is addressed via the parameter C [236].

$s_{21} = s_{2-}/s_{1+} = t$ to the transmission coefficient. The modes of the cavity have resonance frequencies and intrinsic damping rates given by Ω, and radiative damping rates given by Γ. The coupling between the ports and the cavity is described by K, which is a function of the radiative damping rates. The unitary matrix C describes the direct port-port crosstalk.

From the transmittance spectra obtained through experiments and simulations, a distinct three-dip feature is observed, indicative of strong-coupling. This feature comprises the coupled BIC-molecule polariton and the radiative parts of the exciton that do not participate in the coupling process. Thus, we can describe the system effectively using a cavity that supports three resonant modes (BIC and a two-fold contribution of the molecule). One part of the molecule interacts only with the BIC in the near-field via the coupling strength g, while the other part interacts only with the radiative far-field via the

term $\sqrt{\gamma_{\mathrm{BIC,rad}}\gamma_{\mathrm{mol,rad}}}$. The complete set of parameters is given by the following:

$$\Omega = \begin{pmatrix} \omega_{BIC} + i\gamma_{BIC,int} & g & 0 \\ g & \omega_{mol} + i\gamma_{mol,int} & 0 \\ 0 & 0 & \omega_{mol} + i\gamma_{mol,int} \end{pmatrix} \tag{A.3}$$

$$\Gamma = \begin{pmatrix} \gamma_{BIC,rad} & 0 & \sqrt{\gamma_{BIC,rad}\gamma_{mol,rad}} \\ g & 0 & 0 \\ \sqrt{\gamma_{BIC,rad}\gamma_{mol,rad}} & 0 & \gamma_{mol,rad} \end{pmatrix} \tag{A.4}$$

$$K = \begin{pmatrix} \sqrt{\gamma_{BIC,rad}} & 0 & \sqrt{\gamma_{mol,rad}} \\ \sqrt{\gamma_{BIC,rad}} & 0 & \sqrt{\gamma_{mol,rad}} \end{pmatrix} \tag{A.5}$$

$$C = e^{i\phi} \begin{pmatrix} r_0 & it_0 \\ it_0 & r_0 \end{pmatrix} \tag{A.6}$$

We can use a single spectrum to extract the coupling strength, but this method is limited to simplified materials with Lorentz-type oscillators, meaning there are no dispersive losses due to inter-band absorption. However, we can simplify the TCMT model into an eigenvalue problem, which we can use to fit the polariton branch dispersion in the main text. To do this, we can combine the radiative and intrinsic damping rates into a total damping rate of $\gamma_i = \gamma_{i,rad} + \gamma_{i,int}$. This gives us the following expression:

$$\begin{pmatrix} \omega_{BIC} + i\gamma_{BIC} & g \\ g & \omega_{mol} + i\gamma_{mol} \end{pmatrix} \boldsymbol{\nu} = \omega_{\pm}\nu. \tag{A.7}$$

We can express the resonance positions of the upper and lower polariton branches as $\omega_{\pm}$ and the Hopfield coefficients, which describe the proportions of BIC and exciton in the hybrid mode, as a matrix ν. The well-known polariton dispersion relation can be retrieved by solving the Eigenvalue problem

$$\omega_{\pm} = \frac{\omega_{BIC} + \omega_{mol}}{2} + \frac{i(\gamma_{BIC} + \gamma_{mol})}{2} \pm \sqrt{g^2 - \frac{1}{4}(\gamma_{BIC} - \gamma_{mol}) + i(\omega_{BIC} - \omega_{mol})^2}. \tag{A.8}$$

The coupling strength g can be fitted from experimental results using the polariton dispersion relation. The Rabi splitting Ω_R is defined as the minimal polariton splitting $\Delta\omega = \omega_+ - \omega_-$, i.e., when $\omega_{BIC} = \omega_{mol}$. Finally we get

$$\Omega_R = 2\sqrt{g^2 - \frac{(\gamma_{BIC} - \gamma_{mol})^2}{4}} \tag{A.9}$$

Appendix B

Publisher permission

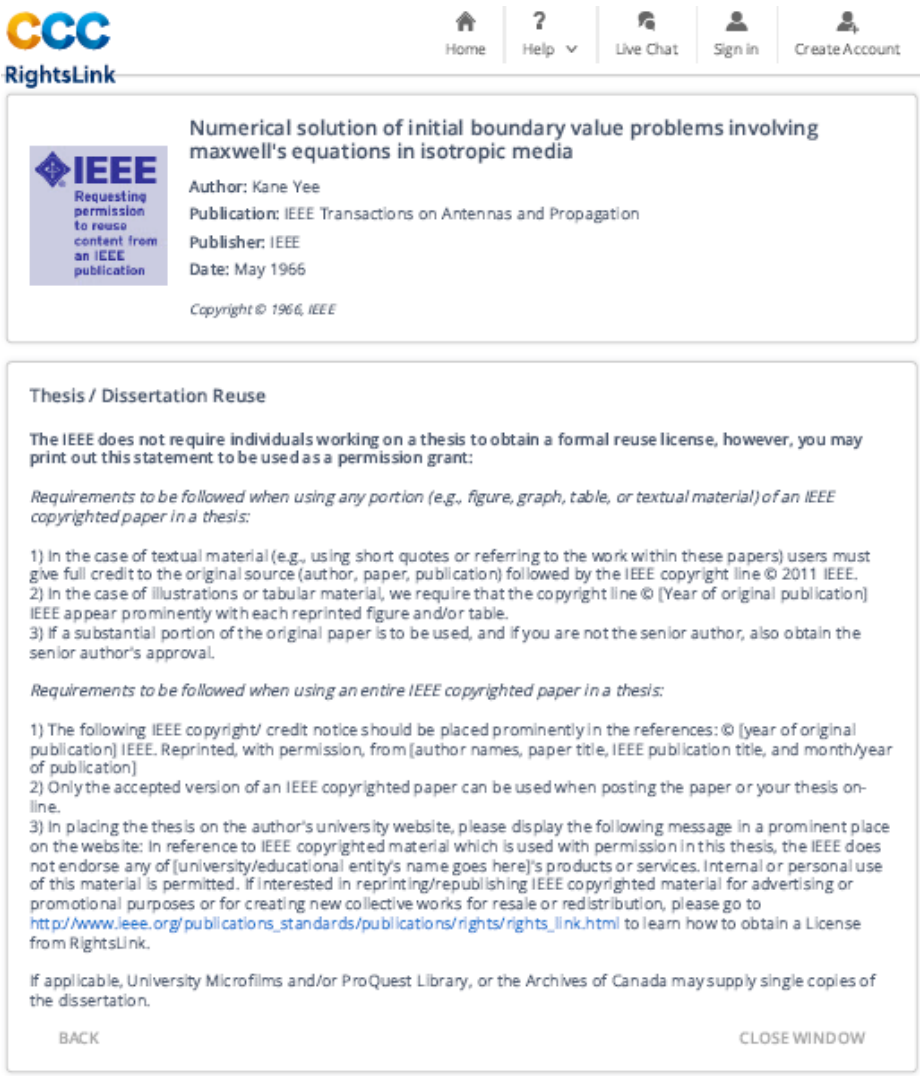

CCC RightsLink

Home | Help | Live Chat | Sign in | Create Account

IEEE Requesting permission to reuse content from an IEEE publication

Numerical solution of initial boundary value problems involving maxwell's equations in isotropic media

Author: Kane Yee

Publication: IEEE Transactions on Antennas and Propagation

Publisher: IEEE

Date: May 1966

Copyright © 1966, IEEE

Thesis / Dissertation Reuse

The IEEE does not require individuals working on a thesis to obtain a formal reuse license, however, you may print out this statement to be used as a permission grant:

Requirements to be followed when using any portion (e.g., figure, graph, table, or textual material) of an IEEE copyrighted paper in a thesis:

1) In the case of textual material (e.g., using short quotes or referring to the work within these papers) users must give full credit to the original source (author, paper, publication) followed by the IEEE copyright line © 2011 IEEE.
2) In the case of illustrations or tabular material, we require that the copyright line © [Year of original publication] IEEE appear prominently with each reprinted figure and/or table.
3) If a substantial portion of the original paper is to be used, and if you are not the senior author, also obtain the senior author's approval.

Requirements to be followed when using an entire IEEE copyrighted paper in a thesis:

1) The following IEEE copyright/ credit notice should be placed prominently in the references: © [year of original publication] IEEE. Reprinted, with permission, from [author names, paper title, IEEE publication title, and month/year of publication]
2) Only the accepted version of an IEEE copyrighted paper can be used when posting the paper or your thesis on-line.
3) In placing the thesis on the author's university website, please display the following message in a prominent place on the website: In reference to IEEE copyrighted material which is used with permission in this thesis, the IEEE does not endorse any of [university/educational entity's name goes here]'s products or services. Internal or personal use of this material is permitted. If interested in reprinting/republishing IEEE copyrighted material for advertising or promotional purposes or for creating new collective works for resale or redistribution, please go to http://www.ieee.org/publications_standards/publications/rights/rights_link.html to learn how to obtain a License from RightsLink.

If applicable, University Microfilms and/or ProQuest Library, or the Archives of Canada may supply single copies of the dissertation.

BACK CLOSE WINDOW

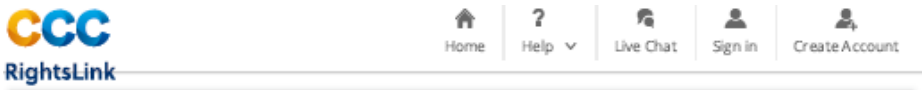

ACS Publications
Most Trusted. Most Cited. Most Read.

Investigating Plasmonic Catalysis Kinetics on Hot-Spot Engineered Nanoantennae

Author: Lin Nan, Jesús Giráldez-Martínez, Andrei Stefancu, et al
Publication: Nano Letters
Publisher: American Chemical Society
Date: Apr 1, 2023

PERMISSION/LICENSE IS GRANTED FOR YOUR ORDER AT NO CHARGE

This type of permission/license, instead of the standard Terms and Conditions, is sent to you because no fee is being charged for your order. Please note the following:

- Permission is granted for your request in both print and electronic formats, and translations.
- If figures and/or tables were requested, they may be adapted or used in part.
- Please print this page for your records and send a copy of it to your publisher/graduate school.
- Appropriate credit for the requested material should be given as follows: "Reprinted (adapted) with permission from {COMPLETE REFERENCE CITATION}. Copyright {YEAR} American Chemical Society." Insert appropriate information in place of the capitalized words.
- One-time permission is granted only for the use specified in your RightsLink request. No additional uses are granted (such as derivative works or other editions). For any uses, please submit a new request.

If credit is given to another source for the material you requested from RightsLink, permission must be obtained from that source.

BACK CLOSE WINDOW

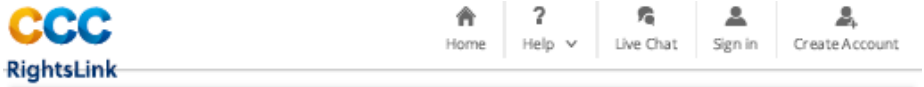

ACS Publications
Most Trusted. Most Cited. Most Read.

Near-Field Retrieval of the Surface Phonon Polariton Dispersion in Free-Standing Silicon Carbide Thin Films

Author: Andrea Mancini, Lin Nan, Fedja J. Wendisch, et al
Publication: ACS Photonics
Publisher: American Chemical Society
Date: Nov 1, 2022

PERMISSION/LICENSE IS GRANTED FOR YOUR ORDER AT NO CHARGE

This type of permission/license, instead of the standard Terms and Conditions, is sent to you because no fee is being charged for your order. Please note the following:

- Permission is granted for your request in both print and electronic formats, and translations.
- If figures and/or tables were requested, they may be adapted or used in part.
- Please print this page for your records and send a copy of it to your publisher/graduate school.
- Appropriate credit for the requested material should be given as follows: "Reprinted (adapted) with permission from {COMPLETE REFERENCE CITATION}. Copyright {YEAR} American Chemical Society." Insert appropriate information in place of the capitalized words.
- One-time permission is granted only for the use specified in your RightsLink request. No additional uses are granted (such as derivative works or other editions). For any uses, please submit a new request.

If credit is given to another source for the material you requested from RightsLink, permission must be obtained from that source.

BACK CLOSE WINDOW

Bibliography

[1] "Beiträge zur Theorie des Mikroskops und der mikroskopischen Wahrnehmung: II. Die dioptrischen Bedingungen der Leistung des Mikroskops," *Archiv für mikroskopische Anatomie*, vol. 9, no. 1, pp. 418–440, 1873.

[2] S. Dunst and P. Tomancak, "Imaging flies by fluorescence microscopy: Principles, technologies, and applications," *Genetics*, vol. 211, no. 1, pp. 15–34, 2019.

[3] V. G. Veselago, "The electrodynamics of substances with simultaneously negative values of and ," *Soviet Physics Uspekhi*, vol. 10, p. 509, apr 1968.

[4] A. Boltasseva and H. A. Atwater, "Low-loss plasmonic metamaterials," *Science*, vol. 331, no. 6015, pp. 290–291, 2011.

[5] J. D. Caldwell, L. Lindsay, V. Giannini, I. Vurgaftman, T. L. Reinecke, S. A. Maier, and O. J. Glembocki, "Low-loss, infrared and terahertz nanophotonics using surface phonon polaritons," *Nanophotonics*, vol. 4, no. 1, pp. 44–68, 2015.

[6] G. Hu, J. Shen, C.-W. Qiu, A. Alù, and S. Dai, "Phonon polaritons and hyperbolic response in van der waals materials," *Advanced Optical Materials*, vol. 8, no. 5, p. 1901393, 2020.

[7] N. W. Ashcroft and N. D. Mermin, *Solid state physics*. Cengage Learning, 2022.

[8] F. J. Garcia de Abajo, "Graphene plasmonics: challenges and opportunities," *Acs Photonics*, vol. 1, no. 3, pp. 135–152, 2014.

[9] M. Fox, *Optical properties of solids*. American Association of Physics Teachers, 2002.

[10] E. Cortés, F. J. Wendisch, L. Sortino, A. Mancini, S. Ezendam, S. Saris, L. de S. Menezes, A. Tittl, H. Ren, and S. A. Maier, "Optical metasurfaces for energy conversion," *Chemical Reviews*, vol. 122, no. 19, pp. 15082–15176, 2022. PMID: 35728004.

[11] W. X. Tang, H. C. Zhang, H. F. Ma, W. X. Jiang, and T. J. Cui, "Concept, theory, design, and applications of spoof surface plasmon polaritons at microwave frequencies," *Advanced Optical Materials*, vol. 7, no. 1, p. 1800421, 2019.

[12] L. Novotny, "Effective wavelength scaling for optical antennas," *Physical review letters*, vol. 98, no. 26, p. 266802, 2007.

[13] K. L. Kelly, E. Coronado, L. L. Zhao, and G. C. Schatz, "The optical properties of metal nanoparticles: the influence of size, shape, and dielectric environment," *The Journal of Physical Chemistry B*, vol. 107, no. 3, pp. 668–677, 2003.

[14] T. Taliercio and P. Biagioni, "Semiconductor infrared plasmonics," *Nanophotonics*, vol. 8, no. 6, pp. 949–990, 2019.

[15] A. Mancini, C. R. Gubbin, R. Berté, F. Martini, A. Politi, E. Cortés, Y. Li, S. De Liberato, and S. A. Maier, "Near-field spectroscopy of cylindrical phonon-polariton antennas," *ACS Nano*, vol. 14, no. 7, pp. 8508–8517, 2020.

[16] J. B. Khurgin, "Relative merits of phononics vs. plasmonics: the energy balance approach," *Nanophotonics*, vol. 7, no. 1, pp. 305–316, 2018.

[17] K. N. Fish, "Total internal reflection fluorescence (tirf) microscopy," *Current protocols in cytometry*, vol. 50, no. 1, pp. 12–18, 2009.

[18] S. A. Maier, *Plasmonics: fundamentals and applications*. Springer, 2007.

[19] D. Aurelio and M. Liscidini, "Electromagnetic field enhancement in bloch surface waves," *Physical Review B*, vol. 96, no. 4, p. 045308, 2017.

[20] J. B. Khurgin, "How to deal with the loss in plasmonics and metamaterials," *Nature nanotechnology*, vol. 10, no. 1, pp. 2–6, 2015.

[21] Y. Kane, "Numerical solution of initial boundary value problems involving maxwell's equations in isotropic media," *IEEE Transactions on Antennas and Propagation*, vol. 14, no. 3, pp. 302–307, 1966.

[22] J.-M. Jin, *The finite element method in electromagnetics*. John Wiley & Sons, 2015.

[23] A. Cheriet, A. Zaoui, M. Feliachi, and S. M. Mimoune, "Computational performance comparison between fvm and fem for 3d magnetostatic problems," 2013.

[24] J. D. Jackson, *Classical Electrodynamics*. John Wiley & Sons, Inc., 3rd ed., 1999.

[25] F. Hao, P. Nordlander, Y. Sonnefraud, P. V. Dorpe, and S. A. Maier, "Tunability of subradiant dipolar and fano-type plasmon resonances in metallic ring/disk cavities: Implications for nanoscale optical sensing," *ACS nano*, vol. 3, no. 3, pp. 643–652, 2009.

[26] Y. Sonnefraud, N. Verellen, H. Sobhani, G. A. Vandenbosch, V. V. Moshchalkov, P. Van Dorpe, P. Nordlander, and S. A. Maier, "Experimental realization of subradiant, superradiant, and fano resonances in ring/disk plasmonic nanocavities," *ACS nano*, vol. 4, no. 3, pp. 1664–1670, 2010.

[27] M. Gross and S. Haroche, "Superradiance: an essay on the theory of collective spontaneous emission," *Physics reports*, vol. 93, no. 5, pp. 301–396, 1982.

[28] G. Grynberg, A. Aspect, and C. Fabre, *Introduction to Quantum Optics: From the Semi-Classical Approach to Quantized Light*. Cambridge, UK: Cambridge University Press, 2010.

[29] J. Cambiasso, *Light-matter interactions in lossy and lossless media*. PhD thesis, Imperial College London, London, July 2017.

[30] M. Born and E. Wolf, *Principles of optics: electromagnetic theory of propagation, interference and diffraction of light*. Cambridge University Press, 7th expanded ed., 1999.

[31] J. A. Fan, K. Bao, J. B. Lassiter, J. Bao, N. J. Halas, P. Nordlander, and F. Capasso, "Near-normal incidence dark-field microscopy: applications to nanoplasmonic spectroscopy," *Nano letters*, vol. 12, no. 6, pp. 2817–2821, 2012.

[32] K. Kneipp, Y. Wang, H. Kneipp, L. T. Perelman, I. Itzkan, R. R. Dasari, and M. S. Feld, "Single molecule detection using surface-enhanced raman scattering (sers)," *Physical Review Letters*, vol. 78, no. 9, p. 1667, 1997.

[33] M. Moskovits, "Surface-enhanced spectroscopy," *Reviews of Modern Physics*, vol. 57, no. 3, p. 783, 1985.

[34] E. C. Le Ru and P. G. Etchegoin, "Surface enhanced raman scattering enhancement factors: A comprehensive study," *The Journal of Physical Chemistry C*, vol. 111, no. 37, pp. 13794–13803, 2007.

[35] S. Ezendam, M. Herran, L. Nan, C. Gruber, Y. Kang, F. Gröbmeyer, R. Lin, J. Gargiulo, A. Sousa-Castillo, and E. Cortés, "Hybrid plasmonic nanomaterials for hydro-

gen generation and carbon dioxide reduction," *ACS Energy Letters*, vol. 7, no. 2, pp. 778–815, 2022.

[36] A. G. Brolo, R. Gordon, B. Leathem, and K. L. Kavanagh, "Surface plasmon sensor based on the enhanced light transmission through arrays of nanoholes in gold films," *Langmuir: the ACS journal of surfaces and colloids*, vol. 20, no. 17, pp. 4813–4815, 2004.

[37] J. N. Anker, W. P. Hall, O. Lyandres, N. C. Shah, J. Zhao, and R. P. Van Duyne, "Biosensing with plasmonic nanosensors," *Nature materials*, vol. 7, no. 6, pp. 442–453, 2008.

[38] V. Giannini, A. I. Fernández-Domínguez, S. C. Heck, and S. A. Maier, "Plasmonic nanoantennas: Fundamentals and their use in controlling the radiative properties of nanoemitters," *Chemical Reviews*, vol. 111, no. 6, pp. 3888–3912, 2011.

[39] C. Clavero, "Plasmon-induced hot-electron generation at nanoparticle/metal-oxide interfaces for photovoltaic and photocatalytic devices," *Nature Photonics*, vol. 8, no. 2, p. 95, 2014.

[40] V. Giannini, J. Sanchez-Gil, O. Muskens, and J. Rivas, "Electrodynamic calculations of spontaneous emission coupled to metal nanostructures of arbitrary shape: Nanoantenna-enhanced fluorescence," *Journal of the Optical Society of America B-Optical Physics*, vol. 26, no. 8, pp. 1569–1577, 2009.

[41] N. Lindquist, P. Nagpal, K. McPeak, D. Norris, and S.-H. Oh, "Engineering metallic nanostructures for plasmonics and nanophotonics," *Reports on Progress in Physics*, vol. 75, no. 3, p. 036501, 2012.

[42] W. Murray and W. Barnes, "Plasmonic materials," *Advanced Materials*, vol. 19, no. 22, pp. 3771–3782, 2007.

[43] T. Serdiuk, S. Alekseev, V. Lysenko, V. Skryshevsky, and A. Geloen, "Charge-driven selective localization of fluorescent nanoparticles in live cells," *Nanotechnology*, vol. 23, no. 31, p. 315101, 2012.

[44] C. Sönnichsen, T. Franzl, T. Wilk, G. von Plessen, J. Feldmann, O. Wilson, and P. Mulvaney, "Drastic reduction of plasmon damping in gold nanorods," *Physical Review Letters*, vol. 88, no. 7, p. 077402, 2002.

[45] M. L. Brongersma, N. J. Halas, and P. Nordlander, "Plasmon-induced hot carrier science and technology," *Nature Nanotechnology*, vol. 10, no. 1, pp. 25–34, 2015.

[46] P. Narang, R. Sundararaman, A. S. Jermyn, W. A. Goddard III, and H. A. Atwater, "Cubic nonlinearity driven up-conversion in high-field plasmonic hot carrier systems," *The Journal of Physical Chemistry C*, vol. 120, no. 39, pp. 21940–21948, 2016.

[47] Z. Jacob and V. M. Shalaev, "Plasmonics goes quantum," *Science*, vol. 334, no. 6055, pp. 463–464, 2011.

[48] M. S. Tame, K. R. McEnery, E. K. İzdelek, J. Lee, S. A. Maier, and M. S. Kim, "Quantum plasmonics," *Nature Physics*, vol. 9, no. 6, pp. 329–340, 2013.

[49] A. M. Brown, R. Sundararaman, P. Narang, W. A. Goddard III, and H. A. Atwater, "Nonradiative plasmon decay and hot carrier dynamics: Effects of phonons, surfaces, and geometry," *ACS nano*, vol. 10, no. 1, pp. 957–966, 2016.

[50] R. Sundararaman, P. Narang, A. S. Jermyn, W. A. Goddard, and H. A. Atwater, "Theoretical predictions for hot-carrier generation from surface plasmon decay," *Nature Communications*, vol. 5, 2014.

[51] J. B. Khurgin, "How to deal with the loss in plasmonics and metamaterials," *Nature Nanotechnology*, vol. 10, no. 1, pp. 2–6, 2015.

[52] S. Linic, U. Aslam, C. Boerigter, and M. Morabito, "Photochemical transformations on plasmonic metal nanoparticles," *Nature Materials*, vol. 14, no. 6, pp. 567–576, 2015.

[53] F. Ladstadter, U. Hohenester, P. Puschnig, and C. Ambrosch-Draxl, "First-principles calculation of hot-electron scattering in metals," *Physical Review B-Condensed Matter and Materials Physics*, vol. 70, no. 23, p. 235119, 2004.

[54] M. Bonn, "Phonon-versus electron-mediated desorption and oxidation of co on ru(0001)," *Science*, vol. 285, no. 5430, pp. 1042–1045, 1999.

[55] P. Christopher, H. Xin, A. Marimuthu, and S. Linic, "Singular characteristics and unique chemical bond activation mechanisms of photocatalytic reactions on plasmonic nanostructures," *Nature materials*, vol. 11, no. 12, pp. 1044–1050, 2012.

[56] P. Christopher, H. Xin, and S. Linic, "Visible-light-enhanced catalytic oxidation reactions on plasmonic silver nanostructures," *Nature Chemistry*, vol. 3, no. 6, pp. 467–472, 2011.

[57] H. Zhang and A. O. Govorov, "Optical generation of hot plasmonic carriers in metal nanocrystals: The effects of shape and field enhancement," *Journal of Physical Chemistry C*, vol. 118, no. 14, pp. 7606–7614, 2014.

[58] V. E. Babicheva, S. V. Zhukovsky, R. S. Ikhsanov, I. E. Protsenko, I. V. Smetanin, and A. Uskov, "Hot electron photoemission from plasmonic nanostructures: the role of surface photoemission and transition absorption," *ACS Photonics*, vol. 2, no. 8, pp. 1039–1048, 2015.

[59] S. Linic, P. Christopher, and D. B. Ingram, "Plasmonic-metal nanostructures for efficient conversion of solar to chemical energy," *Nature Materials*, vol. 10, no. 12, pp. 911–921, 2011.

[60] R. Long and O. V. Prezhdo, "Instantaneous generation of charge-separated state on tio2 surface sensitized with plasmonic nanoparticles," *Journal of the American Chemical Society*, vol. 136, no. 11, pp. 4343–4354, 2014.

[61] S. Mubeen, J. Lee, N. Singh, S. Krämer, G. D. Stucky, and M. Moskovits, "An autonomous photosynthetic device in which all charge carriers derive from surface plasmons," *Nature nanotechnology*, vol. 8, no. 4, pp. 247–251, 2013.

[62] C. Ng, J. J. Cadusch, S. Dligatch, A. Roberts, T. J. Davis, P. Mulvaney, and D. E. Gómez, "Hot carrier extraction with plasmonic broadband absorbers," *ACS nano*, p. acsnano.6b01108, 2016.

[63] A. Stefancu, O. M. Biro, I. Todor-Boer, I. Botiz, E. Cortés, and N. Leopold, "Plasmonic nanoantennas for large-area photodetection," *ACS Photonics*, vol. 9, p. 895, 2022.

[64] A. J. Leenheer, P. Narang, N. S. Lewis, and H. A. Atwater, "Plasmonic efficiency enhancement of si solar cells," *Journal of Applied Physics*, vol. 115, p. 134301, 2014.

[65] S. Lee, H. Hwang, W. Lee, D. Schebarchov, Y. Wy, J. Grand, B. Auguié, D. H. Wi, E. Cortés, and S.-W. Han, "Plasmon-induced hot carrier extraction from gold nanoparticles," *ACS Energy Letters*, vol. 5, p. 3881, 2020.

[66] G. V. Hartland, L. V. Besteiro, P. Johns, and A. O. Govorov, "What's so Hot about Electrons in Metal Nanoparticles?," *ACS Energy Letters*, vol. 2, no. 7, pp. 1641–1653, 2017.

[67] B. Foerster, A. Joplin, K. Kaefer, S. Celiksoy, S. Link, and C. Sönnichsen, "Plasmonics in the ultraviolet with the poor metals al, ga, in, sn, tl, pb, and bi," *ACS nano*, vol. 11, no. 3, pp. 2886–2896, 2017.

[68] U. Kreibig and M. Vollmer, *Optical Properties of Metal Clusters*. Berlin: Springer, 1995.

[69] J. B. Khurgin, "How to deal with the loss in plasmonics and metamaterials," *Nature nanotechnology*, vol. 10, no. 1, pp. 2–6, 2015.

[70] J. Gargiulo, R. Berté, Y. Li, S. A. Maier, and E. Cortés, "Gold nanorods as potential nanoplatforms for surface-enhanced raman spectroscopy detection and cancer treatment," *Accounts of chemical research*, vol. 52, no. 9, pp. 2525–2535, 2019.

[71] E. Cortés, L. V. Besteiro, A. Alabastri, A. Baldi, G. Tagliabue, A. Demetriadou, and P. Narang, "Nanoparticles for photothermal therapies," *ACS nano*, vol. 14, no. 12, pp. 16202–16230, 2020.

[72] B. Foerster, V. A. Spata, E. A. Carter, C. Sönnichsen, and S. Link, "Plasmon damping depends on the chemical nature of the nanoparticle interface," *Science Advances*, vol. 5, no. 3, 2019.

[73] S. A. Lee and S. Link, "Plasmon resonances of individual nanoparticles and their characterization with electron energy loss spectroscopy," *Accounts of Chemical Research*, vol. 54, no. 10, pp. 1950–1959, 2021.

[74] E. Oksenberg, I. Shlesinger, A. Xomalis, A. Baldi, J. J. Baumberg, A. F. Koenderink, and E. C. Garnett, "The role of the excitation symmetry in the plasmon-enhanced raman scattering of chiral molecules," *Nature nanotechnology*, vol. 16, no. 11, pp. 1378–1383, 2021.

[75] J. B. Khurgin, A. Petrov, M. Eich, and A. V. Uskov, "Recent advances in optical antennas and metasurfaces for photodetection and energy conversion," *ACS Photonics*, vol. 8, p. 2041, 2021.

[76] B. Persson, "Theory of surface forces," *Surf. Sci.*, vol. 281, p. 153, 1993.

[77] Z. Schultz, "Raman spectroscopy: From fundamental research to real-world applications," *Spectroscopy*, vol. 35, p. 15, 2020.

[78] A. Otto, "Surface-enhanced raman scattering: a new tool for bioanalytical chemistry," *J. Raman Spectrosc.*, vol. 33, p. 593, 2002.

[79] A. Otto, "The 'chemical' (electronic) contribution to surface-enhanced raman scattering," *J. Raman Spectrosc.*, vol. 36, p. 497, 2005.

[80] S.-D. Iancu, A. Stefancu, V. Moisoiu, L. F. Leopold, and N. Leopold, "Structural and optical properties of silver nanoparticles synthesized by laser ablation in liquid," *Beilstein J. Nanotechnol.*, vol. 10, p. 2338, 2019.

[81] N. Leopold, A. Stefancu, K. Herman, I. S. Tódor, S. D. Iancu, V. Moisoiu, and L. F. Leopold, "Graphene oxide functionalization with chitosan for the preparation of conductive and electro-responsive materials," *Beilstein J. Nanotechnol.*, vol. 9, p. 2236, 2018.

[82] A. Stefancu, S. D. Iancu, V. Moisoiu, and N. Leopold, "Effect of ionizing radiation on the properties of polyethylene glycol and polyethylene glycol-based hydrogels," *Rom. Rep. Phys.*, vol. 70, p. 509, 2018.

[83] A. Stefancu, S. D. Iancu, and N. Leopold, "Photocatalytic activity of graphene oxide-based materials: influence of go oxidation degree and light irradiation," *J. Phys. Chem. C*, vol. 125, p. 12802, 2021.

[84] A. Otto, A. Bruckbauer, and Y. X. Chen, "Surface-enhanced raman spectroscopy," *J. Mol. Struct.*, vol. 661–662, p. 501, 2003.

[85] V. Petráková, I. C. Sampaio, and S. Reich, "Hydrophobic effects in water-mediated interactions between gold nanoparticles," *J. Phys. Chem. C*, vol. 123, p. 17498, 2019.

[86] C. Pfeiffer, C. Rehbock, D. Hühn, C. Carrillo-Carrion, D. J. de Aberasturi, V. Merk, S. Barcikowski, and W. J. Parak, "Interaction of colloidal particles with live cells studied by confocal raman microscopy," *Journal of the Royal Society Interface*, vol. 11, p. 20130931, 2014.

[87] T. Oncsik, G. Trefalt, M. Borkovec, and I. Szilagyi, "Effect of sodium chloride on the interaction forces between silica surfaces," *Langmuir*, vol. 31, p. 3799, 2015.

[88] V. Merk, C. Rehbock, F. Becker, U. Hagemann, H. Nienhaus, and S. Barcikowski, "Investigation of cellular uptake and localization of laser-generated copper-sulfide nanoparticles," *Langmuir*, vol. 30, p. 4213, 2014.

[89] S. Kogikoski, A. Dutta, and I. Bald, "Giant photoabsorption cross sections of pbs quantum dots: The role of aggregation and ligand effects," *ACS Nano*, vol. 15, p. 20562, 2021.

[90] A. Dutta, R. Schürmann, S. Kogikoski, N. S. Mueller, S. Reich, and I. Bald, "Light-driven hydrogenation of nitroarenes over gold nanoparticles: Elucidating the role of surface plasmon resonance," *ACS Catalysis*, vol. 11, p. 8370, 2021.

[91] T. S. Marques, M. A. Śmiałek, R. Schürmann, I. Bald, M. Raposo, S. Eden, and N. J. Mason, "Electron attachment and ionization to room temperature ionic liquids

[emim][ntf2] and [bmim][ntf2]," *The European Physical Journal D*, vol. 74, p. 222, 2020.

[92] A. Dutta, R. Schürmann, and I. Bald, "A comprehensive study of electron attachment to ethylene sulfide," *The European Physical Journal D*, vol. 74, p. 19, 2020.

[93] R. Schürmann and I. Bald, "The role of negative ions in astrochemistry," *Nanoscale*, vol. 9, p. 1951, 2017.

[94] J. Liu, Z.-Y. Cai, W.-X. Sun, J.-Z. Wang, X.-R. Shen, C.-G. Zhan, S. Devasenathipathy, J.-Z. Zhou, D.-Y. Wu, B.-W. Mao, and Z.-Q. Tian, "Direct observation of the disappearance of water droplets induced by a laser trigger," *Journal of the American Chemical Society*, vol. 142, p. 17489, 2020.

[95] P. C. Lee and D. Meisel, "Adsorption and surface-enhanced raman of dyes on silver and gold sol," *The Journal of Physical Chemistry*, vol. 86, p. 3391, 1982.

[96] I. Botiz, M.-A. Codescu, C. Farcau, C. Leordean, S. Astilean, C. Silva, and N. Stingelin, "Comparative study of surface-enhanced raman scattering activity of gold and silver nanostructures," *Journal of Materials Chemistry C*, vol. 5, p. 2513, 2017.

[97] C. Farcau, N. M. Sangeetha, H. Moreira, B. Viallet, J. Grisolia, D. Ciuculescu-Pradines, and L. Ressier, "Sers-active nanostructured substrates based on gold films deposited onto nanopatterned polymeric surfaces," *ACS Nano*, vol. 5, p. 7137, 2011.

[98] A. V. Delgado, F. González-Caballero, R. J. Hunter, L. K. Koopal, and J. Lyklema, "Measurement and interpretation of electrokinetic phenomena," *Pure and Applied Chemistry*, vol. 77, p. 1753, 2005.

[99] C. T. Gerold and C. S. Henry, "Sub-10 nm gold nanoparticle arrays via block copolymer lithography with ion milling: Fabrication and characterization," *Langmuir*, vol. 34, p. 1550, 2018.

[100] B. Bera, N. Kumar, M. H. G. Duits, M. A. Cohen Stuart, and F. Mugele, "Reversing the charge on ionic surfactants: Mixed surfactant systems with oppositely charged components," *Langmuir*, vol. 34, no. 45, pp. 13574–13583, 2018.

[101] D. F. Parsons, M. Bostr"om, P. L. Nostro, and B. W. Ninham, "Electrostatic forces between ions at the air/water interface," *Physical Chemistry Chemical Physics*, vol. 13, no. 27, pp. 12352–12357, 2011.

[102] D. F. Parsons, M. Bostr"om, T. J. Maceina, A. Salis, and B. W. Ninham, "Hofmeister anion-specific surface charge density of the air-water interface," *Langmuir*, vol. 26, no. 5, pp. 3323–3328, 2010.

[103] B. W. Ninham, T. T. Duignan, and D. F. Parsons, "The extended hofmeister series: Compounds ordering the water structure controlled by solutes," *Current Opinion in Colloid Interface Science*, vol. 16, no. 6, pp. 612–617, 2011.

[104] K. D. Collins, "Charge density-dependent strength of hydration and biological structure," *Biophysical Chemistry*, vol. 119, p. 271, 2006.

[105] N. G. Tognalli, E. Cortés, A. D. Hernández-Nieves, P. Carro, G. Usaj, C. A. Balseiro, M. E. Vela, R. C. Salvarezza, and A. Fainstein, "Controlling the morphology of gold nanoparticles with poly(ethyleneimine)," *ACS Nano*, vol. 5, p. 5433, 2011.

[106] W. Nam, Y. Zhao, J. Song, S. A. Safiabadi Tali, S. Kang, W. Zhu, H. J. Lezec, A. Agrawal, P. J. Vikesland, and W. Zhou, "Optimization of lspr sensitivity and figure of merit using ag-au nanocuboids for simultaneous detection of two analytes," *Journal of Physical Chemistry Letters*, vol. 11, p. 9543, 2020.

[107] A. S. Z. L. M. L. A. O. G. L. V. B. Lin Nan, Jesus G. Martinez and E. Cortés, "Investigating plasmonic catalysis kinetics on hot-spot engineered nanoantennae," *Nano Letters*.

[108] D. C. Ratchford, "Plasmon-Induced Charge Transfer: Challenges and Outlook," *ACS Nano*, vol. 13, no. 12, pp. 13610–13614, 2019.

[109] W. Xu, J. S. Kong, and P. Chen, "Probing the catalytic activity and heterogeneity of Au-nanoparticles at the single-molecule level," *Physical Chemistry Chemical Physics*, vol. 11, no. 15, pp. 2767–2778, 2009.

[110] J. B. Sambur and P. Chen, "Approaches to single-nanoparticle catalysis," *Annual Review of Physical Chemistry*, vol. 65, pp. 395–422, 2014.

[111] H. Zhang and A. O. Govorov, "Optical generation of hot plasmonic carriers in metal nanocrystals: The effects of shape and field enhancement," *Journal of Physical Chemistry C*, vol. 118, no. 14, pp. 7606–7614, 2014.

[112] E. Y. Santiago, L. V. Besteiro, X. T. Kong, M. A. Correa-Duarte, Z. Wang, and A. O. Govorov, "Efficiency of Hot-Electron Generation in Plasmonic Nanocrystals with Complex Shapes: Surface-Induced Scattering, Hot Spots, and Interband Transitions," *ACS Photonics*, vol. 7, no. 10, pp. 2807–2824, 2020.

[113] L. V. Besteiro, X. T. Kong, Z. Wang, G. Hartland, and A. O. Govorov, "Understanding Hot-Electron Generation and Plasmon Relaxation in Metal Nanocrystals: Quantum and Classical Mechanisms," *ACS Photonics*, vol. 4, no. 11, pp. 2759–2781, 2017.

[114] A. O. Govorov, H. Zhang, and Y. K. Gun'Ko, "Theory of photoinjection of hot plasmonic carriers from metal nanostructures into semiconductors and surface molecules," *Journal of Physical Chemistry C*, vol. 117, no. 32, pp. 16616–16631, 2013.

[115] B. Seemala, A. J. Therrien, M. Lou, K. Li, J. P. Finzel, J. Qi, P. Nordlander, and P. Christopher, "Plasmon-Mediated Catalytic O2 Dissociation on Ag Nanostructures: Hot Electrons or Near Fields?," *ACS Energy Letters*, vol. 4, no. 8, pp. 1803–1809, 2019.

[116] A. Sousa-Castillo, M. Comesaña-Hermo, B. Rodríguez-González, M. Pérez-Lorenzo, Z. Wang, X. T. Kong, A. O. Govorov, and M. A. Correa-Duarte, "Boosting Hot Electron-Driven Photocatalysis through Anisotropic Plasmonic Nanoparticles with Hot Spots in Au-TiO2 Nanoarchitectures," *Journal of Physical Chemistry C*, vol. 120, no. 21, pp. 11690–11699, 2016.

[117] E. Cortés, W. Xie, J. Cambiasso, A. S. Jermyn, R. Sundararaman, P. Narang, S. Schlücker, and S. A. Maier, "Plasmonic hot electron transport drives nano-localized chemistry," *Nature Communications*, vol. 8, p. 14880, 2017.

[118] O. Ávalos-Ovando, E. Y. Santiago, A. Movsesyan, X. T. Kong, P. Yu, L. V. Besteiro, L. K. Khorashad, H. Okamoto, J. M. Slocik, M. A. Correa-Duarte, M. Comesaña-Hermo, T. Liedl, Z. Wang, G. Markovich, S. Burger, and A. O. Govorov, "Chiral Bioinspired Plasmonics: A Paradigm Shift for Optical Activity and Photochemistry," *ACS Photonics*, vol. 9, no. 7, pp. 2219–2236, 2022.

[119] E. Cortés, "Efficiency and Bond Selectivity in Plasmon-Induced Photochemistry," *Advanced Optical Materials*, vol. 5, no. 15, pp. 1–13, 2017.

[120] Y. Zhao, L. Du, H. Li, W. Xie, and J. Chen, "Is the Suzuki-Miyaura Cross-Coupling Reaction in the Presence of Pd Nanoparticles Heterogeneously or Homogeneously Catalyzed? An Interfacial Surface-Enhanced Raman Spectroscopy Study," *Journal of Physical Chemistry Letters*, vol. 10, no. 6, pp. 1286–1291, 2019.

[121] Z. Li, R. Wang, and D. Kurouski, "Nanoscale Photocatalytic Activity of Gold and Gold-Palladium Nanostructures Revealed by Tip-Enhanced Raman Spectroscopy," *Journal of Physical Chemistry Letters*, vol. 11, pp. 5531–5537, jul 2020.

[122] Y. Li, Y. Hu, F. Shi, H. Li, W. Xie, and J. Chen, "C-H Arylation on Nickel Nanoparticles Monitored by In Situ Surface-Enhanced Raman Spectroscopy," *Angewandte Chemie*, vol. 131, pp. 9147–9151, jul 2019.

[123] Z. Tan, Y. Zhang, B. D. Thackray, and J. Ye, "Improvement of surface-enhanced Raman scattering detection and imaging by multivariate curve resolution methods," *Journal of Applied Physics*, vol. 125, may 2019.

[124] Y. Zhao and W. Xie, "SERS detection of heterogeneous reactions at catalytic interfaces using bifunctional metal nanoparticles," *Scientia Sinica Chimica*, vol. 49, no. 5, pp. 801–810, 2019.

[125] F. Sun, D. D. Galvan, P. Jain, and Q. Yu, "Multi-functional, thiophenol-based surface chemistry for surface-enhanced Raman spectroscopy," *Chemical Communications*, vol. 53, no. 33, pp. 4550–4561, 2017.

[126] T. You, X. Liang, Y. Gao, P. Yin, L. Guo, and S. Yang, "A computational study on surface-enhanced Raman spectroscopy of para-substituted Benzenethiol derivatives adsorbed on gold nanoclusters," *Spectrochimica Acta - Part A: Molecular and Biomolecular Spectroscopy*, vol. 152, pp. 278–287, jul 2016.

[127] T. Fujita, Y. Takeuchi, K. Yamaguchi, T. A. Yano, T. Tanaka, and N. Takeyasu, "Comparison of hot carrier generation between self-assembled gold and silver nanoparticle arrays tailored to the same hybrid plasmon resonance," *Journal of Applied Physics*, vol. 128, sep 2020.

[128] P. Jiang, Y. Dong, L. Yang, Y. Zhao, and W. Xie, "Hot Electron-Induced Carbon-Halogen Bond Cleavage Monitored by in Situ Surface-Enhanced Raman Spectroscopy," *Journal of Physical Chemistry C*, vol. 123, no. 27, pp. 16741–16746, 2019.

[129] R. Schürmann, A. Nagel, S. Juergensen, A. Pathak, S. Reich, C. Pacholski, and I. Bald, "Microscopic Understanding of Reaction Rates Observed in Plasmon Chemistry of Nanoparticle-Ligand Systems," *Journal of Physical Chemistry C*, vol. 126, no. 11, pp. 5333–5342, 2022.

[130] Z. Yu and R. R. Frontiera, "Intermolecular Forces Dictate Vibrational Energy Transfer in Plasmonic-Molecule Systems," *ACS Nano*, vol. 16, no. 1, pp. 847–854, 2022.

[131] A. You, M. A. Y. Be, and I. In, "Plasmonic reactivity of halogen thiophenols on gold nanoparticles studied by SERS and studied by SERS and XPS," vol. 031307, 2022.

[132] R. C. Elias and S. Linic, "Elucidating the Roles of Local and Nonlocal Rate Enhancement Mechanisms in Plasmonic Catalysis," *Journal of the American Chemical Society*, 2022.

[133] M. J. Kale, T. Avanesian, and P. Christopher, "Direct photocatalysis by plasmonic nanostructures," *ACS Catalysis*, vol. 4, no. 1, pp. 116–128, 2014.

[134] C. Boerigter, R. Campana, M. Morabito, and S. Linic, "Evidence and implications of direct charge excitation as the dominant mechanism in plasmon-mediated photocatalysis," *Nature Communications*, vol. 7, 2016.

[135] J. D. Caldwell, A. V. Kretinin, Y. Chen, V. Giannini, M. M. Fogler, Y. Francescato, C. T. Ellis, J. G. Tischler, C. R. Woods, A. J. Giles, *et al.*, "Sub-diffractional volume-confined polaritons in the natural hyperbolic material hexagonal boron nitride," *Nat. Commun.*, vol. 5, no. 1, pp. 1–9, 2014.

[136] V. M. Breslin, D. C. Ratchford, A. J. Giles, A. D. Dunkelberger, and J. C. Owrutsky, "Hyperbolic phonon polariton resonances in calcite nanopillars," *Opt. Express*, vol. 29, no. 8, pp. 11760–11772, 2021.

[137] W. Ma, G. Hu, D. Hu, R. Chen, T. Sun, X. Zhang, Q. Dai, Y. Zeng, A. Alù, C.-W. Qiu, *et al.*, "Ghost hyperbolic surface polaritons in bulk anisotropic crystals," *Nature*, vol. 596, no. 7872, pp. 362–366, 2021.

[138] F. H. Feres, R. A. Mayer, L. Wehmeier, F. C. Maia, E. Viana, A. Malachias, H. A. Bechtel, J. M. Klopf, L. M. Eng, S. C. Kehr, *et al.*, "Sub-diffractional cavity modes of terahertz hyperbolic phonon polaritons in tin oxide," *Nat. Commun.*, vol. 12, no. 1, pp. 1–9, 2021.

[139] N. C. Passler, X. Ni, G. Hu, J. R. Matson, G. Carini, M. Wolf, M. Schubert, A. Alù, J. D. Caldwell, T. G. Folland, *et al.*, "Hyperbolic shear polaritons in low-symmetry crystals," *Nature*, vol. 602, no. 7898, pp. 595–600, 2022.

[140] M. He, T. G. Folland, J. Duan, P. Alonso-González, S. De Liberato, A. Paarmann, and J. D. Caldwell, "Anisotropy and modal hybridization in infrared nanophotonics using low-symmetry materials," *ACS Photonics*, vol. 9, no. 4, pp. 1078–1095, 2022.

[141] D. Basov, M. Fogler, and F. García de Abajo, "Polaritons in van der waals materials," *Science*, vol. 354, no. 6309, p. aag1992, 2016.

[142] W. Ma, P. Alonso-González, S. Li, A. Y. Nikitin, J. Yuan, J. Martín-Sánchez, J. Taboada-Gutiérrez, I. Amenabar, P. Li, S. Vélez, *et al.*, "In-plane anisotropic and ultra-low-loss polaritons in a natural van der waals crystal," *Nature*, vol. 562, no. 7728, pp. 557–562, 2018.

[143] A. Ambrosio, M. Tamagnone, K. Chaudhary, L. A. Jauregui, P. Kim, W. L. Wilson, and F. Capasso, "Selective excitation and imaging of ultraslow phonon polaritons in thin hexagonal boron nitride crystals," *Light Sci. Appl.*, vol. 7, no. 1, pp. 1–9, 2018.

[144] K. Chaudhary, M. Tamagnone, M. Rezaee, D. K. Bediako, A. Ambrosio, P. Kim, and F. Capasso, "Engineering phonon polaritons in van der waals heterostructures to enhance in-plane optical anisotropy," *Sci. Adv.*, vol. 5, no. 4, p. eaau7171, 2019.

[145] Z. Zheng, N. Xu, S. L. Oscurato, M. Tamagnone, F. Sun, Y. Jiang, Y. Ke, J. Chen, W. Huang, W. L. Wilson, *et al.*, "A mid-infrared biaxial hyperbolic van der waals crystal," *Sci. Adv.*, vol. 5, no. 5, p. eaav8690, 2019.

[146] Q. Zhang, Q. Ou, G. Hu, J. Liu, Z. Dai, M. S. Fuhrer, Q. Bao, and C.-W. Qiu, "Hybridized hyperbolic surface phonon polaritons at α-moo3 and polar dielectric interfaces," *Nano Lett.*, vol. 21, no. 7, pp. 3112–3119, 2021.

[147] J. Yang, J. Tang, M. B. Ghasemian, M. Mayyas, Q. V. Yu, L. H. Li, and K. Kalantar-Zadeh, "High-q phonon-polaritons in spatially confined freestanding α-moo3," *ACS Photonics*, vol. 9, no. 3, pp. 905–913, 2022.

[148] A. Bylinkin, M. Schnell, F. Calavalle, P. Li, J. Taboada-Gutièrrez, S. Liu, J. H. Edgar, F. Casanova, L. E. Hueso, P. Alonso-Gonzalez, *et al.*, "Real-space observation of vibrational strong coupling between propagating phonon polaritons and organic molecules," *Nat. Photonics*, vol. 15, no. 3, pp. 197–202, 2021.

[149] E. Yoxall, M. Schnell, A. Y. Nikitin, O. Txoperena, A. Woessner, M. B. Lundeberg, F. Casanova, L. E. Hueso, F. H. Koppens, and R. Hillenbrand, "Direct observation of ultraslow hyperbolic polariton propagation with negative phase velocity," *Nat. Photonics*, vol. 9, no. 10, pp. 674–678, 2015.

[150] M. Dressel and G. Grüner, *Electrodynamics of solids: optical properties of electrons in matter*. American Association of Physics Teachers, 2002.

[151] J. Dionne, L. Sweatlock, H. Atwater, and A. Polman, "Planar metal plasmon waveguides: frequency-dependent dispersion, propagation, localization, and loss beyond the free electron model," *Phys. Rev. B*, vol. 72, no. 7, p. 075405, 2005.

[152] K. J. Kaltenecker, E. Krauss, L. Casses, M. Geisler, B. Hecht, N. A. Mortensen, P. U. Jepsen, and N. Stenger, "Mono-crystalline gold platelets: a high-quality platform for surface plasmon polaritons," *Nanophotonics*, vol. 9, no. 2, pp. 509–522, 2020.

[153] D.-Z. A. Chen, A. Narayanaswamy, and G. Chen, "Surface phonon-polariton mediated thermal conductivity enhancement of amorphous thin films," *Phys. Rev. B*, vol. 72, no. 15, p. 155435, 2005.

[154] L. Tranchant, S. Hamamura, J. Ordonez-Miranda, T. Yabuki, A. Vega-Flick, F. Cervantes-Alvarez, J. J. Alvarado-Gil, S. Volz, and K. Miyazaki, "Two-dimensional phonon polariton heat transport," *Nano Lett.*, vol. 19, no. 10, pp. 6924–6930, 2019.

[155] Y. Wu, J. Ordonez-Miranda, S. Gluchko, R. Anufriev, D. D. S. Meneses, L. Del Campo, S. Volz, and M. Nomura, "Enhanced thermal conduction by surface phonon-polaritons," *Sci. Adv.*, vol. 6, no. 40, p. eabb4461, 2020.

[156] Y. Liu, D. F. Pile, Z. Liu, D. Wu, C. Sun, and X. Zhang, "Negative group velocity of surface plasmons on thin metallic films," *Proc. SPIE*, vol. 6323, pp. 224–232, 2006.

[157] N. C. Passler, I. Razdolski, D. S. Katzer, D. F. Storm, J. D. Caldwell, M. Wolf, and A. Paarmann, "Second harmonic generation from phononic epsilon-near-zero berreman modes in ultrathin polar crystal films," *Acs Photonics*, vol. 6, no. 6, pp. 1365–1371, 2019.

[158] S. Campione, I. Brener, and F. Marquier, "Theory of epsilon-near-zero modes in ultrathin films," *Phys. Rev. B*, vol. 91, no. 12, p. 121408, 2015.

[159] R. Hillenbrand, T. Taubner, and F. Keilmann, "Phonon-enhanced light–matter interaction at the nanometre scale," *Nature*, vol. 418, no. 6894, pp. 159–162, 2002.

[160] F. Mörz, R. Semenyshyn, T. Steinle, F. Neubrech, U. Zschieschang, H. Klauk, A. Steinmann, and H. Giessen, "Nearly diffraction limited ftir mapping using an ultrastable broadband femtosecond laser tunable from 1.33 to 8 μm," *Opt. Express*, vol. 25, no. 26, pp. 32355–32363, 2017.

[161] B. Hauer, A. P. Engelhardt, and T. Taubner, "Quasi-analytical model for scattering infrared near-field microscopy on layered systems," *Opt. Express*, vol. 20, no. 12, pp. 13173–13188, 2012.

[162] A. Mancini, L. Nan, F. J. Wendisch, R. Berté, H. Ren, E. Cortés, and S. A. Maier, "Near-field retrieval of the surface phonon polariton dispersion in free-standing silicon carbide thin films," *ACS Photonics*, 2022.

[163] F. Walla, M. M. Wiecha, N. Mecklenbeck, S. Beldi, F. Keilmann, M. D. Thomson, and H. G. Roskos, "Anisotropic excitation of surface plasmon polaritons on a metal film by a scattering-type scanning near-field microscope with a non-rotationally-symmetric probe tip," *Nanophotonics*, vol. 7, no. 1, pp. 269–276, 2018.

[164] J. Barnett, D. Wendland, M. Lewin, K. Wirth, A. Heßler, and T. Taubner, "Investigation of low-confinement surface phonon polariton launching on sic and srtio3 using scanning near-field optical microscopy," *Appl. Phys. Lett.*, vol. 120, no. 21, p. 211107, 2022.

[165] F. Hu, Y. Luan, M. Scott, J. Yan, D. Mandrus, X. Xu, and Z. Fei, "Imaging exciton–polariton transport in mose2 waveguides," *Nat. Phot.*, vol. 11, no. 6, pp. 356–360, 2017.

[166] B. Liao, X. Guo, D. Hu, F. Zhai, H. Hu, K. Chen, C. Luo, M. Liu, X. Yang, and Q. Dai, "A multibeam interference model for analyzing complex near-field images of polaritons in 2d van der waals microstructures," *Adv. Funct. Mater.*, vol. 29, no. 42, p. 1904662, 2019.

[167] A. A. Abrikosov, "The magnetic properties of superconducting alloys," *Journal of Physics and Chemistry of Solids*, vol. 2, no. 3, pp. 199–208, 1957.

[168] O. V. Lounasmaa and E. Thuneberg, "Vortices in rotating superfluid 3he," *Proceedings of the National Academy of Sciences*, vol. 96, no. 14, pp. 7760–7767, 1999.

[169] K. G. Lagoudakis, M. Wouters, M. Richard, A. Baas, I. Carusotto, R. André, L. S. Dang, and B. Deveaud-Plédran, "Quantized vortices in an exciton–polariton condensate," *Nature physics*, vol. 4, no. 9, pp. 706–710, 2008.

[170] G. Lerario, A. Fieramosca, F. Barachati, D. Ballarini, K. S. Daskalakis, L. Dominici, M. De Giorgi, S. A. Maier, G. Gigli, S. Kéna-Cohen, *et al.*, "Room-temperature superfluidity in a polariton condensate," *Nature Physics*, vol. 13, no. 9, pp. 837–841, 2017.

[171] S.-Z. Lin, X. Wang, Y. Kamiya, G.-W. Chern, F. Fan, D. Fan, B. Casas, Y. Liu, V. Kiryukhin, W. H. Zurek, *et al.*, "Topological defects as relics of emergent continuous symmetry and higgs condensation of disorder in ferroelectrics," *Nature Physics*, vol. 10, no. 12, pp. 970–977, 2014.

[172] F. P. Chmiel, N. Waterfield Price, R. D. Johnson, A. D. Lamirand, J. Schad, G. van der Laan, D. T. Harris, J. Irwin, M. S. Rzchowski, C.-B. Eom, *et al.*, "Observation of magnetic vortex pairs at room temperature in a planar α-fe2o3/co heterostructure," *Nature Materials*, vol. 17, no. 7, pp. 581–585, 2018.

[173] M. Uchida and A. Tonomura, "Generation of electron beams carrying orbital angular momentum," *nature*, vol. 464, no. 7289, pp. 737–739, 2010.

[174] J. Verbeeck, H. Tian, and P. Schattschneider, "Production and application of electron vortex beams," *Nature*, vol. 467, no. 7313, pp. 301–304, 2010.

[175] C. W. Clark, R. Barankov, M. G. Huber, M. Arif, D. G. Cory, and D. A. Pushin, "Controlling neutron orbital angular momentum," *Nature*, vol. 525, no. 7570, pp. 504–506, 2015.

[176] D. Sarenac, M. E. Henderson, H. Ekinci, C. W. Clark, D. G. Cory, L. DeBeer-Schmitt, M. G. Huber, C. Kapahi, and D. A. Pushin, "Experimental realization of neutron helical waves," *Science Advances*, vol. 8, no. 46, p. eadd2002, 2022.

[177] A. Luski, Y. Segev, R. David, O. Bitton, H. Nadler, A. R. Barnea, A. Gorlach, O. Cheshnovsky, I. Kaminer, and E. Narevicius, "Vortex beams of atoms and molecules," *Science*, vol. 373, no. 6559, pp. 1105–1109, 2021.

[178] I. P. Ivanov, "Promises and challenges of high-energy vortex states collisions," *Progress in Particle and Nuclear Physics*, p. 103987, 2022.

[179] J. Wang, J.-Y. Yang, I. M. Fazal, N. Ahmed, Y. Yan, H. Huang, Y. Ren, Y. Yue, S. Dolinar, M. Tur, *et al.*, "Terabit free-space data transmission employing orbital angular momentum multiplexing," *Nature photonics*, vol. 6, no. 7, pp. 488–496, 2012.

[180] Y. Yan, G. Xie, M. P. Lavery, H. Huang, N. Ahmed, C. Bao, Y. Ren, Y. Cao, L. Li, Z. Zhao, *et al.*, "High-capacity millimetre-wave communications with orbital angular momentum multiplexing," *Nature communications*, vol. 5, no. 1, p. 4876, 2014.

[181] A. E. Willner, H. Huang, Y. Yan, Y. Ren, N. Ahmed, G. Xie, C. Bao, L. Li, Y. Cao, Z. Zhao, *et al.*, "Optical communications using orbital angular momentum beams," *Advances in optics and photonics*, vol. 7, no. 1, pp. 66–106, 2015.

[182] A. Mair, A. Vaziri, G. Weihs, and A. Zeilinger, "Entanglement of the orbital angular momentum states of photons," *Nature*, vol. 412, no. 6844, pp. 313–316, 2001.

[183] E. Nagali, F. Sciarrino, F. De Martini, L. Marrucci, B. Piccirillo, E. Karimi, and E. Santamato, "Quantum information transfer from spin to orbital angular momentum of photons," *Physical review letters*, vol. 103, no. 1, p. 013601, 2009.

[184] R. Fickler, R. Lapkiewicz, M. Huber, M. P. Lavery, M. J. Padgett, and A. Zeilinger, "Interface between path and orbital angular momentum entanglement for high-dimensional photonic quantum information," *Nature communications*, vol. 5, no. 1, p. 4502, 2014.

[185] L. Allen, M. W. Beijersbergen, R. Spreeuw, and J. Woerdman, "Orbital angular momentum of light and the transformation of laguerre-gaussian laser modes," *Physical review A*, vol. 45, no. 11, p. 8185, 1992.

[186] M. Pu, X. Li, X. Ma, Y. Wang, Z. Zhao, C. Wang, C. Hu, P. Gao, C. Huang, H. Ren, *et al.*, "Catenary optics for achromatic generation of perfect optical angular momentum," *Science Advances*, vol. 1, no. 9, p. e1500396, 2015.

[187] R. C. Devlin, A. Ambrosio, N. A. Rubin, J. B. Mueller, and F. Capasso, "Arbitrary spin-to–orbital angular momentum conversion of light," *Science*, vol. 358, no. 6365, pp. 896–901, 2017.

[188] A. H. Dorrah, N. A. Rubin, M. Tamagnone, A. Zaidi, and F. Capasso, "Structuring total angular momentum of light along the propagation direction with polarization-controlled meta-optics," *Nature communications*, vol. 12, no. 1, p. 6249, 2021.

[189] H. Ren and S. A. Maier, "Nanophotonic materials for twisted-light manipulation," *Advanced Materials*, p. 2106692, 2021.

[190] M. de Oliveira, M. Piccardo, S. Eslami, V. Aglieri, A. Toma, and A. Ambrosio, "Radially and azimuthally pure vortex beams from phase-amplitude metasurfaces," *ACS Photonics*, 2022.

[191] H. Ahmed, H. Kim, Y. Zhang, Y. Intaravanne, J. Jang, J. Rho, S. Chen, and X. Chen, "Optical metasurfaces for generating and manipulating optical vortex beams," *Nanophotonics*, vol. 11, no. 5, pp. 941–956, 2022.

[192] P. Genevet, J. Lin, M. A. Kats, and F. Capasso, "Holographic detection of the orbital angular momentum of light with plasmonic photodiodes," *Nature communications*, vol. 3, no. 1, pp. 1–5, 2012.

[193] H. Ren, X. Li, Q. Zhang, and M. Gu, "On-chip noninterference angular momentum multiplexing of broadband light," *Science*, vol. 352, no. 6287, pp. 805–809, 2016.

[194] Z. Yue, H. Ren, S. Wei, J. Lin, and M. Gu, "Angular-momentum nanometrology in an ultrathin plasmonic topological insulator film," *Nature Communications*, vol. 9, no. 1, p. 4413, 2018.

[195] Z. Ji, W. Liu, S. Krylyuk, X. Fan, Z. Zhang, A. Pan, L. Feng, A. Davydov, and R. Agarwal, "Photocurrent detection of the orbital angular momentum of light," *Science*, vol. 368, no. 6492, pp. 763–767, 2020.

[196] H. Ren, X. Wang, C. Li, C. He, Y. Wang, A. Pan, and S. A. Maier, "Orbital-angular-momentum-controlled hybrid nanowire circuit," *Nano Letters*, vol. 21, no. 14, pp. 6220–6227, 2021.

[197] F. Machado, N. Rivera, H. Buljan, M. Soljačić, and I. Kaminer, "Shaping polaritons to reshape selection rules," *ACS Photonics*, vol. 5, no. 8, pp. 3064–3072, 2018.

[198] A. M. Konzelmann, S. O. Krüger, and H. Giessen, "Interaction of orbital angular momentum light with rydberg excitons: Modifying dipole selection rules," *Physical Review B*, vol. 100, no. 11, p. 115308, 2019.

[199] J. Ni, S. Liu, D. Wu, Z. Lao, Z. Wang, K. Huang, S. Ji, J. Li, Z. Huang, Q. Xiong, *et al.*, "Gigantic vortical differential scattering as a monochromatic probe for multiscale chiral structures," *Proceedings of the National Academy of Sciences*, vol. 118, no. 2, p. e2020055118, 2021.

[200] H. Kim, J. Park, S.-W. Cho, S.-Y. Lee, M. Kang, and B. Lee, "Synthesis and dynamic switching of surface plasmon vortices with plasmonic vortex lens," *Nano letters*, vol. 10, no. 2, pp. 529–536, 2010.

[201] A. David, B. Gjonaj, Y. Blau, S. Dolev, and G. Bartal, "Nanoscale shaping and focusing of visible light in planar metal–oxide–silicon waveguides," *Optica*, vol. 2, no. 12, pp. 1045–1048, 2015.

[202] A. David, B. Gjonaj, and G. Bartal, "Two-dimensional optical nanovortices at visible light," *Physical Review B*, vol. 93, no. 12, p. 121302, 2016.

[203] G. Spektor, D. Kilbane, A. Mahro, B. Frank, S. Ristok, L. Gal, P. Kahl, D. Podbiel, S. Mathias, H. Giessen, *et al.*, "Revealing the subfemtosecond dynamics of orbital angular momentum in nanoplasmonic vortices," *Science*, vol. 355, no. 6330, pp. 1187–1191, 2017.

[204] Y. Yang, L. Wu, Y. Liu, D. Xie, Z. Jin, J. Li, G. Hu, and C.-W. Qiu, "Deuterogenic plasmonic vortices," *Nano Letters*, vol. 20, no. 9, pp. 6774–6779, 2020.

[205] G. Spektor, E. Prinz, M. Hartelt, A.-K. Mahro, M. Aeschlimann, and M. Orenstein, "Orbital angular momentum multiplication in plasmonic vortex cavities," *Science Advances*, vol. 7, no. 33, p. eabg5571, 2021.

[206] K. Frischwasser, K. Cohen, J. Kher-Alden, S. Dolev, S. Tsesses, and G. Bartal, "Real-time sub-wavelength imaging of surface waves with nonlinear near-field optical microscopy," *Nature Photonics*, vol. 15, no. 6, pp. 442–448, 2021.

[207] Y. Bai, J. Yan, H. Lv, and Y. Yang, "Plasmonic vortices: a review," *Journal of Optics*, 2022.

[208] E. Prinz, M. Hartelt, G. Spektor, M. Orenstein, and M. Aeschlimann, "Orbital angular momentum in nanoplasmonic vortices," *ACS Photonics*, 2023.

[209] L. Xiong, Y. Li, D. Halbertal, M. Sammon, Z. Sun, S. Liu, J. H. Edgar, T. Low, M. M. Fogler, C. R. Dean, *et al.*, "Polaritonic vortices with a half-integer charge," *Nano letters*, vol. 21, no. 21, pp. 9256–9261, 2021.

[210] M. Wang, G. Hu, S. Chand, M. Cotrufo, Y. Abate, K. Watanabe, T. Taniguchi, G. Grosso, C.-W. Qiu, and A. Alù, "Spin-orbit-locked hyperbolic polariton vortices carrying reconfigurable topological charges," *eLight*, vol. 2, no. 1, pp. 1–11, 2022.

[211] K. Y. Bliokh, F. J. Rodríguez-Fortuño, F. Nori, and A. V. Zayats, "Spin–orbit interactions of light," *Nature Photonics*, vol. 9, no. 12, pp. 796–808, 2015.

[212] S. Tsesses, E. Ostrovsky, K. Cohen, B. Gjonaj, N. Lindner, and G. Bartal, "Optical skyrmion lattice in evanescent electromagnetic fields," *Science*, vol. 361, no. 6406, pp. 993–996, 2018.

[213] S. Tsesses, K. Cohen, E. Ostrovsky, B. Gjonaj, and G. Bartal, "Spin–orbit interaction of light in plasmonic lattices," *Nano letters*, vol. 19, no. 6, pp. 4010–4016, 2019.

[214] M. Schnell, A. García-Etxarri, A. Huber, K. Crozier, J. Aizpurua, and R. Hillenbrand, "Controlling the near-field oscillations of loaded plasmonic nanoantennas," *Nature Photonics*, vol. 3, no. 5, pp. 287–291, 2009.

[215] M. Schnell, A. Garcia-Etxarri, J. Alkorta, J. Aizpurua, and R. Hillenbrand, "Phase-resolved mapping of the near-field vector and polarization state in nanoscale antenna gaps," *Nano letters*, vol. 10, no. 9, pp. 3524–3528, 2010.

[216] P. Alonso-Gonzalez, M. Schnell, P. Sarriugarte, H. Sobhani, C. Wu, N. Arju, A. Khanikaev, F. Golmar, P. Albella, L. Arzubiaga, *et al.*, "Real-space mapping of fano

interference in plasmonic metamolecules," *Nano letters*, vol. 11, no. 9, pp. 3922–3926, 2011.

[217] B. J. Bohn, M. Schnell, M. A. Kats, F. Aieta, R. Hillenbrand, and F. Capasso, "Near-field imaging of phased array metasurfaces," *Nano letters*, vol. 15, no. 6, pp. 3851–3858, 2015.

[218] A. J. Sternbach, S. Latini, S. Chae, H. Hübener, U. De Giovannini, Y. Shao, L. Xiong, Z. Sun, N. Shi, P. Kissin, *et al.*, "Femtosecond exciton dynamics in wse2 optical waveguides," *Nature communications*, vol. 11, no. 1, pp. 1–6, 2020.

[219] Y. Luan, H. Zobeiri, X. Wang, E. Sutter, P. Sutter, and Z. Fei, "Imaging anisotropic waveguide exciton polaritons in tin sulfide," *Nano Letters*, vol. 22, no. 4, pp. 1497–1503, 2022.

[220] N. C. Passler and A. Paarmann, "Generalized 4× 4 matrix formalism for light propagation in anisotropic stratified media: study of surface phonon polaritons in polar dielectric heterostructures," *JOSA B*, vol. 34, no. 10, pp. 2128–2139, 2017.

[221] T. Teperik, A. Archambault, F. Marquier, and J.-J. Greffet, "Huygens-fresnel principle for surface plasmons," *Optics express*, vol. 17, no. 20, pp. 17483–17490, 2009.

[222] M. Bertalmio, A. L. Bertozzi, and G. Sapiro, "Navier-stokes, fluid dynamics, and image and video inpainting," in *Proceedings of the 2001 IEEE Computer Society Conference on Computer Vision and Pattern Recognition. CVPR 2001*, vol. 1, pp. I–I, IEEE, 2001.

[223] M. Tamagnone, A. Ambrosio, K. Chaudhary, L. A. Jauregui, P. Kim, W. L. Wilson, and F. Capasso, "Ultra-confined mid-infrared resonant phonon polaritons in van der waals nanostructures," *Sci. Adv.*, vol. 4, no. 6, p. eaat7189, 2018.

[224] A. Liu, G. Rui, X. Ren, Q. Zhan, G. Guo, and G. Guo, "Encoding photonic angular momentum information onto surface plasmon polaritons with plasmonic lens," *Optics Express*, vol. 20, no. 22, pp. 24151–24159, 2012.

[225] G. Rui, Q. Zhan, and Y. Cui, "Tailoring optical complex field with spiral blade plasmonic vortex lens," *Scientific Reports*, vol. 5, no. 1, pp. 1–9, 2015.

[226] J. v. Neumann and E. Wigner, "Uber merkwürdige diskrete eigenwerte," *Physikalische Zeitschrift*, vol. 30, pp. 465–467, 1929.

[227] C. W. Hsu, B. Zhen, A. D. Stone, J. D. Joannopoulos, and M. Soljačić, "Bound states in the continuum," *Nature Reviews Materials*, vol. 1, no. 9, p. 16048, 2016.

[228] F. Monticone and A. Alù, "Embedded photonic eigenvalues in 3d nanostructures," *Physical Review Letters*, vol. 112, no. 21, p. 213903, 2014.

[229] Z. F. Sadrieva, K. Frizyuk, M. I. Petrov, Y. S. Kivshar, and A. A. Bogdanov, "Multipolar origin of bound states in the continuum," *Physical Review B*, 2019.

[230] B. Zhen, C. W. Hsu, L. Lu, A. Stone, and M. Soljači'c, "Topological nature of optical bound states in the continuum," *Phys. Rev. Lett.*, vol. 113, p. 257401, 2014.

[231] C. W. Hsu, B. Zhen, J. Lee, S.-L. Chua, S. Johnson, J. D. Joannopoulos, and M. Soljači'c, "Observation of trapped light within the radiation continuum," *Nature*, vol. 499, p. 188, 2013.

[232] P. Yu, A. Kupriianov, V. Dmitriev, and V. Tuz, "All-dielectric metasurfaces with trapped modes: group-theoretical description," *arXiv preprint arXiv:1812.10817*, 2018.

[233] L. Ni, Z. Wang, C. Peng, and Z. Li, "Tunable optical bound states in the continuum beyond in-plane symmetry protection," *Phys. Rev. B*, vol. 94, p. 245148, 2016.

[234] H. Friedrich and D. Wintgen, "Interfering resonances and bound states in the continuum," *Phys. Rev. A*, vol. 32, p. 3231, 1985.

[235] G. Leitis and et al., "Leitis et al., sci. adv. 2019;5:eaaw2871," *Science Advances*, vol. 5, no. 5, p. eaaw2871, 2019.

[236] L. S. A. B. M. N. P. W. J. K. . J. J. F. S. A. M. Thomas Weber, Lucca Kúhner and A. Tittl1, "Investigating plasmonic catalysis kinetics on hot-spot engineered nanoantennae," *Nature Matierials*.

[237] H. A. Haus, *Waves and Fields in Optoelectronics*. Prentice-Hall, 1984.